Charles University in Prague
Faculty of Mathematics and Physics

DOCTORAL THESIS

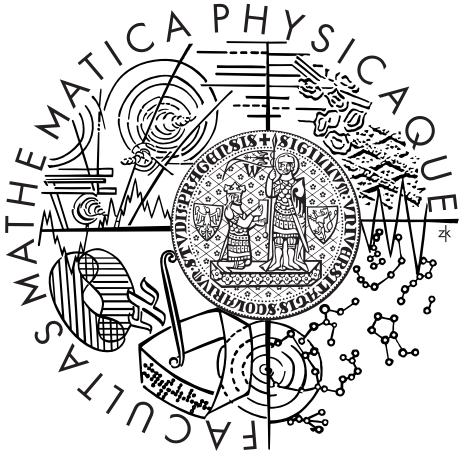

Lucie Szabová

Chemical reactivity of metal-supported ceria thin films: a density functional study

Department of Surface and Plasma Science

Supervisor of the doctoral thesis: Prof. RNDr. Vladimír Matolín, DrSc.
Advisor of the doctoral thesis: Dr. Stefano Fabris
Specialization: Surface and Interface Physics

Praha 2013

In the first place I would like to gratefully thank my advisor Dr. Stefano Fabris for the valuable guidance, helpful discussions and appreciated advice. I am also grateful to my supervisor Prof. RNDr. Vladimír Matolín, DrSc. for his help and support during my studies and for all the great opportunities he provided. I would like to thank Dr. Josef Mysliveček for frequent discussions, his patience to explain many issues not only from the experimental field. I would also like to thank my colleagues and friends Filip Dvořák and Oleksandr Stetsovych for providing the experimental results to motivate and support my calculations and valuable explanations in the field of STM. Last I want to thank my family (among whom especially my sister Lenka Szabová) and friends, namely Tatiana Zahoranová, Ľubica Valentová, Pavol Jusko and many others for their support and help.

Prohlašuji, že jsem tuto disertační práci vypracovala samostatně a výhradně s použitím citovaných pramenů, literatury a dalších odborných zdrojů.

Beru na vědomí, že se na moji práci vztahují práva a povinnosti vyplývající ze zákona č. 121/2000 Sb., autorského zákona v platném znění, zejména skutečnost, že Univerzita Karlova v Praze má právo na uzavření licenční smlouvy o užití této práce jako školního díla podle §60 odst. 1 autorského zákona.

V ..... dne .....

Název práce: Chemická reaktivita tenkých vrstev oxidů ceru na kovových podložkách studovaná metodou teorie funkcionálu hustoty

Autor: Lucie Szabová

Katedra (ústav): Katedra fyziky povrchů a plazmatu

Vedoucí dizertační práce: Prof. RNDr. Vladimír Matolín, DrSc., Katedra fyziky povrchů a plazmatu, MFF, UK

Abstrakt: Tato práce je zaměřená na teoretické výpočty fyzikálních a chemických vlastností ultratenkých vrstev oxidů ceru nanesených na Cu(111) metodou numerických DFT+U simulací. Oxidy ceru vykazují vysokou účinnost zejména pro rozklad vody a CO oxidaci, což jsou reakce s velkým významem pro katalýzu a palivové články. Práce ukazuje, že elektronické, strukturní i chemické vlastnosti tenkých vrstev jsou významně závislé na jejich tloušťce. Výpočty spolu s experimenty provedené pomocí skenovacího tunelového mikroskopu ukazují rozdíl v náboji, napětí a přítomnosti kyslíkových vakancí mezi první monovrstvou a tlustšími vrstvami. Rozdíly v reaktivitě vrstev v závislosti na tloušťce byly ukázány na případu adsorpce vody. Vrstva oxidu tlustá dvě monovrstvy vykazuje vyšší adsorpční energie než tenčí nebo tlustší vrstvy.

Klíčová slova: DFT, heterogenní katalýza, rozhraní kov/oxid, elektronová struktura, fyzika povrchů

Title: Chemical reactivity of metal-supported ceria thin films: a density functional study

Author: Lucie Szabová

Department: Department of Surface and Plasma Science

Supervisor: Prof. RNDr. Vladimír Matolín, DrSc., Department of Surface and Plasma Science, FMF, CU

Abstract: The present work is a theoretical analysis based on numerical DFT+U simulations investigating the physical and chemical properties of ultrathin ceria films supported by Cu(111). Such materials exhibit high activity towards several important reactions in heterogeneous catalysis such as water-gas shift and CO oxidation, with important applications also for renewable energy technologies such as fuel cells. We provide evidence of the influence of film thickness on the electronic and structural properties as well as on the reactivity of ultrathin ceria films supported by copper. The calculations combined with scanning tunneling microscopy experiments show that one monolayer thin film of ceria on Cu(111) is charged, strained and contains oxygen vacancies due to the limited thickness of the film. The influence of the film thickness on the reactivity of thin ceria films was explored for the case of water adsorption and dissociation. Significant differences were shown for water adsorption and dissociation on one-monolayer ceria compared to thicker films, in particular the two monolayer film exhibited highest adsorption energies.

Keywords: DFT, heterogeneous catalysts, metal/oxide interface, surface science, electronic structure

Contents

Chapter 1

Introduction

Environmental protection together with the attempts for finding new, cleaner sources of energy gains more and more importance in the present time. These problems are closely connected with development of new, cheaper and more effective catalysts. Fuel cells allow for converting chemical energy to electricity through an electrochemical reaction. The most frequently used fuels in these devices are hydrogen (H_2), hydrocarbons or alcohols such as methanol. Polymer electrolyte membrane fuel cells (PEMFC) are among the most promising technologies for portable applications, while solid-oxide fuel cells are better suited for power-intensive applications [1]. Highly efficient catalysts are necessary to operate efficiently these fuel cells as well as to produce the necessary fuel. The most used technology to produce H_2 for fuel cells is steam reforming with water gas shift reaction (WGS) or alcohol decomposition. The use of H_2 in PEMFCs requires its purification to prevent poisoning of the anode by CO. Therefore advanced catalysts capable of preferential oxidation of CO in the presence of H_2 are required.

Several types of catalysts are used for this purpose, such as noble metal-based (Pd, Pt, Rh) materials, often supported on or dispersed in metal-oxides. In this context cerium oxides are frequently used components of catalysts for WGS or preferential oxidation of CO. In the ceria-based catalysts, cerium oxide has the role to support and promote the catalytic activity of the precious metals supported by or incorporated into ceria. An example of such ceria-based catalytic systems are gold-ceria catalysts for preferential oxidation of CO [2] and platinum-ceria catalysts frequently used as anode catalysts in fuel cells [3, 4, 5, 6]. Copper-ceria catalysts are widely analyzed because of their high activity in preferential oxidation of CO [7, 8], WGS reaction [9, 10, 11, 12], methanol steam reforming [13] and hydrogen production as catalysts in PEMFCs [14, 2, 15]. It was shown that even a small amount of Cu can greatly enhance catalytic properties of ceria [16, 17, 18, 19, 20, 11].

In many cases the role of ceria in ceria-based catalytic systems is not only to support metal particles and reduce the amount of metal needed, but also to promote the catalytic reactions by its ability to store and release oxygen depending on the surrounding conditions. This property is called oxygen storage capacity (OSC) and is based on the easy and reversible change of the valence state of cerium ions $Ce^{4+} < - > Ce^{3+}$, which accompanies ceria reduction from the

stoichiometric cerium oxide CeO_2 to the reduced form Ce_2O_3.

In the present time more and more often theoretical calculations help the development of new more effective catalysts with improved reactivity, particularly by evaluating the electronic and chemical properties of the catalytic materials and the mechanisms of catalytic reactions as well as assisting the interpretation of experimental measurements. Numerical modeling of catalytic materials takes advantage of variety of methods from classical potentials to sophisticated many-body electronic structure methods. The catalytic activity of ceria is closely connected to the valence change $Ce^{3+} <-> Ce^{4+}$ which is mediated by localisation of excess electrons to Ce f states. Simulation of catalytic reactions on ceria thus need to be able to correctly capture electronic structure of cerium ions in both oxidation states and the changes induced upon Ce oxidation/reduction. In usual cases standard Density Functional Theory (DFT) provides a good compromise between predictive power, level and accuracy of description of the electronic properties as well as the number of atoms that can be realistically simulated with the computer power available to a standard laboratory. However this is not the case for ceria based materials as will be described later within this work. Due to the strong localization of one electron in Ce 4f states in Ce^{3+} ion in the case of the reduced form Ce_2O_3, the standard DFT is not capable of correctly describing the electronic state of the reduced form of ceria. There are several possibilities to overcome this problem. A practical one is to modify the DFT functional by adding Hubbard U term to Local Density Approximation (LDA) or Generalized Gradient Approximation (GGA) exchange correlation functional. The present work employs such modified DFT+U method, which became popular for simulations of highly reducible oxides such as CeO_2, TiO_2 [21] or Co_3O_4.

Water is present in catalytic systems either as an impurity in the atmosphere, as constituents in catalytic reactions (in the case of WGS) or a by-product such as the O_2 electrochemical reduction in fuel cells. Water interaction with ceria surfaces has been extensively studied, but the exact mechanism is still under debate [22, 23]. For example it was shown that water can bind both molecularly and dissociatively on both stoichiometric and reduced ceria surfaces [24, 25]. Also the effect of H_2O adsorption on ceria surface, whether it causes oxidation or reduction of the surface is still unclear [26, 27, 28, 24]. Understanding the exact mechanism of H_2O adsorption or dissociation on catalytic systems based on ceria is essential for development of new more efficient catalysts. The state-of-the-art research focuses on molecular adsorption in low coverages and low pressure conditions. However up to now, no studies of more realistic environments have been reported. The present work aims to provide a support for future studies of much more complex cases of water present on surfaces in form of multilayers or drops simulating more realistic conditions.

The present work focuses on a specific system consisting of copper and ceria, that was recently synthesized in the laboratories of prof. Vladimír Matolín in Prague. The present calculations are instrumental to a combined theory-experiment characterization of this new catalyst. In particular, we aim to study the inverse model copper/ceria catalysts formed by ultrathin ceria layers on Cu(111) substrate. Inverse model systems are interesting, since they allow to complement the studies of real catalytic systems formed by metal particles sup-

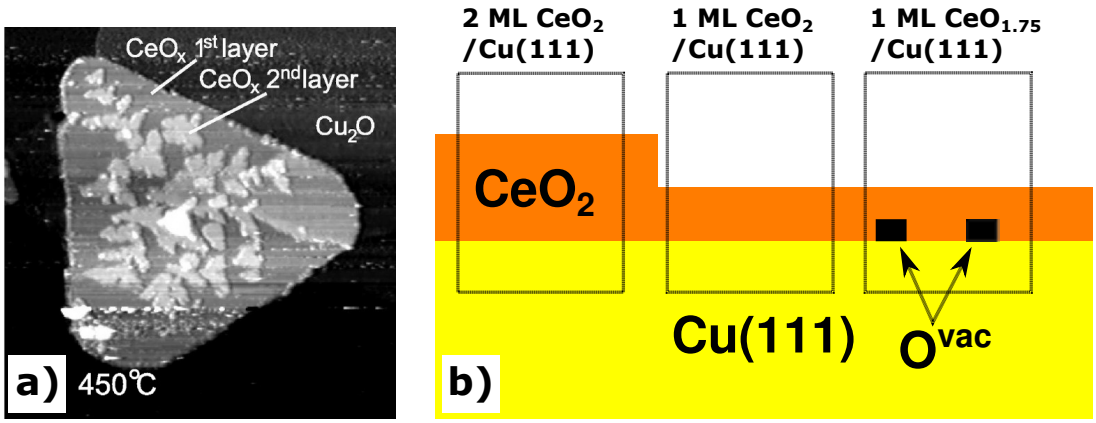

Figure 1.1: STM image of ceria island on Cu(111) exhibiting 1 and 2 ML areas (a). Reprinted with permission from Dvořák et al. J. Phys. Chem. C , 115, 7496-7503, 2011. Copyright 2013 American Chemical Society. Schematic figure of 1 and 2 ML ceria films on Cu(111) substrate (b). The defective 1 ML film encompass oxygen vacancies at the interface.

ported by oxides as well as to describe the situation where an oxide support encapsulate the metal particle. The inverse model catalysts represent more simple systems allowing to study their properties under more controlled conditions.

Our calculations complement the experimental measurements by scanning tunneling microscopy (STM), which allowed to observe ultrathin ceria films on Cu(111) substrate with thickness of 1 and 2 monolayer (ML, O-Ce-O stacking) in atomic resolution. The experiment shows interesting properties of the 1 ML film different from the properties of the thicker films, namely the 2×2 reconstruction in the atomically resolved images of 1 ML film as well as the moiré patterns in the large scale images suggesting a strain in the thin films.

In order to understand the origin of observed different properties of the 1 ML ceria film compared to thicker films, we first analyze the structural and electronic properties of these films. The combined experimental (STM) and theoretical (DFT+U) study identifies the finite size effect of the thickness of the film to be responsible for the different properties of 1 ML ceria film. Subsequently we proceed with study of the impact of confinement effects in thin ceria films on their reactivity. As a probe we employ the water molecule adsorbed on the thin films molecularly and dissociatively. We explore the binding of water on the thin films as a function of thickness of the film using the adsorption energy as a descriptor of reactivity. The size effect demonstrating as presence/absence of structural defects (oxygen vacancies) and electronic defects (Ce^{3+} ions) in the films of different thickness can provide different conditions for adsorption not available on stoichiometric surfaces.

1.1 Work plan

The thesis is organized as follows.

In the second chapter we introduce the method used to calculate properties of

copper/ceria catalytic systems. We describe the DFT method together with the approximations relevant to the present study. We also introduce the modification of this theory DFT+U, which allow to perform calculations on strongly correlated systems containing ceria.

In the third chapter we give an overview of theoretical methods employed in studies on ceria based systems together with the difficulties of these methods with respect to presence of metastable solutions. Next we describe the previous results for more simple systems of either bulk copper and cerium oxides or copper/ceria interfaces formed by copper adatoms on stoichiometric and reduced ceria (111) substrates. We also show the structural and electronic properties of $Cu(111)/CeO_2(111)$ interface from our previous calculations.

In the fourth chapter we calculate the properties of ultrathin ceria layers on Cu(111) substrate as an example of inverse model catalyst. We employ model systems formed by defective and stoichiometric 1 and 2 ML ceria on copper and discover different behaviour with respect to presence of oxygen vacancies as well as strain or electronic structure between 1 ML ceria film compared to thicker films.

In the fifth chapter we use the model systems from previous chapter to study H_2O adsorption and dissociation on ceria. We identify the stable adsorption positions and structures as well as electronic properties of the water molecule bonding on ceria films. We show the differences in H_2O adsorption on ultrathin and thicker films and ascribe the effect to the different thickness of the ceria films and charge state of Ce ions in the topmost layer of the film.

In the last chapter we summarise the main findings and conclusions.

Chapter 2

Density Functional Theory

In this chapter I will focus on the theoretical methods used to model the Cu/CeO_2 systems. I will introduce the Density Functional Theory (DFT) and summarize the approximations leading to the practical use of DFT in calculations. The specific implementations of the numerical tools allowing for DFT calculations such as wave-function basis set and pseudopotentials will also be presented. Last I will introduce the DFT+U method allowing for description of strongly correlated materials such as ceria.

2.1 DFT

The theoretical understanding of the function of the heterogeneous catalysts, which is of most importance in the present time, requires accurate and precise quantum mechanic calculations. Exploring electronic properties and predicting chemical behaviour of the chemical compounds requires solving the Schrödinger equation. The *time independent Schrödinger equation* is

$$\hat{H}\Psi = E\Psi, \tag{2.1}$$

where $\hat{H}$ is the *Hamiltonian* operator and the Ψ is the wave function describing the state of the system and is a function of all the concerned objects. In case of compounds, the system is composed of nuclei and electrons. Therefore the Ψ is a function of position of each electron and nucleus and the Hamiltonian operator has following form presented in Ref. [29]

$$\hat{H} = -\frac{\hbar^2}{2m_e}\sum_i \nabla_i^2 - \sum_{i,I}\frac{Z_I e^2}{|\vec{r_i} - \vec{R_I}|} + \frac{1}{2}\sum_{i\neq j}\frac{e^2}{|\vec{r_i} - \vec{r_j}|} - \tag{2.2}$$
$$-\frac{\hbar^2}{2M_I}\sum_I \nabla_I^2 + \frac{1}{2}\sum_{I\neq J}\frac{Z_I Z_J e^2}{|\vec{R_I} - \vec{R_J}|},$$

where the lower case letters represent the quantities for the electrons and the upper case letters represent the nuclei. The m and M are the masses of the electrons and nuclei respectively, Z stands for the charge of the nuclei. The first term in this many body Hamiltonian is the kinetic energy of the electrons, while the fourth term represents the kinetic energy of the nuclei. The second,

third and fifth term express the electron-nuclei, electron-electron and nuclei-nuclei interactions respectively.

Born-Oppenheimer approximation

This very complicated problem can be simplified by realizing that the masses of electrons and ions are of a different order by the factor of almost 2000 [30]. Since the electrons are much lighter than the nuclei and the electronic motion is much faster than the nuclei motion, the *adiabatic* or *Born-Oppenheimer* approximation can be introduced based on treating the electrons and nuclei separately. When studying the electronic state of some compound, the nuclei can be considered at rest and the calculation can be focused on electrons in the potential of the nuclei. The total wave function of the system thus can be rewritten in terms of dividing to the two separate wave functions for electrons and nuclei as presented 2.3

$$\Psi(\vec{R},\vec{r}) = \phi(\vec{R})\psi(\vec{r}). \tag{2.3}$$

The Hamiltonian for system of electrons is thus reduced by neglecting the fourth term in the equation 2.2 and effectively, the ionic coordinates enter the equation as parameters.

Density Functional

The description of the system of electrons with the wave function is still very complicated since for N electrons, the electron wave function is a function of 3N spatial coordinates and N spin variables. It was proved by *Hohenberg* and *Kohn* in Ref. [31], proof is given in Ref. [29], that the ground state properties of a real system are uniquely determined by (are functionals of) the ground state electron density, which is a function of only one set of coordinates. It was also shown that the external potential acting on the electrons determines this electron density.

Hohenberg and Kohn also showed, that a unique and universal functional of the electron density $F[n(\vec{r})]$ exists, that is present in variational principle of a total energy functional $E[n(\vec{r})]$

$$E[n(\vec{r})] = F[n(\vec{r})] + \int V_{ext}(\vec{r})n(\vec{r})d\vec{r}, \tag{2.4}$$

where $F[n(\vec{r})]$ contains the kinetic energy and the mutual Coulomb interaction of the electrons and the $V_{ext}(\vec{r})$ is external potential acting on the electrons.

Kohn-Sham equations

The next very important step towards the practical applications of DFT was the substitution of the problem concerning electrons interacting with each other by an auxiliary problem of non-interacting particles with the same electron density as for the interacting problem. The legitimacy of such substitution was shown by *Kohn* and *Sham* in Ref. [32], the proof is given in Ref. [29]. Because of this approach, the functional $F[n(\vec{r})]$ formerly complicated by containing the interaction effects of the electrons could be simplified to be composed of the functionals of the

kinetic energy of the non-interacting electrons, their Coulomb interaction treated as a mean field and the exchange-correlation energy E_{xc} which accounts for all the other many-body interaction effects. It also allows to overcome the many-particle problem by solving one-particle equations as will be described in following.

As a result of the simplifications described above, solving of the Schrödinger equation 2.1 with a Hamiltonian 2.2 for a complete system reduces to solving the *Kohn-Sham one particle equations*

$$\hat{H}_{KS}\psi_i(\vec{r}) = [-\frac{\hbar^2\nabla^2}{2m} + V_{KS}(\vec{r})]\psi_i(\vec{r}) = e_i\psi_i(\vec{r}), \tag{2.5}$$

where the $\psi_i(\vec{r})$ are one-particle wave functions and $V_{KS}(\vec{r})$ is the *Kohn-Sham potential* defined as

$$V_{KS}(\vec{r}) = V_{ext} + e^2 \int \frac{n(\vec{r}')}{|\vec{r} - \vec{r}'|} d\vec{r}' + v_{xc}(\vec{r}). \tag{2.6}$$

The Kohn-Sham potential was derived from the properties of the functional $F[n(\vec{r})]$ for example in Ref. [33] or [29]. The second term in the formulation for the Kohn-Sham potential is the contribution from the Coulomb interaction of the electrons and the third term $v_{xc}(\vec{r})$ is the exchange-correlation potential defined as

$$v_{xc}(\vec{r}) = \frac{\delta E_{xc}[n]}{\delta n(\vec{r})}. \tag{2.7}$$

The Kohn-Sham equations are an effective way of acquiring properties of materials, but since the electron density is a result of solving the equations as well as it enters the equation through the Kohn-Sham potential, the solution has to be reached iteratively.

Exchange-correlation functionals

Every quantity present in the Kohn-Sham equations is exact and well defined. However the exchange-correlation energy has a very complicated expression, which is not known explicitly. This is the reason to introduce an approximation to the theory in form of simplifying the exchange-correlation energy.

The most simple approximation is called *LDA*, the *Local Density Approximation*. In LDA, the exchange-correlation energy is expressed in terms of exchange-correlation potential of the uniform electron gas, that can be calculated with great accuracy

$$E_{xc}^{LDA}[n] = \int \epsilon_{xc}^{hom}(n(\vec{r}))n(\vec{r})d\vec{r}, \tag{2.8}$$

where $\epsilon_{xc}^{hom}(n(\vec{r}))$ is the exchange-correlation density of the uniform electron gas.

The idea is to apply this function also to inhomogeneous systems, for which the value of the exchange-correlation energy is calculated point-by-point as a function of the local density with the exchange-correlation potential derived for uniform electron gas with the same density.

According to Ref. [33] the LDA can be used to calculate systems such as simple metals, intrinsic semiconductors or even non homogeneous systems as covalently bonded materials and some transition metals. It usually predicts structural and vibrational properties of those materials well but it tends to underestimate the equilibrium bond lengths and overestimate the bonding energies compared to experiments.

Some of the drawbacks of the LDA approximation can be overcome by introducing a more complicated approximation for the exchange-correlation energy – the *GGA*, *Generalized Gradient Approximation*. This approximation include also the influence of the local inhomogeneities of the electron density. The general expression of the exchange-correlation energy in the GGA approximation is

$$E_{xc}^{GGA}[n] = \int \epsilon_{xc}^{GGA}(n(\vec{r}), |\nabla n(\vec{r})|)n(\vec{r})d\vec{r}, \tag{2.9}$$

where the $\epsilon_{xc}^{GGA}(n(\vec{r}), |\nabla n(\vec{r})|)$ is different for different particular formulation of the GGA exchange-correlation energy. In this work we use the formulation of Perdew-Burke-Ernzherof (PBE) reported in Ref. [34].

In order to model materials with magnetic properties, it is useful to have the exchange-correlation energy functional directly dependent on the spin. Therefore more complicated *Local Spin Density Approximation* (*LSDA*) and also *spin polarised GGA* were formulated.

Periodic systems

The calculation of the bulk materials are based on the assumption, that the system is periodic with respect to the position of atoms, thus the external potential $V_{ext}(\vec{r})$ acting on the electrons is periodic with the periodicity of the lattice of the crystal. This periodicity can be expressed as

$$V_{ext}(\vec{r} + \vec{R}) = V_{ext}(\vec{r}), \tag{2.10}$$

where $\vec{R}$ is vector in the crystal created as integer linear combination of the crystal lattice vectors.

Not only the external potential is periodic, but also the electronic Hamiltonian operator and the physical quantities describing the system are also periodical with the same periodicity. The *Bloch theorem* can be applied expressing the single particle electronic wave function as

$$\psi_{\vec{k}v}(\vec{r}) = e^{i\vec{k}\cdot\vec{r}}u_{\vec{k}v}(\vec{r}), \tag{2.11}$$

where $u_{\vec{k}v}(\vec{r})$ is a function with the same periodicity as the crystal, the v is a discrete band index and $\vec{k}$ is the crystal momentum of the electrons defined within the first Brillouine Zone in the reciprocal space. The reciprocal space is in the relation with the real space via the expression

$$\vec{b}_i \cdot \vec{u}_j = 2\pi\delta_{ij}, \tag{2.12}$$

where the $\vec{b}_i$ are lattice vectors of the reciprocal space, $\vec{u}_j$ are lattice vectors of the real space and the indexes i and j are considered equal to 1, 2, 3.

Because of the translational invariance, the k-points can be treated independently. The sums over the electronic states figuring in expressions for many physical quantities correspond to the integrations in the Brillouine Zone and sums over the band index v. The symmetry of the crystal allows to substantially reduce the number of k-points used for the integration and further reduction can be achieved by using special points techniques such Monkhorst-Pack technique reported in Ref. [35]. To the systems which are not naturally periodic such as surfaces or interfaces the periodicity has to be artificially added for example by using a supercell method.

The application of the special point technique on the metals has difficulties because of relatively small k-point sampling of the area around the Fermi level with respect to the sensitivity of metallic properties in this area. This can be solved by either using the tetrahedron method as reported in Ref. [36] or by introducing a smearing to smoothen the weight of the states. The different smearing techniques depend on the function used for the smearing as for example the finite temperature Fermi distribution, the Lorentzian, the Gaussian [37], cold smearing factors [38] or the Methfessel and Paxton smearing technique [39].

The plane wave pseudopotential method

In order to perform practical calculations, the continuous problem has to be transformed to the more algebraic one. For this purpose the electronic wave functions are expanded to the basis set. In this work the *Plane Wave* basis set was used. This representation profits from Fourier transformation, for which efficient algorithms are available.

The Bloch electronic wave functions in this representation are

$$\psi_{\vec{k}v}(\vec{r}) = \frac{1}{(N\Omega)^{\frac{1}{2}}} \sum_{\vec{G}} e^{i(\vec{k}+\vec{G})\cdot\vec{r}} c_v(\vec{k}+\vec{G}), \tag{2.13}$$

where the Ω is the volume of the unit cell, the $\vec{G}$ are reciprocal lattice vectors and the $c_v(\vec{k}+\vec{G})$ are normalized Fourier coefficients.

The absolute precision of the result can be achieved by use of infinite number of vectors $\vec{G}$, which is not possible in the numerical calculations. Therefore only plane waves contained in the sphere of maximum kinetic energy E_{wfc}^{cut} are used in the real calculations:

$$\frac{\hbar}{2m}|\vec{k}+\vec{G}|^2 < E_{wfc}^{cut}. \tag{2.14}$$

Describing the wave functions of core electrons would require a prohibitively large number of plane waves, because of the strong localization of the wave function. This can be partially avoided by using the *Pseudopotential method*. This technique is based on the fact that the studied chemical and physical properties of the system are determined by the behaviour of the electrons in the valence bands. The electrons near to the core can be perceived as integrated to the core forming an ionic core. The pseudopotential is calculated as the external potential of those ionic cores acting on the valence electrons. The calculations then can be applied only on the valence electrons which increase the applicability of the calculations

by lowering the complexity of the problem. In this thesis the ultrasoft potential as described in Ref. [40] was used.

2.2 DFT+U

Strongly correlated materials are a challenge for standard DFT. The standard LSDA or spin polarized GGA are not able to describe properly the correct insulating electronic structure of many transition metal oxides, instead they either underestimate the band gap or even provide a wrong metallic solution. Thus in the case of such materials with valence electrons localised closer to the core, many-body effects become more and more important and better approximations than LDA or GGA are necessary [33]. One of the possibilities that has been proposed for modeling strongly-correlated materials is the DFT+U method [41, 42, 43, 44]. Within this method electronic correlation of small part of localized orbitals is treated differently from the others [45]. In order to compensate for the on-site Coulomb interaction a *Hubbard U term* is added to the LDA or GGA energy functional.

One of the possibilities for the formulation of the modified functional is the following simplified rotationally invariant version [46]

$$E_{xc}^{LDA/GGA} = E_{xc}^{LDA/GGA} + \frac{U}{2}\sum_{I} Tr[\mathbf{n}^I(1-\mathbf{n}^I)], \tag{2.15}$$

where $\mathbf{n}^I$ represent the $M \times M$ matrices and projections of the one-electron density matrix $\hat{\rho}$ over the f manifold localized at lattice site I

$$\langle \phi^I_{m\sigma} | \hat{\rho} | \phi^I_{m'\sigma'} \rangle = n^{I\sigma}_{\sigma\sigma'}. \tag{2.16}$$

M stands for the degeneracy of the localized atomic orbital (7 in the case of f orbitals).

The role of the value of the U term within this approach is to penalize the fractional occupancies of the particular orbitals and thus disfavor the wrong metallic solution and stabilize the physical insulating one. The extent of the energy penalty is governed by the parameter U.

The performance of the DFT+U method is closely dependent on the choice of U as well as on the definition of the occupancies of the particular orbitals. Both the U and the projector functions for the occupancies are part of the model and hence are in principle arbitrary. The usual choice of the projector functions are the atomic orbitals of the atomic configuration corresponding to the configuration used for the pseudopotential generation. The DFT+U approach exhibits strong dependence of the energetics and electronic structure results on the value of U. A specific choice of the projectors in the form of localized Wannier-Boyd functions [47, 48, 49], which can be obtained self consistently, allows for removing the strong dependency of the energetics on U.

The value of the parameter U is essential for the accuracy of the solution. The usual practice was to choose the value to achieve the agreement between the resulting properties such as the band gap of the insulator with the experiment.

However this causes loss of the ab initio character of the calculations. Good agreement with experiments was also obtained by calculating the value of U selfconsistently employing the linear response approach described in Ref. [45]. For the case of ceria the U was calculated in [46, 50] as 4.5 eV. This value has subsequently been used in many calculations of ceria based systems [51, 52, 53, 54, 55, 56].

Chapter 3

Simulating Cu/CeO_2 interfaces

In this chapter I will first describe the methods used to calculate properties of ceria based systems and difficulties arising from the peculiar electronic structure of reduced cerium oxides. Then I will summarize the results of my previous works, mainly the diploma thesis [57] and following publications [55, 58] which are relevant and strongly connected to the goals of this thesis (Figures and tables adapted with permission from the Journal of Chemical Physics. Copyright 2013, the American Institute of Physics.). I will introduce the calculations of bulk and surface properties of the individual constituents of the studied system, the copper and cerium oxides as well as the effects at the Cu/ceria interfaces. The general effect at the interface of Cu/ceria systems is the charge transfer across the interface and reduction of ceria as a result of contact with copper.

3.1 Calculation of ceria based materials

Cerium is a rare-earth metal which exists in two main oxidation states Ce^{3+} and Ce^{4+} corresponding to two different oxides, reduced cerium oxide Ce_2O_3 and ceria, CeO_2 respectively. The electron configuration of cerium is $1s^2$ $2s^2$ $2p^6$ $3s^2$ $3p^6$ $3d^{10}$ $4s^2$ $4p^6$ $5s^2$ $4d^{10}$ $5p^6$ $4f^2$ $6s^2$. Bulk ceria has a face-centered cubic (fcc) symmetry with one cerium and two oxygen atoms in a unit cell forming space group Fm3m, while the bulk reduced Ce_2O_3 crystallizes in two phases. The A phase is hexagonal with two cerium and three oxygen atoms in the unit cell forming a space group P-3m1 [59], while the C phase has cubic bixbyite symmetry. While in ceria the valence Ce states are empty, in reduced Ce_2O_3, one electron of each Ce^{3+} ion occupies 4f cerium band. The strong spatial localization of the Ce 4f states causes the inability of the standard energy functionals to correctly capture the self-interaction correction. As a result the standard DFT calculations are not able to consistently describe cerium ions in both oxidation states: Ce^{3+} and Ce^{4+}. Both forms of cerium oxide, Ce_2O_3 and CeO_2 are insulators, but standard DFT in the case of the reduced form Ce_2O_3 provides a wrong metallic solution with Ce f states partially occupied and crossing Fermi energy instead of the correct insulating solution with one Ce f state occupied and exhibiting sharp f peak below Fermi level.

First calculations of cerium oxide were performed by the means of linear

augmented-plane wave method in Ref. [60], where the mechanism of bonding in CeO_2 was studied. In Ref. [61] the Hartree-Fock method was employed to calculate electronic and thermodynamic properties of ceria. The resulting lattice parameter and bulk modulus exhibited discrepancies with experimental values of about 50%.

Different approaches were proposed and have been implemented in order to overcome the difficulty with the localization of f electron in reduced cerium oxides. One of the first methods was based on different description of Ce^{3+} and Ce^{4+} ions. While Ce^3 ion and thus the Ce_2O_3 oxide is described within core state model (CSM), where 4f states are treated as part of the core, the Ce^{4+} ions in CeO_2 are described according to a valence band model (VBM), where 4f electrons are regarded as a part of the valence band. This approach however is not able to correctly determine the oxidation state of the cerium ion, so the state has to be given as an input into a calculation. In the case of calculation of more complex systems, many configurations of the reduced ion placement have to be tested. In Ref. [62] this approach was used to calculate the electronic, bonding and optical properties of both forms of oxide, CeO_2 and Ce_2O_3 by the means of full-potential linear muffin-tin orbital DFT method. Adapting the CSM and VBM allowed to reach better agreement of the calculated results with experiment. In the next study from the same authors [63] the same approach was used to study oxygen vacancy formation in ceria and transformation between CeO_2 and Ce_2O_3.

The periodic Hartree-Fock calculations [64] and projector augmented-wave (PAW) DFT calculation [65] studies explored stability of different ceria surfaces and consistently reported (111) surface as the most stable.

A first DFT calculations revealing number of metastable states for reduced cerium oxide were reported in [46]. Within these metastable states, the most stable solution for reduced cerium oxide was indeed the physical one with the correct oxidation state. In particular the standard DFT calculation of electronic structure of Ce_2O_3 exhibited metallic solution with a single Ce 4f band partially occupied (see Fig. 3.1 (b)). One electron was distributed between three Ce f states. Further self consistent calculations performed from different initial conditions instead revealed a true ground state, which was insulating and exhibited one electron localized on each Ce ion. The Ce 4f states split resulting in one peak among occupied states (Fig. 3.1 (c)). Most stable state was shown as ferromagnetic, while antiferromagnetic states represented more metastable states. It was shown that addition of Hubbard-U term to the energy functional (LDA or GGA) enhances the stability of the correct physical solution (see Fig. 3.1 (d)). In the case of the Hubbard U contribution defined in terms of maximally localized Wannier functions, the resulting energy is independent on the U term.

Standard DFT exhibits metastable states also for the case of oxygen vacancy in ceria [46]. Upon oxygen removal two electrons are left behind. In standard DFT calculations these two electrons are equally divided between all the neighbouring Ce ions, which thus exhibit same outwards relaxation. When employing DFT+U calculations, a more stable solution is discovered, where the two electrons left behind are localized on two cerium atoms causing asymmetrical structure upon relaxation (see density of states, DOS in Fig. 3.1 (e)).

The choice of parameter U was discussed in detail in Ref. [49]. Parameter

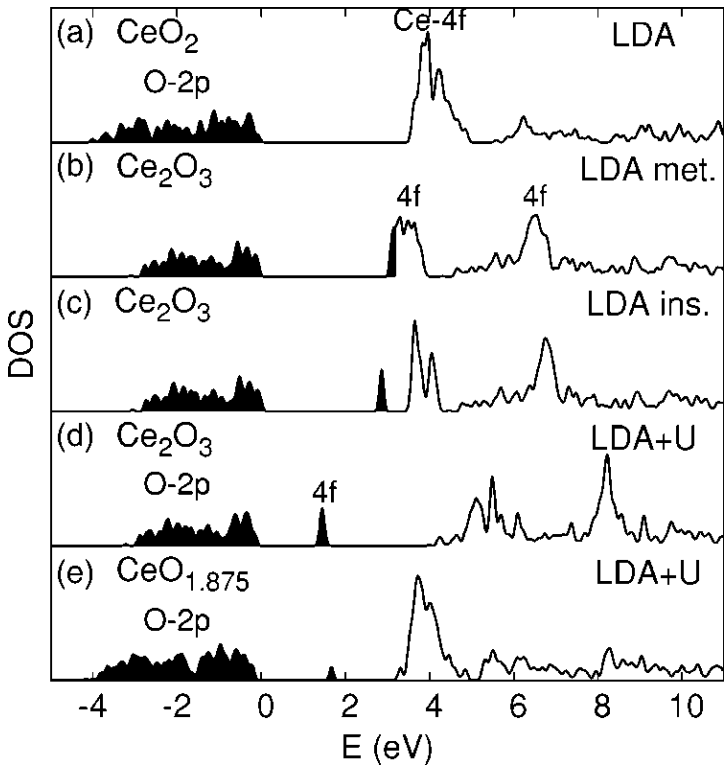

Figure 3.1: Density of states images for CeO_2 (a), Ce_2O_3 (b)-(d) and $CeO_{1.875}$. Occupied states are displayed dark. Reprinted figure with permission from Fabris et al. Phys. Rev. B 71, 041102, 2005 [46]. Copyright 2013 by the American Physical Society.

U is usually chosen semiempirically to fit the results with available experimental measurements. Good agreement with experiments was also achieved with U value calculated selfconsistently in [49, 50] using linear response approach described in [45]. DFT+U was then used to calculate electronic and structural properties of stoichiometric and defective ceria surfaces.

The effect of the value of the U parameter on the calculated electronic properties of stoichiometric and reduced cerium oxides was explored in [66]. The different stability of ferromagnetic and antiferromagnetic solutions was shown for different values of U. In [52] the dependence of the properties of CO adsorption on ceria surfaces on the U term was explored. It was shown, that to obtain results in agreement with experiment, the U=2 eV was required, while much higher value (above 4.5 eV) was necessary to get a correct electronic structure of ceria [46, 67, 68].

Since the first calculations many studies of ceria based systems have been reported employing DFT+U method as a standard method for dealing with ceria materials. However the problem of existence of metastable solutions appears frequently within calculations of ceria materials even within DFT+U method especially in the presence of Ce^{3+} ions such as near oxygen vacancies or adsorbed metal atoms.

Even though the DFT+U method is able to correctly predict the localization

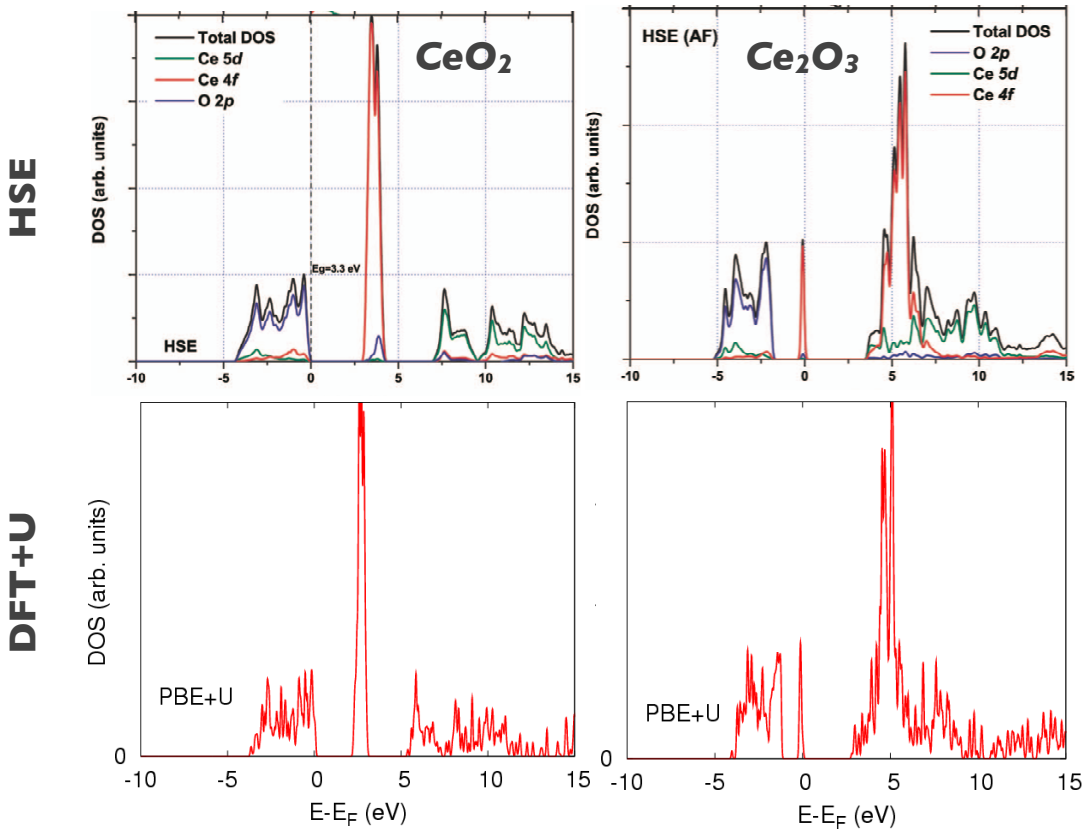

Figure 3.2: The DOS of cerium oxides CeO_2 and Ce_2O_3 calculated by DFT+U method (lower panel) and within hybrid functional approach (upper panel) as published in Hay et al. J. Chem. Phys. 125, 034712, 2006. Reprinted with permission from the Journal of Chemical Physics. Copyright 2013, the American Institute of Physics.

of two electrons on two Ce ions and thus their reduction, there is still a question of the exact location of those two Ce^{3+} ions. First studies reported the Ce^{3+} ions in the direct neighbourhood of the vacancy. Later calculations revealed many metastable solutions with reduced Ce ions in different positions away from the vacancy within the supercell [69, 70, 71, 72].

Another case of the complexity of DFT+U is described in [73] where not only the position of reduced Ce ion but also its spin adds to the number of possible metastable solutions different in energy for the case of oxygen vacancy in the VO/CeO_2 system. This behaviour is typical for the systems where ceria is doped by transitional metals [23].

Metal-oxide interfaces have been subjects of many recent studies. Metal-ceria systems are especially interesting since they have possible applications in heterogeneous catalysis, where the combined system can have greatly enhanced catalytic activity compared to standard metal or oxide catalysts. The smallest representatives of metal-oxide interfaces are metal adatoms and small metal clusters on ceria surfaces. Transition metals such as Pd [74, 75, 76, 77], Pt [78, 79, 76, 80, 77] and Au are most frequently studied due to the flexibility concerning oxidation

states [23, 81, 82]. Metal adsorption on stoichiometric ceria is connected with transfer of electrons from metal to ceria, causing ceria reduction. In case of Au [54, 81, 82, 83, 84, 85, 86], Ag [82, 87] and Cu [82, 55, 88, 89], one electron is transfered, Ga, In and Fe induce transfer of two electrons and three electrons are transfered from Al, La, Ce, V or Cr. Each electron transfered is localized on one Ce ion causing its reduction. The position of this reduced Ce ion as well as the exact oxidation state of the adsorbed metal contributes to the number of possible metastable solutions.

Another approach for the calculations of ceria-based materials is based on employing more sophisticated hybrid functionals based on mixing part of the exact nonlocal Hartree-Fock exchange with correlation functional such as described in Ref. [90, 91, 22] instead of using standard LDA+U or GGA+U functionals. This approach is able to overcome the kind of problems described in this chapter, however its application to the real problems is limited due to the high requirements for computing resources [92, 93]. As seen in Fig. 3.2 by comparing the DOS of cerium oxides calculated by the DFT+U method with the DOS calculated with hybrid functionals [90] we show that the DFT+U level of theory gives results within acceptable precision with lower demand for computing resources.

In the present work we show an extreme case of the limitation of the predictive power of DFT+U calculation for the metal-oxide interface. As reported in other systems, we observe a charge transfer connected with reduction of ceria at the CeO_2/Cu(111) interface containing four molecules of ceria and at least nine atoms of copper. This extended interface exhibits a large number of metastable solutions with respect to occupation of particular Ce f states depending on different initial electronic configuration of the scf calculation for system with the same atomic coordinates. A detailed description of the metastable solutions and the implications from their existence is reported in appendix.

3.2 Method

Our calculations are based on DFT using GGA approximation for the exchange-correlation functional in the formulation of Pedrew-Burke-Ernzerhof (PBE) [34]. The plane wave pseudopotential method is used as implemented in the PWscf code of the Quantum ESPRESSO distribution [94]. The interaction between valence electrons and ionic cores is represented by Vanderbilt ultrasoft pseudopotentials [40]. In order to provide the correct insulating description of Ce_2O_3, we use GGA functional with addition of the Hubbard-U term in the implementation of Cococcioni and de Gironcoli [45]. The value of the parameter U=4.5 eV is consistent with numerous works reported in literature for this system using the values between 4.5 and 5 eV [49, 68, 67, 95, 96, 83, 69] and was calculated by ab initio linear response model in Ref. [50, 49]. The structures are visualised by XCrysDen visualisation program [97].

The precision of the calculations is governed by three main parameters. In our plane-waves pseudo-potential formulation the three main parameters are the energy cutoffs for the basis function and density representation (E_{wfc}^{cut} and E_{rho}^{cut}, respectively) and the k-point mesh. E_{wfc}^{cut} determines the size of the basis set

used to describe the electronic pseudo wave function, but also controls the computational time and memory usage. The basis set includes all plane waves whose wave number $\vec{k}+\vec{G}$ verify the condition 2.14. Another parameter E_{rho}^{cut} controls the density representation and should be larger than 4*E_{wfc}^{cut} in the case of ultrasoft pseudopotentials. The integrals in the Brillouin Zone are calculated numerically using a finite grid of k points, chosen according to the Monkhorst-Pack grid [35] using the Methfessel-Paxton scheme [39] together with an energy broadening of 0.01 eV.

In [57] we performed convergence tests of total energy and lattice parameter for both bulk copper and ceria in order to determine the proper values of above mentioned parameters. As a result in the following calculations we use the E_{wfc}^{cut} 30 eV, E_{rho}^{cut} 300 eV and the Monkhorst-Pack k-point mesh of 8×8×8 and 12×12×12 for 1×1×1 cell of ceria and copper respectively.

3.3 Copper and cerium oxides

Copper is a transition metal crystallizing in fcc structure with lattice parameter of 3.61 Å [98]. Our calculated value 3.63 Å [57] is in good agreement with this experimental value. Previously reported calculations of Cu surfaces show, that to correctly describe surface properties of copper, 4 monolayers (ML) of copper separated by 14 Å thick layer of vacuum is sufficient. The crystal structure of copper is displayed in Fig. 3.3 (a), while the band structure and density of states taken from [57] in the same figure (b) and (c) respectively.

The equilibrium lattice parameter of ceria calculated in [57] 5.53 Å is higher than the experimental lattice parameter reported for this compound 5.41 Å [99], 5.411 Å [100, 101] and 5.406 Å [102]. The crystal structure of ceria together with band structure and density of states projected on individual atoms in the ceria unit cell (pDOS) is displayed in Fig 3.4. The pDOS picture show the oxygen p states located below the Fermi level and also the unoccupied cerium f states above the Fermi level. For comparison we show the crystal structure, band structure and density of states of reduced A-type cerium oxide Ce_2O_3 as well in Fig. 3.5. Compared to the pDOS of ceria, the f states of the cerium atoms in Ce_2O_3 exhibit a peak below the Fermi level. This peak correspond to the one electron occupying one of the f states and is typical sign of the reduction of the cerium atom from Ce^{4+} state to Ce^{3+} state. Both forms of cerium oxide exhibit insulating character.

3.4 Copper/ceria interfaces

Our previous calculations [57, 55, 58] report effects upon adsorption of copper adatom on stoichiometric and defective ceria (111) surfaces as a model of smallest copper/ceria interface. In agreement with other theoretical works in literature [82, 89] the most stable adsorption site of Cu adatom on stoichiometric ceria surface is shown to be the hollow site between three surface oxygen atoms, while the most stable site on the defective surface is a site just above surface oxygen vacancy.

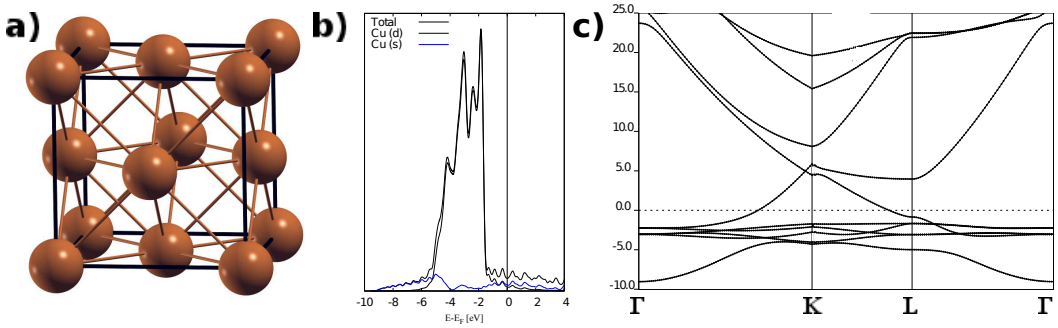

Figure 3.3: Crystal structure (a), band structure (b) and density of states (c) of bulk Cu crystal. Zero is set to the value of Fermi energy both in band structure and DOS figure.

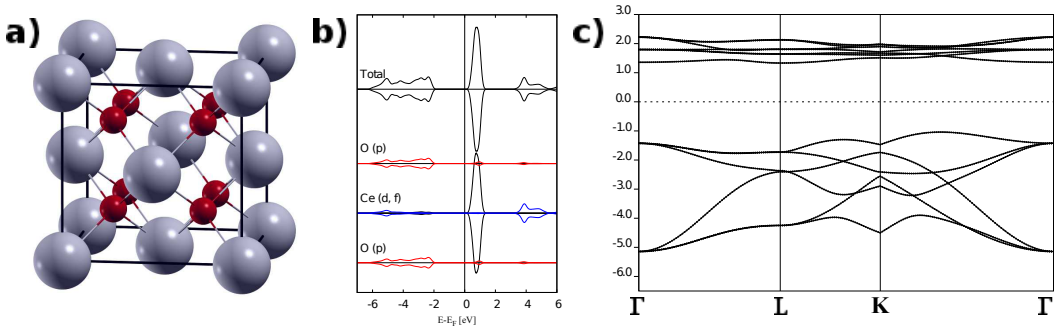

Figure 3.4: Crystal structure (a), band structure (b) and projected density of states (c) of bulk ceria crystal. The oxygen atoms are shown as small red balls, the cerium atoms are displayed as large grey balls. Zero is set to the value of Fermi energy both in band structure and pDOS figure. The red lines correspond to oxygen p states, while the blue and black lines to Ce d and f states respectively.

The corresponding structures together are displayed in Fig. 3.6 while the calculated electronic structure of this system is shown in Fig. 3.7 (a). Copper adsorption on stoichiometric ceria induces charge transfer from copper to ceria causing reduction of one cerium atoms from Ce^{4+} to Ce^{3+}. The reduction can be seen from pDOS image by the appearance of a sharp peak in Ce f states below Fermi level as well as in Table 3.1 from the value of magnetic moment of the system and lowdin charge on the cerium atom. The copper charges positively which can also be deduced from the Löwdin charge value.

Defective ceria surface was modeled by creating a surface oxygen vacancy in the stoichiometric (111) ceria surface. Presence of oxygen vacancy causes reduction of two cerium atoms in the surface. Copper adsorption on top of the vacancy exhibits opposite effect to the adsorption on stoichiometric surface. The charge transfer occurs in the opposite direction from ceria to copper causing reoxidation of one of the reduced Ce atoms and charging Cu adatom negatively 3.7 (b). The copper adsorption on stoichiometric ceria is more stable than on the defective surface. This is in contrast with other metals adsorbing on ceria

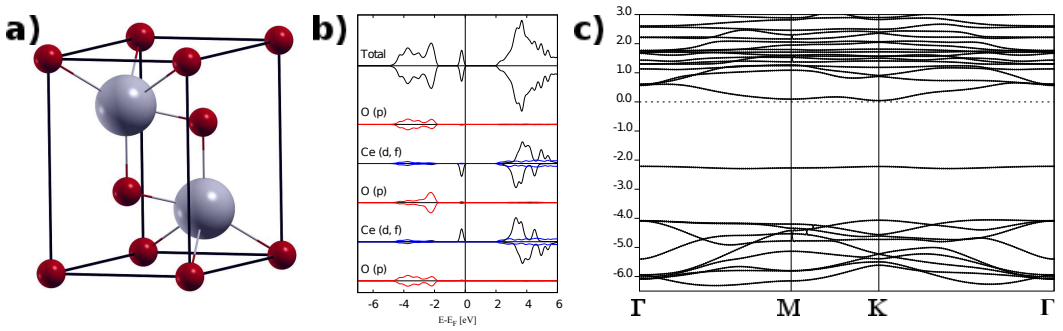

Figure 3.5: Crystal structure (a), band structure (b) and projected density of states of bulk A type hexagonal Ce_2O_3 crystal. The oxygen atoms are shown as small red balls, the cerium atoms are displayed as large grey balls. Zero is set to the value of Fermi energy both in band structure and pDOS figure. The red lines correspond to oxygen p states, while the blue and black lines to Ce d and f states respectively.

surfaces [83, 54, 79, 103] such as Au, Pt or Pd, but the same as Cu adsorption on for example titan oxide surfaces [104]. The contrast is ascribed to redox potential of copper. Calculated adsorption energies together with reported values are displayed in Table 3.2.

Our studies [55, 57] report also calculations of extended interface between Cu (111) and ceria (111) surfaces. The good match of lattice parameters of copper and ceria together with low energy electron diffraction (LEED) pattern [105, 106, 107] displaying 1.5 periodicity (see Fig. 3.8 (a) allowed us to use relatively small hexagonal supercell composed of (2×2) 3 ML ceria slab and (3×3) 4 ML copper slab. The charge transfer is observed also in the case of the interface. Contact with copper causes reduction of the whole first layer of cerium atoms. The study also examines the atomistic structure of the interface by exploring the mutual lateral shifts of one slab with respect to the other as well as the distance at the interface. The resulting structure at the interface is in fact the most symmetric one with one interfacial oxygen atom in the top position above one of the interfacial Cu atoms, while the other three oxygen atoms are in the bridge positions between two Cu atoms (see Fig. 3.6 (c)). The bondlengths and charge state (spin magnetic moment) of interfacial atoms is reported in the Table 3.2. The charge transfer and resulting ceria reduction is confirmed experimentally for example in [105]. The resulting X-ray photoelectron spectroscopy (XPS) spectrum of ceria before and after doping by copper clearly showing the reduction is displayed in Fig. 3.8 (c) together with an example of real copper/ceria catalytic system formed by copper doped ceria nanoparticles (b).

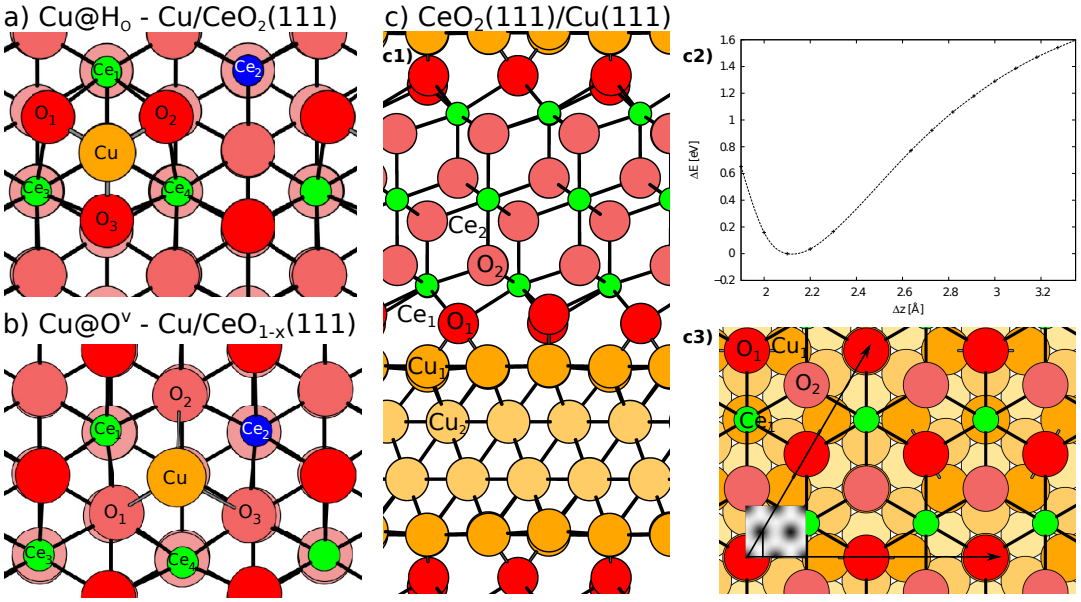

Figure 3.6: Adsorption geometry of Cu adatom on the stoichiometric (a) and defective (b) $CeO_2(111)$ surfaces. Structure of the $CeO_2(111)/Cu(111)$ interface (c) - side (c1) and top (c3) view of the supercell; total energy vs interfacial distance Δz (c2); energy plane of the relative displacement of metal and oxide slab in the inset in (c3).

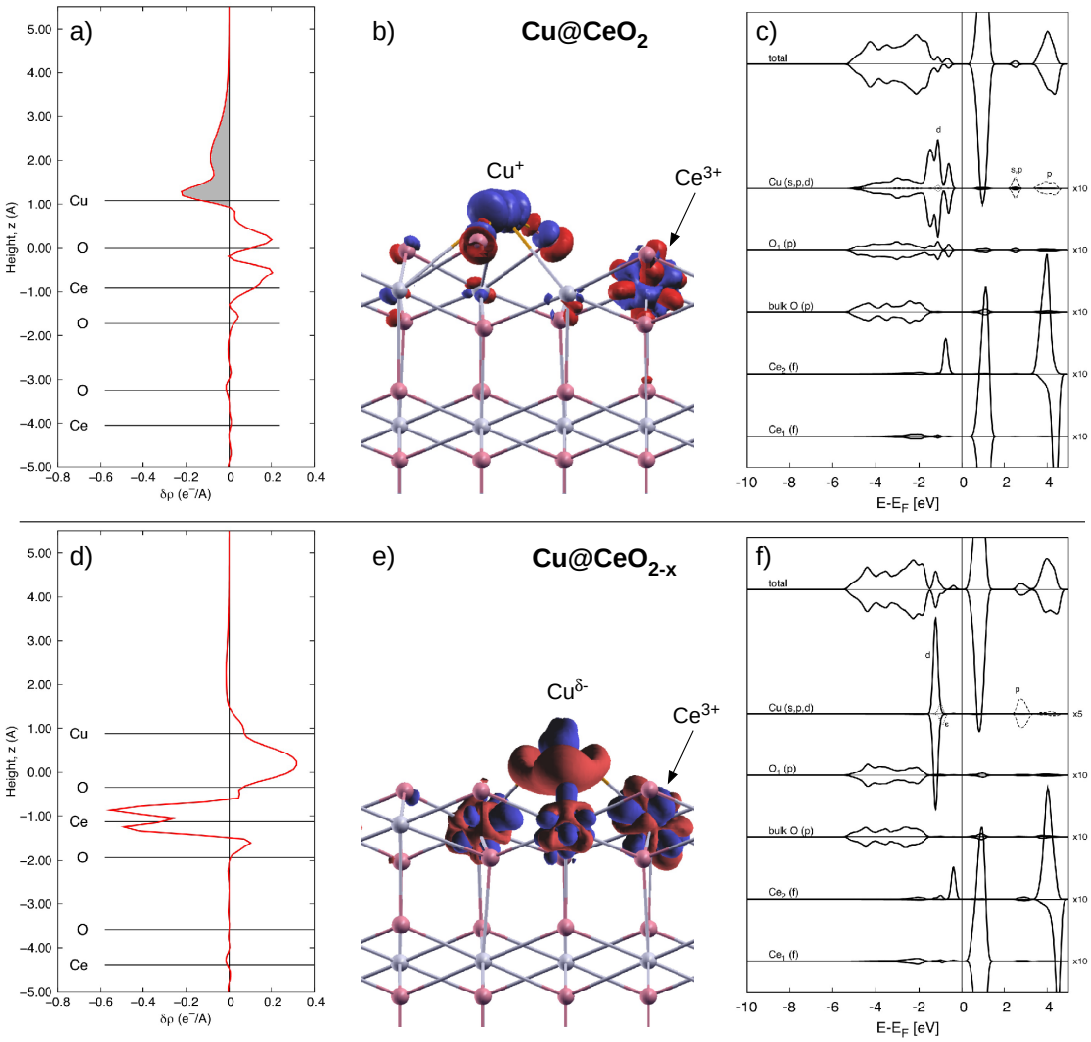

Figure 3.7: Bonding charge (a,b,d,e) and projected density of states (c,f) for Cu atom adsorbed on stoichiometric (a-c) and defective (d-f) ceria surfaces.

Table 3.1: Adsorption energy (E_{ads}) and free energy of formation (ΔG^0, calculated at $\Delta\mu = 0$); Spin magnetic moments of the Cu and Ce atoms (μ_{Cu} and μ_{Ce}); Elevation of the Cu adatom over the O atoms of the clean surface (d_z); Shortest Cu-O and Cu-Ce bondlengths (d) obtained from GGA+U (U=4.5 eV) calculations. Corresponding results obtained by setting the value of U to 2.5 eV or the lattice parameter to the experimental value are indicated in squared brackets and parenthesis, respectively. Corresponding values shown for the $Cu(111)/CeO_2$ interface: Spin magnetic moments of interfacial (Cu_1, Ce_1) and other (Ce_2) atoms and shortest Cu_1-O_1 and Cu_1-Ce_1 bonds.

	$Cu@H_O$	$Cu@O^v$	$Cu(111)/CeO_2$
E_{ads} [eV]	-3.03 $[-2.49]_U$ $(-2.86)_{a_0}$	-1.58	
ΔG^0 [eV]	0.47	4.39	
μ_{Cu} [μ_B]	0.00 [0.00] (0.00)	0.01	0.00 × 9 (Cu_1)
μ_{Ce} [μ_B]	1.01 × 1 0.00 × 3 [0.96] (1.00)	0.98 × 1 0.03 × 3	0.98 × 4 (Ce_1) 0.00 × 4 (Ce_2)
d_z(Cu)[Å]	0.91	1.22	1.58-1.89
d(Cu-O)[Å]	2.03 × 3	3.37 3.56 3.57	1.89 × 1 2.04 × 6
d(Cu-Ce)[Å]	2.89 × 3	3.09 × 2 3.20 × 1	3.12 × 1 3.28 × 6

Table 3.2: Adsorption energies of Cu adatom on stoichiometric and defective ceria surfaces compared to reported values for the same systems as well as different adatoms or different substrates as reported in literature.

substrate	ceria								titania
adatom	Cu	Cu		Au		Ag	Pd	Pt	Cu
reference	[55]	[82]	[89]	[83]	[54]	[82]	[103]	[79]	[104]
Stoichiometric	-3.03	-2.79	-2.68	-1.18	-1.18	-1.55	-1.71	-2.62	-1.76
Defective	-1.58		-1.46	-2.75	-2.29				-0.94

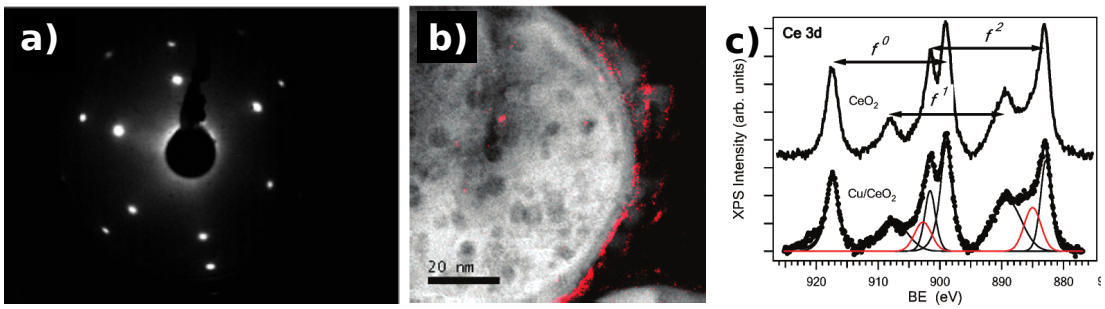

Figure 3.8: Low energy electron diffraction (LEED) pattern at 120 K at an electron energy of 98 eV for CeO_2 film on Cu(111) after annealing up to 970 K showing epitaxial growth of ceria with main axis aligned with the substrate and with the lattice parameter ratio 3:3 (a). High resolution transmission electron microscopy (HRTEM) image of copper doped ceria nanopowder with copper indicated by red color. A system representing a real copper/ceria catalyst and containing an example of copper/ceria interface (b). X-ray photoelectron spectroscopy (XPS) Ce 3d core level spectrum of pure and copper loaded ceria powder evidencing ceria reduction by the presence of copper (c). Adapted with permission from Matolín et al. J. Phys. Chem. C, 112, 3751-3758, 2008. Copyright 2013 American Chemical Society.

Chapter 4

Thin ceria films supported by Cu(111)

In this chapter I will describe results of my calculations on the new system composed of thin ceria films on Cu(111) surfaces. These results were published (Szabová et al. J. Phys. Chem. C , 116, 6677-6684, 2012) and are reported here with permission (Copyright 2013 American Chemical Society). In this chapter I will show differences in strain, atomic and electronic structure and behaviour of oxygen vacancies in 1 ML thin ceria film on copper substrate compared to the thicker films. This system is interesting as an inverse model catalyst as well as because it reproduces the local structure of systems where metal nanoparticles are encapsulated by metal-oxide.

4.1 Previous studies

In heterogeneous catalysis, oriented thin oxide films on metal substrates have traditionally been used as model systems mimicking the surfaces of bulk oxides [108]. Decreasing the thickness of the oxide films causes emerging of a broad range of effects that significantly influence the catalytic properties [109, 110]. When the oxide thickness reduces to few monolayers oxide stoichiometry, [111] electronic and crystalline structure [112, 113, 114], and charge of molecular adspecies [115] start to differ significantly from thicker films or bulk-truncated surfaces. Ultrathin oxide films are often discontinuous representing inverse model catalysts with unique catalytic properties [116, 117].

Continuous thin films on ceria have been prepared on Ru(0001) [118, 119] and Cu(111) [106, 120]. These films have served numerous model studies evaluating the catalytic properties of bare ceria surfaces [121, 122] as well as ceria surfaces activated with metal clusters [123, 124, 125, 78]. Discontinuous ultrathin films of ceria have been prepared on various metal substrates. Some of these ceria-based inverse model catalysts are showing exceptional activity in technologically relevant reactions like water-gas shift [126, 127] and CO oxidation [128, 129, 130]. Particularly, ceria on Cu(111) is a featured inverse model catalyst inspiring design of novel noble-metal-free industrial catalysts [127, 131]. Cu(111) substrate is convenient because of the 3:2 ratio of copper and ceria lattice parameters which

allowed to expect minimal mismatch and thus growth of thin ceria films with good epitaxy.

The high activity of inverse model catalysts is explained by a cooperative action of oxide and metal at the perimeter of oxide islands [126, 127, 128, 129, 130]. However, as first pointed out by Castellarin-Cudia et al. [132], the surface of ultrathin oxide islands in inverse model catalysts may itself incorporate catalytically active sites, which are not stable on thicker films and/or bulk oxide surfaces. Indeed, microscopic studies of 1-3 ML thick ceria islands on various metal substrates confirm that ultrathin ceria is strained [132, 133, 134], influenced by coincidence effects between substrate and oxide lattices [119, 120, 132], and shows several characteristic phenomena regarding oxygen vacancies, such as their ordering in coincidence structures [132, 133, 134] or their segregation at metal-oxide interfaces or at oxide surfaces in islands of various thickness (1 or more ML) [134].

4.1.1 STM study of ultrathin ceria films on Cu(111)

In our previous publication [56] we showed the differences in structure and morphology in ultrathin ceria layers (1-2 ML) on Cu(111) as obtained with atomic-resolution scanning tunneling microscopy. Room temperature STM experiment provided observation of ceria islands on Cu(111) substrate with large areas of 1 and 2 ML film. These samples were prepared either by titrating an oxidized Cu(111) surface with minute amounts of Ce (less than 0.1 ML) or by evaporation of Ce in a background oxygen atmosphere 5×10^{-5} Pa and substrate temperature of 400 °C. The STM images were obtained by tunneling the electrons into unoccupied states of the sample.

In order to analyze properties of ceria films of different thickness the samples were prepared with an increased amount of ceria of about 0.5 monolayer deposited at 460 °C. The islands shown in Fig. 4.1 (L-a) are composed of ceria monolayers stacked one on top of each other [120]. The islands are locally 1, 2, and > 2 ML thick and allow for a direct comparison of ceria layers with different thickness in one experiment. Step heights of the islands are 3.1 Å for 1 ML relative to unoxidized Cu substrate, 3.2 Å for 2 ML relative to 1 ML, and 2.9 Å for 3 ML relative to 2 ML, corresponding to a stack of complete ceria monolayers residing on unoxidized Cu substrate.

The triangular shape and orientation of the island is transferred from the first monolayer to higher monolayers. This indicates that the islands are coherent single crystals of ceria. Ceria islands exhibit different azimuthal orientations with respect to the copper surface. Two major populations of islands (45 % islands each) are represented by islands that are mutually rotated by 180°. These islands are marked "M" and "W" in 4.1 (L-a). Previous investigations of $CeO_2(111)/Cu(111)$ showed that the main crystallographic directions of ceria layer correspond to that of the copper substrate [106]. Thus, the ceria $[1\bar{1}2]$ direction must be parallel and antiparallel to the Cu $[1\bar{1}2]$ direction in "M" and "W" islands. A small number of ceria islands (10 %) show a random azimuthal orientation. An example of such island is marked "X" in 4.1 (L-a).

In a more detailed view, STM on the 1 ML ceria film reveals two characteristic patterns, one extending, on the lateral scale, for several nanometers (shown in

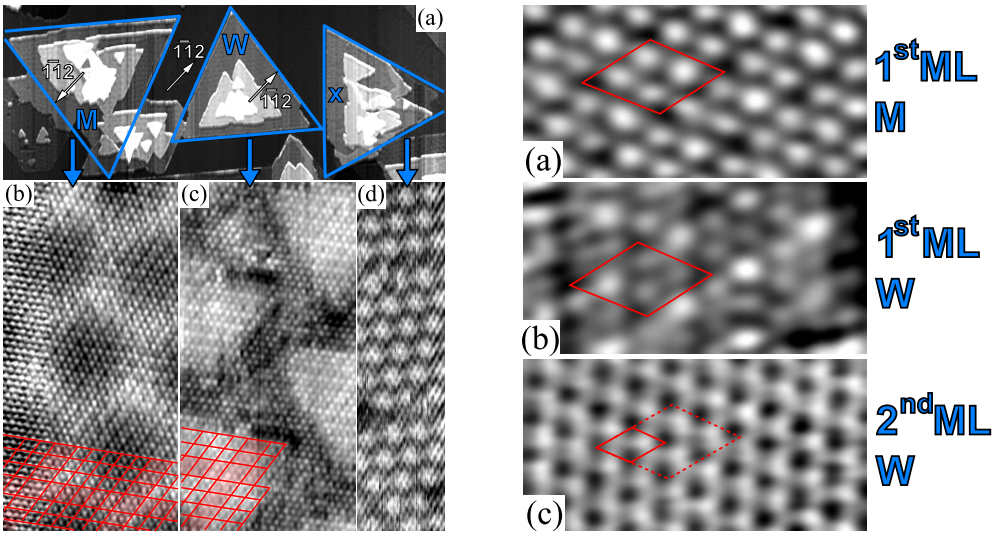

Figure 4.1: Ultrathin ceria islands grown on Cu(111) substrate with different azimuthal orientations of ceria with respect to the substrate (L-a). The "M" (Moiré, L-b) and "W" (wagon-wheel, L-c) represent majority of observed islands with ceria $11\bar{2}$ direction antiparallell and parallel to Cu $11\bar{2}$ direction, while "X" (L-d) displays small moiré surface reconstruction and represent 10% of islands with random orientations. Atomically resolved images of 1st ML of "W" (R-a) and "M" (R-b) islands. 2×2 pattern is visible for both orientations. The pattern vanishes in the 2 ML of ceria (R-c) and the surface becomes unreconstructed. The 2×2 and 1×1 unit cell for the 1 ML and 2 ML case respectively are highlighted by red lines.

Fig. 4.1 (L-b)-(L-d)), the other ranging in the order of Ångstroms (see Fig 4.1 (R-a), (R-b)). These patterns are largely suppressed or absent on the 2 ML or thicker ceria films as clear from Fig. 4.1 (R-c) and thus allow for drawing conclusions about the metal-oxide interaction, the strain buildup, and the localization of oxygen vacancies that are very specific for the first ceria monolayer on Cu(111).

1 ML ceria: strain

Morphological patterns on the lateral scale of nanometers can be traced back to the coincidence effects between ceria and the metal substrate. [120, 130, 133, 132, 119] Close observation of the islands show that these patterns in CeO_2/Cu(111) are strongly dependent on the azimuthal orientation of oxide islands. Typical morphologies observed by STM in the first monolayer ceria in "M", "W", and "X" oriented islands are shown in 4.1 (L-b)-(L-d). The change of the morphological pattern between "M" and "W" islands reveals the extent of the metal-oxide interaction in CeO_2/Cu(111), since for obtaining a change in the geometry of in CeO_2/Cu(111) upon 180° rotation of the oxide, at least two monolayers of Cu must interact with the oxide as shown in Fig. 4.2.

The STM pattern on the 1 ML ceria in "M"-oriented islands (4.1 (L-b)) corresponds to a moiré-like coincidence of substrate and adsorbate (111) planes with dissimilar lattice constant observed in many substrate-adsorbate systems [135].

In spite of the fact that ceria is expected to grow on Cu(111) pseudomorphically in an almost ideal 2:3 relation with a negligible 0.2 % expansion of ceria, electron diffraction experiments on ceria on Pt(111) [134] and on Cu(111) [136] reveal contraction of the ultrathin ceria films. Based on the periodicity of the moiré pattern the contraction of the 1 ML ceria on Cu(111) was estimated as 3.2 ± 0.3 %.

The morphology of the first ceria monolayer in "W" oriented islands (4.1 (L-c)) corresponds to a "waggon-wheel" superstructure which is a generalized moiré superstructure [137]. The atomically resolved detail in (4.1 (L-c)) shows a larger periodicity than the moiré structure on "M" islands (Fig. 4.1 (L-b)). However, on most "W" areas the waggon-wheel superstructure features a periodicity matching the moiré pattern on "M" islands, so no significant differences in contraction of ceria film with respect to substrate in "M" and "W" islands are expected.

The differences between superstructures in "M" and "W" islands can be discussed in terms of different relaxations of oxide and metal atoms. Indeed, changes in the registry of substrate and oxide atoms by a fraction of the interatomic distance significantly influence the STM contrast in ultrathin oxide films on metals [135, 132]. It was proposed that the relaxations of oxide atoms in "M" islands are minimal because the moiré pattern is obtained already for isotropic (111) lattices. In "W" islands the relaxations of oxide atoms may be more pronounced to induce a departure from the moiré pattern towards the waggon-wheel pattern. The "X" islands with random orientations display variety of smaller moiré patterns with different periodicities, stripe patterns, random height modulation or no height modulation. An example is shown in Fig. 4.1 (L-d).

1 ML ceria: oxygen vacancies

Apart from patterns on the nanometer scale, 1 ML ceria in "M" and "W" islands shows modification to the 1×1 atom pattern of $CeO_2(111)$. The islands exhibited areas of 2×2 reconstruction (in Fig. 4.1 (L-b), (L-c) marked by red lines) that are locally, and in registry with the moiré pattern, interleaved with stripes showing rather 3×2 reconstruction. On "M" islands, regular 2×2 or 3×2 patterns cover the entire surface of the 1 ML ceria, while on "W" islands, the 2×2 or 3×2 is localized among less ordered areas.

A detailed view of the 2×2 reconstruction in "M" and "W" islands is shown in 4.1 (R-a), (R-b), respectively. A unit cell of the 2×2 reconstruction, marked in the images by red lines, is composed of one bright and three darker protrusions as well as one darker and three brighter depressions. The unit cell is rotated by 180° between "M" and "W" islands in accordance with the orientation of the ceria layer in these islands. 2×2 reconstructions on the surface of bulk ceria [138] as well as on thin ceria films [134] have been interpreted as a fingerprint of subsurface oxygen vacancies. Thus it can be expected that the first ceria monolayer on Cu(111) includes oxygen vacancies at the ceria/Cu interface. Given the long range periodicity of the 2×2 pattern the vacancies are forming a regular array perturbed locally (in 3×2 areas) by coincidence effects between substrate and oxide layer.

2 ML ceria

In 2 ML thick areas of both "M" and "W" islands the 2×2 surface reconstruction disappears as shown in Fig. 4.1 (R-c) for "W" island. This indicates a different behaviour of oxygen vacancies in 2 ML and thicker ceria similar to observations of ultrathin ceria on Pt [134]. From the patterns on the nanometer scale observed in 1 ML ceria only moiré on "M" islands becomes partly visible in 2 ML ceria which indicates a significantly reduced influence of the substrate. The moiré in 2 ML ceria reveals a reduced contraction of 2.4 ± 0.3 %.

4.2 Calculation details

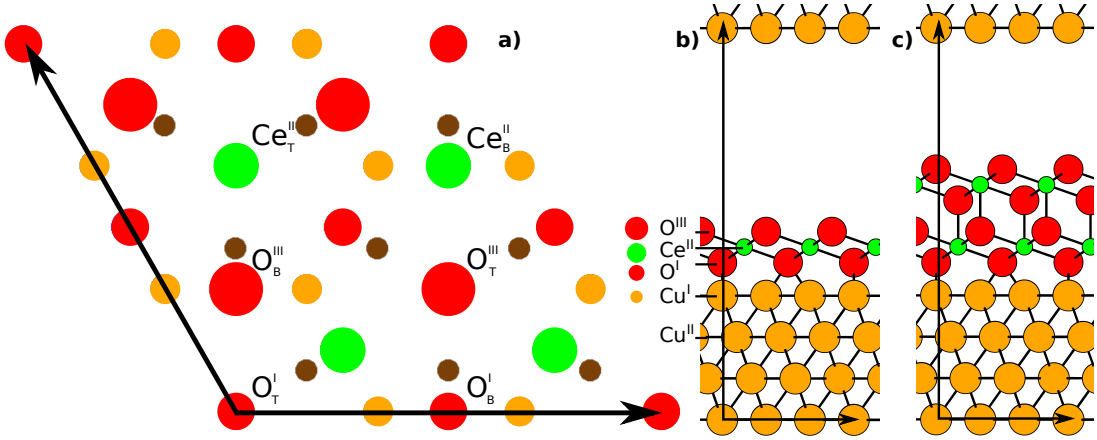

Figure 4.2: Top view of the 1 ML CeO_2/Cu(111) interface (a). Side view of a supercell for calculations of 1 ML (b) and 2 ML (c) CeO_2/Cu(111) systems. The different atoms are distinguished by color (a,b,c) and size (a) of the circles. Labels in the panel (a) correspond to different symmetry inequivalent sites due to the effect of the interface.

Also the calculations of the thin ceria films on Cu(111) were performed in the same way as our previous studies [57, 55, 58] and described in previous chapter. Spin-polarized DFT+U calculations employed PBE functional in the plane-wave pseudopotential method. The electron-ion interaction was represented by Vanderbilt ultrasoft pseudopotentials. The calculations were done by PWscf code of Quantum ESPRESSO distribution. The value of U was set to 4.5 eV in agreement with previous studies [49, 68, 67, 95, 96, 83, 69]. The plane-wave basis set and electron density representation were limited by energy cutoffs of 30 and 300 Ry in agreement with convergence tests reported previously.

The ultrathin films CeO_2/Cu(111) were modeled by means of hexagonal and orthorhombic supercells for stoichiometric and defective ceria film respectively, comprising one or two ML (O-Ce-O trilayer) (2×2) CeO_2(111) film in contact with a 4-layer (3×3) Cu(111) slab. The external surfaces were separated in the perpendicular direction by 11 Å of vacuum. The starting local structure of the interface was obtained in previous calculation described in [55, 57] by exploring energy landscape of the mutual shifts of ceria with respect to copper as well as

the distance of the slabs at the interface. The resulting structure at the interface was the most symmetric one, displayed in the Fig. 4.2 (a). One interfacial oxygen atom O_T^I is localised on top of one of the interfacial Cu_T^I atoms and thus has a different local environment than the other three interfacial oxygen atoms O_B^I which are in the bridge positions between two Cu_B^I atoms. This effect is then propagated to the higher atomic layers causing one atom (Ce_T^{II}, O_T^{III}) in each atomic layer of ceria slab to be different from the other three (Ce_B^{II}, O_B^{III}). The atomic positions of the metal/oxide interface and of the ceria thin film were optimized according to the Hellmann-Feynman forces. During the relaxation the two bottom Cu layers were kept fixed in their bulk-like position. The lattice parameter of the free-standing ceria slabs was calculated by relaxing all internal degrees of freedom for a set of lattice parameters a.

4.3 Results

4.3.1 Strain and structure of thin films

The experimentally observed moiré pattern on the 1 ML ceria film points to a contraction of the ceria film with respect to its equilibrium bulk lattice parameter. Our DFT calculations show that this is a size effect stemming from the confined dimensions of the slab in the perpendicular direction. Indeed, the lattice parameter a of an unsupported 1 ML ceria slab results to be smaller than the bulk CeO_2 value (a_0) by 6.7 % (see Table 4.1). On one hand, this contraction in the lattice parameter of thin ceria films quickly decreases as a function of the number of layers: the difference is reduced to 3.7% already for a 2 ML ceria slab. On the other hand, the strain is considerably reduced by the presence of O defects and reduced Ce ions as shown by the smaller contractions displayed by unsupported defective $CeO_{(1.75)}$ (4.1 %) and Ce_2O_3 (2.8 %) monolayers. Our calculations therefore provide evidence of the lateral contraction of thin stoichiometric ceria films with respect to bulk CeO_2 and demonstrate that oxygen vacancies together with reduced Ce^{3+} ions in the slab allow for reducing the lattice mismatch between 1 ML ceria films and the copper crystal. Thicker stoichiometric 2 ML CeO_2 slabs display a much smaller contraction than 1 ML CeO_2. Ceria films thicker than 1 ML can therefore yield small strain build-up at the interfaces with Cu(111), even in the absence of crystal and electron defects.

The 1 ML ceria thin films present a completely different behaviour than thicker ceria films with respect to the location of O vacancies. The calculated relative energetics of an O vacancy in the symmetry inequivalent sites of 1 and 2 ML CeO_2/Cu systems is reported in Tab. 4.2. The symmetry-inequivalent sites are defined in the top and side views of the supported ceria films displayed in Fig. 4.2. The calculations show that O vacancies tend to segregate at the metal-oxide interface in the case of 1 ML ceria film with a driving force of -1.2 eV. Among the two inequivalent O sites at the interface, the vacancy at the O site on top of a Cu atom (O_T^I) is more favoured than at the O site bridging between two Cu atoms (O_B^I) by 0.38 eV. In the case of thicker ceria films, an oxygen vacancy in the same (2×2) lateral supercell would instead segregate at the outermost surface layer

Table 4.1: Equilibrium lattice parameter (a) of unsupported stoichiometric and defective cerium oxide layers, and corresponding difference with respect to the bulk value of CeO_2 (a_0).

	a(CeO_2) [Å]	$(a - a_0)/a_0$ [%]
Bulk CeO_2	3.91	–
1 ML CeO_2	3.65	6.7
1 ML $CeO_{(1.75)}$	3.75	4.1
1 ML Ce_2O_3	3.80	2.8
2 ML CeO_2	3.76	3.7
3 ML CeO_2	3.80	2.8

(O^{VI}), where it is more stable by 1.08 eV with respect to the interface position (O^I_T). These structural and energetics analysis thus suggest that O vacancies in the 1 ML ceria film reduce the lateral strain and that they are located at the metal/oxide interface. As a consequence of the strong preferential interface segregation, O vacancies are predicted to be subsurface in the 1 ML ceria films.

Table 4.2: Energy difference (ΔE) between structures containing O vacancies at symmetry-inequivalent O sites of the first interface layer (O^I) with respect to the outermost surface sites (O^{III} and O^{VI} in the 1 ML and 2 ML ceria slabs, respectively). Labelling of O sites is defined in Fig. 4.2.

	site	ΔE [eV]
1 ML $CeO_{1.75}$/Cu	O^I_T	-1.20
	O^I_B	-0.82
	O^{III}_B	–
2 ML $CeO_{1.875}$/Cu	O^I_T	+1.08
	O^{VI}	–

4.3.2 Electronic structure

The analysis of the electronic structure allows to explain the fundamental difference in the O-vacancy segregation at the interface between 1 and 2 ML ceria films reported above. The interface between the stoichiometric thin ceria film and a copper surface displays a charge transfer from the metal to the oxide, yielding electron localization and reduction of all the interfacial Ce ions to Ce^{3+}. This interfacial effect, observed also in the case of thicker ceria films [55], is clearly displayed by the spin polarisation of the cerium atoms (see spin density in 4.3) and by the charge population analysis of the Cu atoms reported in 4.3. The latter shows the difference of the Löwdin charge of the Cu atoms with respect to the bulk value. For the case of the stoichiometric 1 ML CeO_2/Cu system, the data clearly support the charge depletion (oxidation) of the Cu atoms in the first interfacial layer (Cu^I) with respect to the deeper and bulk-like metal atoms (Cu^{II} and Cu^{III}). The Cu atoms displaying the largest variations are the closest to the interfacial O atoms, namely the Cu atom with an O atom on top labeled

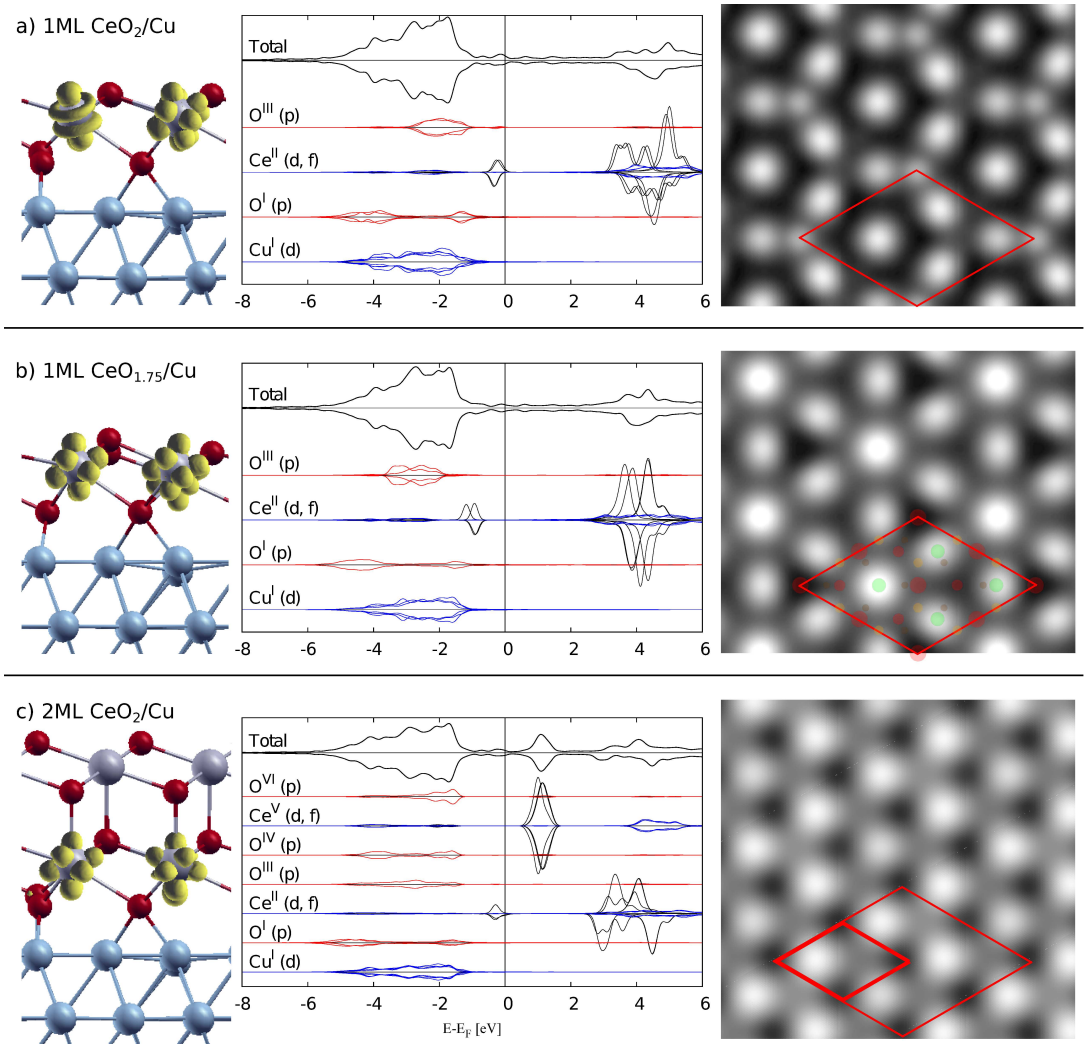

Figure 4.3: Spin density (left), projected density of states (middle) and simulated STM images (right) of 1 ML CeO_2/Cu(111) (a), 1 ML $CeO_{1.75}$/Cu(111) (b) and 2 ML CeO_2/Cu(111) (c) systems. In the pDOS figures the zero is set to the Fermi energy, red blue and thin black lines correspond to p, d and f orbitals respectively. Color coding displayed in right panel (b) is explained in Fig. 4.2

as $Cu^I(O^I_T)$, and the six ones connected to a bridging O labeled as $Cu^I(O^I_B)$. The Cu atoms further to and in hollow position with respect to the interfacial O atoms are also oxidized but by a minor extent.

Creating an oxygen vacancy in the bulk or at surfaces of ceria is usually accompanied by the localisation of two excess electrons at two Ce^{4+} ions, leading to their reduction to Ce^{3+}. [49, 69] This is not possible in the case of vacancy formation at the 1 ML CeO_2/Cu(111) interface, since all the cerium atoms in the film are already in the 3+ state. The excess charge originating from the presence of the O vacancy results to be localized at the metallic Cu/oxide interface. This is supported by the calculated charge analysis for the defective 1 ML $CeO_{(1.75)}$ film (4.3), which indicates an excess of charge at the interfacial Cu atoms with respect to the stoichiometric case. In particular, the Cu atom displaying the largerst variation is the one directly below the O vacancy, $Cu^I(O^I_T)$, while the

Table 4.3: Difference in the Löwdin charge of the Cu atoms in the I- and II-layers (Cu^I and Cu^{II} respectively) with respect to the bulk-like value.

	1 ML CeO_2/Cu	1 ML $CeO_{1.75}$/Cu	2 ML CeO_2/Cu
$Cu^I(O_T^I)$ [×1]	-0.3	0.0	-0.3
$Cu^I(Ce_T^{II})$ [×1]	-0.1	0.0	-0.1
$Cu^I(O_T^{III})$ [×1]	-0.2	-0.2	-0.2
$Cu^I(O_B^I)$ [×6]	-0.3	-0.2	-0.2
Cu^{II} [×9]	-0.1	-0.1	-0.1

charge on the other Cu atoms is only marginally affected by the presence of the vacancy. A further support of this effect is given by the calculated density of electronic states of the 1 ML CeO_2/Cu and $CeO_{1.75}$/Cu systems (shown in Fig. 4.3), displaying the same degree of reduction of the four Ce ions, but a different position of the Fermi level crossing the Cu *s*-band.

A thicker 2 ML ceria film displays an opposite behaviour than the 1 ML case with respect to the position of O vacancies. Our calculations predict that this difference has an electronic origin. The spin density (see 4.3 (c), left panel) shows that the effect of the interface on the reduction of the cerium atoms extends up to the first monolayer, while the second monolayer is formed exclusively by Ce^{4+} atoms. Reduced thicker ceria films can therefore easily localise the excess electrons on the Ce^{4+} sites of its second monolayer.

4.3.3 Atomistic structure

The difference between supported 1- and 2 ML ceria films is also apparent in the local atomistic structures of the surface atoms, whose electronic states are probed by the STM tip. As was described before, the symmetry of the interface causes one of each 4 atoms in the atomic layer of ceria feel different local environment than other three. This results in one 1.91 Å $Cu^1(O_T^I)$-O_T^I bond and six 2.05 Å $Cu^I(O_B^I)$-O_B^I bonds for the case of stoichiometric ceria film on Cu(111). Due to the presence and periodicity of the underlying copper atoms, the one symmetry-inequivalent O atom (O_T^I) relaxes away from the interface by 0.35 Å. This displaces outward the three neighboring cerium atoms Ce_B^{II} by 0.11 Å with respect to the other cerium atom in the supercell (Ce_T^{II}). The coherent and stoichiometric 1 ML CeO_2/Cu interface therefore induces structural changes that differentiate one of the four O and Ce atoms in each atomic layers up to the surface plane, thus resulting in an effective (2×2) periodicity at the surface of the thin film.

The presence of the O vacancy at the O_T^I interfacial site of the 1 ML $CeO_{(1.75)}$/Cu(111) system has a qualitatively similar but more pronounced effect on the outermost surface atoms. The lowest-energy site for vacancy formation is in fact the most symmetrical O_T^I site. The O vacancy induces a shift of the three neighbouring cerium atoms away (both in the vertical – by 0.31 Å, and horizontal – by 0.12 Å directions). The other Ce_T^{II} atom is not only geometrically distinct from the other three Ce_B^{II} atoms, but is the only one that is six-fold coordinated. At the interface, this atom repulses the neighbouring interface oxygen atoms by 0.23 Å,

leading to an increase of the six interface Cu-O_B^I bonds to 2.09 Å. At the surface, one O_T^{III} atom protrudes by 0.43 Å with respect to the other three surface O_B^{III} oxygen atoms. Therefore, also in this case, the surface of the thin film has an effective (2×2) structural periodicity.

Instead, for the case of thicker films, the structural effects of the interface do not propagate up to the surface atoms. The stoichiometric thicker (2 ML) ceria film displays the same interface structure of the 1 ML case, but the structural differentiation of atoms in each atomic layer is negligible for the outermost O-Ce-O trilayer, and the surface of the supported film has an effective (1×1) periodicity, both in terms of local atomistic and electronic structures.

4.3.4 Simulated STM images

This different periodicity of 1 ML and 2 ML supported ceria films is reflected in the simulated STM images reported in Fig. 4.3. In order to allow for a direct comparison with the experiment (measured at positive bias), we report in the figure the STM images calculated for the unoccupied states. In these conditions, the bright spots are associated to the Ce ions, as clearly shown by the projected density of states reported in the middle panels of Fig. 4.3 for the Ce and O atoms. In the energy window relevant for the comparison with experiment, the contribution of the oxygen states is negligible.

A representative simulated STM image for the 1 ML CeO_2/Cu system is displayed in Fig. 4.3 (a), and presents important differences with the experimental micrograph of Fig. 4.1 (R-a),(R-b). In particular, the simulated STM image displays a large darker area around the symmetry inequivalent Ce_T^{II} site, which is not observed in the experimental data. A better agreement is not obtained by calculating the STM image at different biases or by plotting the integrated charge on planes at different distance from the surface. On the other hand, for a wide range of biases and sample-plane distances (0-3 eV and 0.35-2.0 Å, respectively), the simulated STM image of the defective 1 ML $CeO_{1.75}$/Cu system presents a much better agreement with the experiment (see Fig. 4.3 (b)). The calculated pattern displays a (2×2) periodicity of four spots (one of which brighter than the others) and of two darker areas (one of which darker than the other). By superimposing the atomic positions on the simulated STM image it is possible to associate the brightest spot and darkest areas to the Ce_T^{II} and O_T atoms, respectively. This similarity between the simulated STM image for the defective 1 ML $CeO_{1.75}$/Cu system and experimental images further supports the presence of vacancies at the interface between the 1 ML ceria film and copper.

Quite differently, the simulated STM image of the 2 ML CeO_2/Cu system (in Fig. 4.3 (c)) displays a 1×1 pattern of brighter and darker spots, which is in very good agreement with the images of the 2 ML ceria observed in STM. This therefore confirms that the 2 ML ceria film is stoichiometric.

4.3.5 Orientation of 1 ML ceria film

In the following, we investigate the possible origins of the two types of islands experimentally observed. We have so far calculated and described the most stable

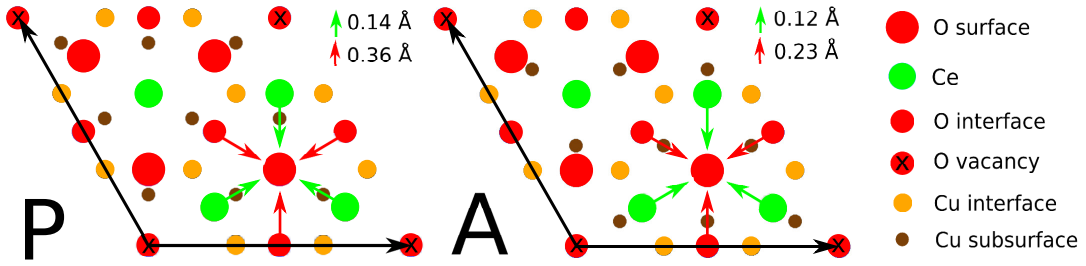

Figure 4.4: Paralell (left) and antiparalell (right) orientations of 1 ML ceria on Cu(111). Directions of atomic relaxation induced by creating of an oxygen vacancy at the position indicated by "×" are indicated by arrows, the average magnitudes of the relaxation are specified for each orientation in the inset.

structure of the 1 ML $CeO_{1.75}$/Cu with the oxygen vacancy at the O_{I1} site where the $[1\bar{1}2]$ directions of ceria and copper are antiparallel ("A" in 4.4). There is another configuration of this 1 ML $CeO_{1.75}$/Cu interface, in which the two $[1\bar{1}2]$ directions are parallel ("P" in 4.4). Differences between the two orientations arise when considering the subsurface copper atoms (brown circles). Calculated atomic relaxation in the "P" and "A" orientations are graphically represented by colored arrows in 4.4 with magnitude in Å indicated in the insets. Interface "P" induces larger horizontal relaxations than interface "A" by 0.13 Å for the interface oxygen atoms and by 0.02 Å for the cerium atoms. This can be explained by the different interaction of interface oxygen atoms with the copper atoms in the subsurface layer, considering that in the "A" supercell the oxygen atoms are forced to move horizontally closer to the subsurface copper atoms due to the presence of the vacancy. As a result the atoms in all atomic layers in the ceria layer relax vertically to a higher level in the "A" supercell than in the "P" case. In addition, the "A" orientation turns out to be energetically more favourable than the "P" orientation by 0.12 eV. This small energy difference is consistent with the comparable frequency of occurence of two types of islands in the experimental data.

Establishing a correspondence between calculated "P" and "A" orientations and "M" and "W" islands in experiment is difficult, because the supercell size used in our calculations is too small to capture the long-range moiré (which develops over more than 14 unit cells) or "waggon-wheel" structures. However, on the basis of the calculated energy preference of the "A" orientation as well as its smaller relaxation magnitudes and larger vertical accommodation, we tentatively propose that the "A" orientation corresponds to the locally better-accomodated "M" islands.

4.4 Study of strain distribution in ceria islands on Cu(111)

Further analysis of previously described STM images of triangular ceria islands on Cu(111) substrate was focused on exploring the strain distribution in the thin films due to the change of lattice parameter of the film with increased film

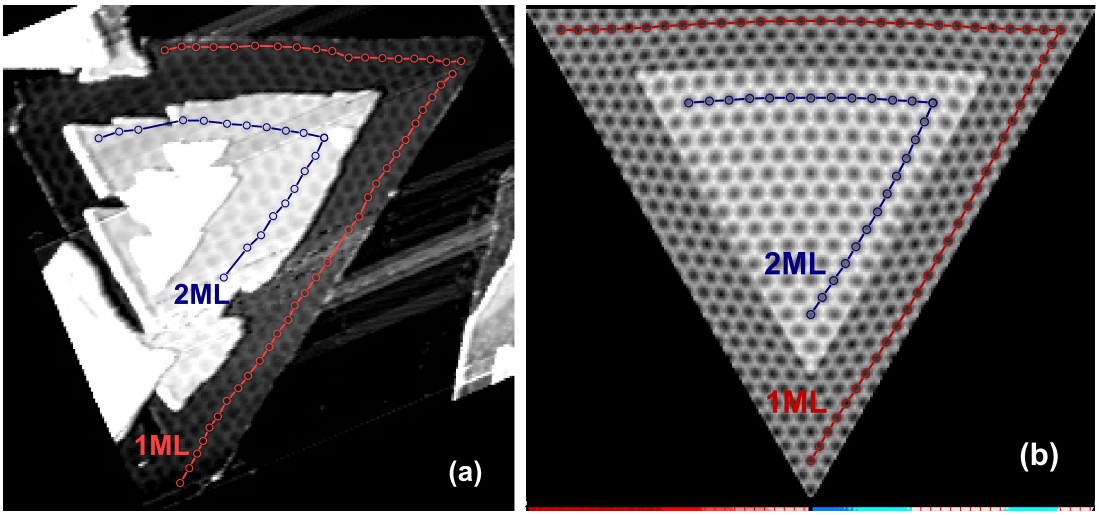

Figure 4.5: Inhomogeneously strained multilayer island of ceria on Cu(111) (a). 1 ML and 2 ML label the first and second ceria monolayers. Rings are centers of moiré spots. Simulation of moiré on a strained 2 ML island by the finite elements method (b). Reprinted with permission from Stetsovych O. et al. Phys. Rev. Lett. 109, 266102, 2012. Copyright 2013 by the American Physical Society.

Table 4.4: Lateral contraction of ceria layers of different thickness with respect to bulk lattice constant as obtained by fitting from moiré pattern in STM images and by DFT+U calculations of equilibrium lattice parameter of unsupported stochiometric ceria layers.

	Contraction [%]	
	STM	DFT+U
1 ML CeO_2	3.2	6.7
2 ML CeO_2	2.4	3.7
3 ML CeO_2	1.9	2.8

thickness. The method described in Ref. [139] is based on standard method of fringe counting from classical moiré interferometry and allows for nanometer-scale resolution of inhomogeneous two dimensional strain in incommensurate layered systems.

The moiré pattern is able to reveal even tiny variations in the registry of the lattices and thus also small changes in the lattice constant [140] or azimuthal registry of the lattices [137]. In the triangular ceria islands, the moiré pattern was observed on the first monolayer showing the contraction of ceria layer of 3.2% and also on 2nd monolayer with larger periodicity corresponding to contraction of lattice parameter for 2.4%. In the area of the second monolayer the moiré was isotropic, while in the case of first monolayer it was anisotropic on the sides of islands with periodicity elongated along the edge of the islands indicating a presence of further strain in the first monolayer. In table 4.4 adapted with permission from [139] we show the contraction of ceria films with different thickness calculated as the compression of the lattice parameter of unsupported ceria films

with respect to the bulk lattice parameter. The values clearly show the decrease in compression with increase of the thickness of the film. The result is in agreement with the trend observed for the values of compression obtained by fitting the moiré pattern in STM images. Thus our ab initio calculations predict the driving force for the strain caused by the quantum-mechanical size effect related to a limited thickness of the layer. The strain observed in the triangular islands is induced by larger lattice parameter of the 2 ML film compared to lattice parameter of the first monolayer which causes outwards relaxation of the edges of 1 ML film. This is also possible due to the free gliding of ceria films on copper substrate allowed due to the low variation of binding energy of the copper/ceria interface for different mutual lateral shifts predicted by DFT+U calculations in Ref. [55].

4.5 Conclusions

In this chapter I presented physical and chemical properties of ultrathin ceria films on Cu(111) substrate. I showed that the 1^{st} monolayer of cerium oxide on Cu(111) is strained as a result of a size effect of the limited dimension of the film. The larger lattice parameter of 2 ML film in the ceria island was shown to induce inhomogeneous stress into the first ceria monolayer along the island edges. The 2×2 pattern observed in STM images was identified as an ordered array of subsurface oxygen vacancies in the 1^{st} ceria monolayer. The different behaviour of oxygen vacancies in the 1 ML film compared to thicker films was explained by the electronic effect of the interface with metal, which cause all the interfacial Ce atoms to be in a 3+ state. Electrons left by the vacancy creation are not able to localize on Ce atoms, instead they transfer to the metal substrate. This is not necessary for thicker films which can localize electrons at Ce^{4+} atoms in further layers.

Both oxygen vacancies and Ce^{3+} ions help to relieve the strain in the thin ceria film. The effect of the interface between metal and oxide reach to the 1^{st} ceria monolayer and to the subsurface Cu atomic layer. Already 2 ML ceria film exhibit surface similar to the (111) termination of bulk ceria crystal and standard behaviour of oxygen vacancies. The distinct physico-chemical properties of the first ceria monolayer likely play a significant role in the enhanced reactivity of inverse model ceria/Cu catalysts where 1 ML ceria represents the most extended surface phase.

Oxygen vacancies on clean ceria surfaces are usually regarded as catalytically active sites. They contain both structural defect and Ce^{3+} ions. Whether the catalytic activity comes from the missing oxygen or from the different charge state of Ce atom is not clear. In this perspective, the ultrathin ceria films on copper present three very interesting systems. One of them, the 2 ML CeO_2/Cu(111) has atomistic structure of the surface monolayer similar to the (111) surface of bulk ceria crystal and its top cerium atomic layer contains only Ce^{4+} ions as standard CeO_2(111) surface. Compared to that, the 1 ML CeO_2/Cu(111) system has also similar atomistic structure to the previous case, but contains only Ce^{3+} ions. Last the 1 ML $CeO_{1.75}$/Cu(111) system contains also exclusively Ce^{3+} ions but also

deviates from the CeO_2 stoichiometry by presence of an oxygen vacancy. These three systems are thus ideal candidates for study the mechanism of adsorption on ceria surfaces and to determine and separate the role of electronic (Ce^{3+} ions) and structural (oxygen vacancy) defects during the adsorption. The extra charge in the 1 ML ceria can affect adsorption properties of molecules by providing a charge donation to adsorbates capable of accepting electron or allowing for adsorption structures and states not available at stoichiometric surfaces. The effects of these structural defects on the reactivity of the copper-ceria systems are described in the next chapter.

Chapter 5

H_2O adsorption

In this chapter I will investigate how the special properties of the ultrathin ceria layers on Cu(111) substrate described in the previous chapter namely the different charge state of Ce atoms in the top layer of films with different thickness affect the H_2O adsorption on ceria surface. I will show results of study of H_2O adsorption and dissociation on 1 ML CeO_2, 1 ML $CeO_{1.75}$ and 2 ML CeO_2 films specifically with aim to provide better understanding of the mechanism of H_2O adsorption and dissociation and of the role of structural and electronic defects for the adsorption.

5.1 Previous studies

Understanding the mechanism of H_2O adsorption on different surfaces is important in the field of the development of new catalysts. Since water is present in the atmosphere, it necessarily takes part in many reactions either as a reactant (for example in WGS reaction), byproduct or impurity [141]. Water adsorption on reduced and stoichiometric ceria has been thoroughly studied both experimentally and theoretically and has been a subject of many controversies. It is not clear whether water adsorbs as a molecule or dissociates on stoichiometric and reduced ceria surfaces as well as whether water adsorption on ceria surfaces causes its oxidation or reduction.

Different studies reported different behavior of ceria surfaces upon contact with water. In Ref. [142] ceria was described as strongly hydrophobic with many technological applications. In [26, 27, 28] oxidation of ceria films and powders upon water adsorption was reported, whereas further reduction of reduced ceria film on Pt(111) was shown in Ref. [24]. The possible explanation of this discrepancy was suggested in the fact that during the experiments different ceria surfaces were exposed to water. Namely for reduced (111) ceria surface it was shown that water causes its further reduction [143]. The same XPS and thermally programmed desorption (TPD) study also reported no dissociation occurring on reduced (111) ceria surfaces. On the other hand, dissociation of H_2O leading to stable OH groups up to 600 K on inverse model CeO_x/Au(111) was reported in [25]. XPS and TPD experiments on CeO_2(111)/Cu(111) [144] showed that lower temperature favored molecular water adsorption, while dissociation increased with higher temperature or with increased Ce^{3+}/Ce^{4+} ratio (degree of ceria reduction). The morphology of both stoichiometric and reduced ceria lay-

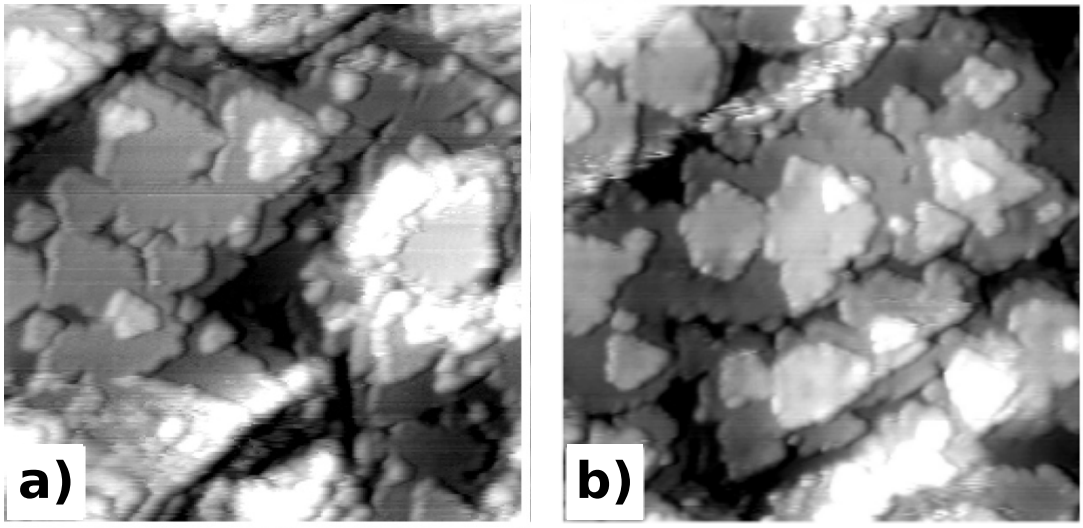

Figure 5.1: STM images of 10 ML ceria layer on Cu(111) before (a) and after (b) water adsorption and desorption. No significant change of morphology was observed upon water adsorption. Figure from Ref. Matolín et al. Catal. Today 181, 124-132, 2012.

ers was not affected by water adsorption as visible in Fig. 5.1. Another XPS and thermal desorption spectroscopy (TDS) studies [145, 146] on CeO_2 films on Cu(111) instead consistently reported both dissociation and molecular adsorption on stoichiometric surface but only dissociation on reduced surface.

In Ref. [147] a dynamic scanning force microscopy was employed to study water adsorption on clean stoichiometric CeO_2(111) surface. In this study, the water adsorbed on the surface was identified as triangular protrusions centered on Ce ions similar to image displayed in Fig. 5.2. The water adsorption was shown as spontaneous as well as tip-induced. The adsorbed water was identified as either molecular or dissociated molecule with proton (H) in immediate vicinity of the OH group so as to preserve local charge neutrality. The surface diffusion barier of 1 eV of a water molecule on ceria surface was estimated as a lower limit for the adsorption energy. Further study in Ref. [148] analyzed water adsorption on reduced ceria surface. Apart from molecular water, hydroxide groups localized at surface oxygen positions were also observed. Oxygen vacancy was proposed to act as a center for water dissociation on reduced ceria surface. Moreover in Ref. [149] the non-contact atomic force microscopy (NC-AFM) experiment displayed the water molecule on CeO_2(111) surface and reported the possibility of transferring water molecules by the tip across the clean surface or oxygen vacancy. According to this study, the water molecule was more likely to bind close to the vacancy than be dissociated in the vacancy.

Water adsorption on ceria surfaces have been subject of many theoretical studies as well. The results of different studies were rather inconsistent in terms of adsorption energies and structures. The latest reports [22, 23] give an overview of the previous studies as well as give possible explanations for the discrepancies namely the level of theory used (DFT or DFT+U), the size of the supercell and water coverage as well as difficulty to obtain lowest energy adsorption state. The

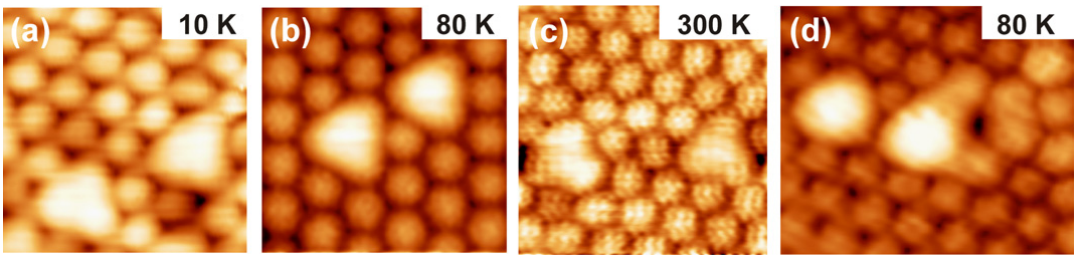

Figure 5.2: Water molecules adsorbed on stochiometric (a-c) and defective (d) ceria surfaces imaged by NC-AFM. Water is identified by triangular features centered above Ce ions. Figure from Torbrügge S. et al. J. Phys.: Condens. Matter 24, 044024, 2012.

overall findings are also summarized in table 5.2.

Kumar and Shelling in Ref. [141] calculated water adsorption on ceria surfaces using the standard DFT. They reported the preference for water adsorption on top of Ce atom forming a single hydrogen bond with surface oxygen upon adsorption on stoichiometric ceria surface. DFT+U [150] and DFT [151] analyses instead calculated preferred adsorption configuration of water molecule on clean ceria surfaces to form two hydrogen bonds with surface oxygen atoms. Watkins et al [152] performed DFT+U calculations with results showing water dissociation with OH group adsorbed on cerium ion and H atom on one of the three closely neighbouring surface oxygen atoms, which was more stable compared to water molecularly adsorbed on top of Ce ion with two hydrogen bonds with surface oxygen atoms. All the previous studies reported stronger adsorption of water molecule on reduced ceria surface as well as the preference for water dissociation in the presence of oxygen vacancies. [151, 141, 152]

Following study performed by Yang et al in [153] by DFT+U method reported both molecularly adsorbed and partially dissociated water molecule on stoichiometric ceria surface to be very close in energy with slight preference for the molecular adsorption. Also on reduced ceria surface both molecularly adsorbed H_2O together with completely dissociated OH groups were described in agreement with experimental reports. The same findings for stoichiometric ceria surface were reported in Ref. [22] together with thorough discussion of the discrepancies of previous studies. The closeness of the molecular adsorption and partially dissociated molecule was explained by the convenient lattice parameter and high flexibility of ceria upon water adsorption, while complete dissociation on stoichiometric surface was ruled out completely. The barrier of H_2O dissociation on ceria surface was calculated as well as the barrier for the rotation of the water molecule between the three equivalent positions on top of one cerium atom which is responsible for the water molecule appearing as a triangular feature in the scanning force microscopy images [148, 154]. Consistent results were reported also in newer studies [155, 156].

These studies clearly show the importance of defects for water adsorption. In these studies, the defect is always in form of oxygen vacancy, which is a structural defect of the lattice accompanied by electronic defect in form of Ce^{3+} ions in the

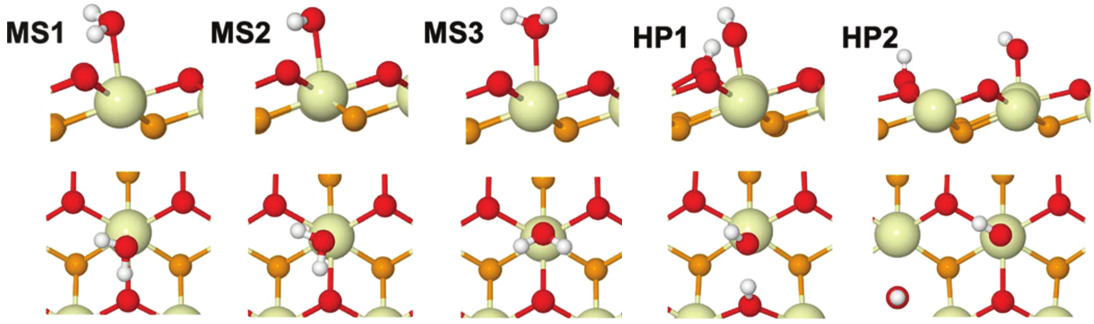

Figure 5.3: Metastable adsorption configurations of molecular and dissociated H_2O on clean ceria surfaces as described in [22]. Adapted with permission from Fernandéz-Torre et al. J. Phys. Chem. C 116, 13584-13596, 2012. Copyright 2013 American Chemical Society.

vicinity of the vacancy. In this perspective the thin films described in the previous chapter are ideal candidates to study water adsorption and disentangle the role of the two different kinds of defects on the adsorption and dissociation of water molecule on ceria surfaces. The 1 ML CeO_2/Cu(111) indeed has a stoichiometry of ceria but consists exclusively from Ce^{3+} ions even without the presence of structural defects. In contrast the 2 ML CeO_2/Cu(111) has full stoichiometry and charge state of ceria (111) surface. Therefore in this study we calculate and compare adsorption properties of water molecule adsorbed on both these systems in order to find the role of Ce^{3+} ions in the adsorption.

5.2 Calculation details

Calculation of water adsorption on thin ceria films on Cu(111) substrates employed spin-polarized DFT+U calculations within GGA aproximation in PBE formulation using Vanderbilt ultrasoft plane-wave pseudopotentials. The energy cutoffs for plane-wave basis set and electron density representation remained set to 30 and 300 Ry as well as the Monkhorst-Pack k-point mesh, since our supercells remained basically the same.

In order to be able to set a baseline for our calculations and to be able to compare and relate our results with available theoretical and experimental studies, first we calculated properties of water adsorption on clean ceria (111) surface. To do that we prepared a hexagonal supercell consisting of 3 ML (2×2) ceria slab separated by 12 Å vacuum layer. For further analysis of water adsorption on thin ceria films on Cu(111) we used the orthorhombic supercells containing 4 atomic layers (3×3) Cu slab and 1 and 2 ML (2×2) ceria films with atomistic structures described in the previous chapter. The topmost layer of ceria and lowest layer of copper were separated by 11 Å of vacuum. A detailed insight into energetics and electronic structure of these ultrathin films on Cu(111) is reported in appendix.

Water molecule was placed on top of the ceria films in a number of starting configurations. As a starting point we considered the adsorption configurations reported as stable or metastable for clean ceria (111) surface. The configura-

tions are displayed in Fig. 5.3, which was taken from Ref. [22] as well as the nomenclature for the configurations. The configurations are namely MS1, which corresponds to water molecule tilted in a way that one hydrogen forms a bond with one surface oxygen; MS2, where the water molecule is tilted symmetrically, so that each hydrogen atom form a bond with surface oxygen atom and MS3 which has both hydrogen atoms pointing away from the surface. All of these configurations were put on different sites of the ceria surfaces, namely above the O^{III}, Ce^{II} and O^{I} sites as well as above the subsurface vacancy in the 1 ML $CeO_{1.75}$ film in different heights above the surface oxygen layer in the range 0.5-2.0 Å. Adsorption on different symmetry inequivalent Ce^{II} atoms as described in previous chapter was also compared.

Moreover also dissociated water molecule was introduced on top of the thin ceria films in the configuration HP1 with OH group adsorbed on Ce ion and H atom on neighbouring surface oxygen and in the configuration HP2 where the remaining hydrogen is adsorbed on surface oxygen far from the OH group.

All of these starting configurations were relaxed according to the Hellman-Feynman forces with bottom ceria monolayer in case of adsorption on clean ceria and two bottom copper layers in all other cases fixed in the bulk-like positions and all the other atoms were allowed to relax.

5.3 Results

Here I will describe the results of our calculations of water adsorbed in molecular and dissociated state on ceria surfaces. First I will show results for 3 ML CeO_2 to establish a base line for futher analysis of water adsorption and dissociation on ultrathin supported ceria films. The comparison of our results for clean ceria slab with results reported in literature is shown in table 5.1 to verify validity of our calculations.

Table 5.1: H_2O adsorption energies $E^{ads}_{H_2O}$ [eV] on clean stoichiometric ceria surface. The adsorption energies of water molecule on $CeO_2(111)$ surface in different configurations described in Ref. [22] as calculated in this work. For comparison we show values calculated in different theoretical publications as well as the experimental value of adsorption energy.

Configuration	MS1	MS2	MS3	HP1	HP2
This work	-0.52	-0.51	-0.32	-0.50	-0.24
Férnandez-Torre et al. [22]	-0.54	-0.51	-0.32	-0.52	-0.24
Kumar and Shelling [141]	-0.58				
Chen et al. [150]	-0.49	-0.52			
Watkins et al. [152]			-0.36	-0.66	-0.16
Fronzi et al. [151]		-0.49	-0.33	-0.36	
Yang et al. [153]	-0.57			-0.55	
Experiment: Prin et al. [157]	-0.56 – -0.61				

Table 5.2: H_2O adsorption energies $E^{ads}_{H_2O}$ [eV] on ceria surfaces. Overview of the adsorption energies of water molecule on $CeO_2(111)$ surfaces in different configurations described in Ref. [22] calculated within this study on clean ceria slab and thin ceria films on Cu(111).

Configuration	MS1	MS2	MS3	HP1	HP2
3 ML CeO_2	-0.52	-0.51	-0.32	-0.50	-0.24
2 ML CeO_2/Cu(111)	-0.99	-0.95	-0.77	-0.97	-0.50
1 ML CeO_2/Cu(111)(S)	-0.71	-0.70	–	-0.21	-0.60
1 ML CeO_2/Cu(111)(R)	-0.56	-0.40	-0.32	–	-0.23
1 ML CeO_{2-x}/Cu(111)	-0.52	-0.45	-0.29	-0.31	-0.30

Next I will investigate the results of water adsorption on 2 ML CeO_2/Cu(111), which is a system exposing a ceria(111) surface with atomistic and electronic structure similar to that of clean unsupported ceria slab. The comparison with adsorption on clean ceria slab will show the effect of the Cu support and the copper-ceria interface 2 ML below the surface on the adsorption properties of water molecule.

Then I will show the properties of water molecule adsorbed on 1 ML ceria film exhibiting atomistic structure of clean ceria but electronic structure of reduced cerium oxide containing exclusively Ce^{3+} ions. This will allow to explore the differences arising from the presence of Ce^{3+} ions in the topmost monolayer of ceria film on the adsorption of water molecule.

Last I will show the properties of dissociative adsorption of water molecule on thin ceria films. An overview of adsorption energies for water molecule in different adsorption configurations in molecular and dissociated states is summarized in the table 5.2.

5.3.1 3 ML CeO_2

To be able to relate our findings to the available results in the literature, we study the adsorption of water molecule also on (111) surface of clean ceria slab. In particular we stabilize the reported MS1, MS2 and MS3 molecular adsorptions structures as well as the dissociated HP1 and HP2. In agreement with the latest literature results reported by Férnandez-Torre et al. [22], the one hydrogen bond MS1 structure is most stable and almost degenerate with dissociated HP1 and two hydrogen bond MS2 structures.

The bondlengths calculated in this study are reported in tables 5.3 and 5.4. The calculated structures and bondlengths are in good agreement with values reported in literature. The water molecule in MS1 configuration has one short (0.98 Å) and one long (1.01 Å) OH bond. The bond between hydrogen and surface oxygen is longer than reported value (1.77 Å compared to reported 1.69 Å) which might be responsible for slightly lower obtained adsorption energy. The bond between oxygen atom in water molecule and cerium atom in ceria is 2.63 Å which is 10% larger than the Ce-O bond in ceria bulk. Similar Ce-O bondlength (2.62 Å) was calculated also for the MS2 configuration. The water molecule in

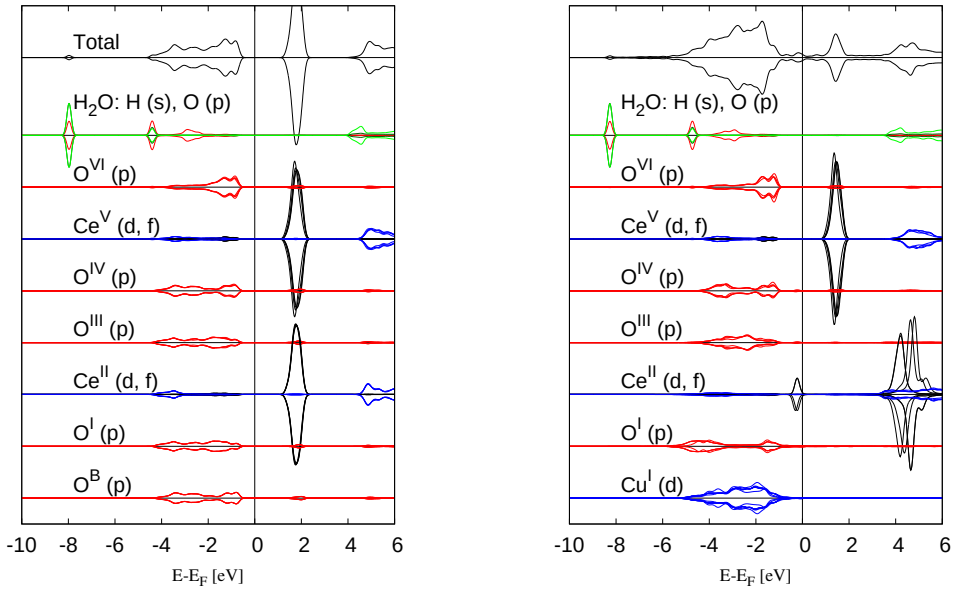

Figure 5.4: Projected density of state of individual atoms upon adsorption of water molecule in the MS1 configuration on 3 ML CeO_2 slab (left) and 2 ML CeO_2/Cu(111) (right). The green lines correspond to H s orbitals, red lines are O p orbitals, blue and black represent Ce d and f states respectively.

the MS2 configuration has two symmetrical 0.99 Å OH bonds and the hydrogens are bound to the surface oxygen atoms with the bondlengths of 2.04 and 2.07 Å. The distance of the oxygen atom in water molecule to the Ce atom in the surface in case of the MS3 configuration with both hydrogen atoms pointing away from the surface is larger by 0.1 Å (2.71 Å).

The bonding of water molecule on the clean ceria slab in the most stable MS1 configuration is analyzed with respect to the electronic properties. The pDOS analysis is displayed in the Fig. 5.4, while the bonding charge in the Fig. 5.5. It is clearly visible that water molecule forms a bond between oxygen atom and surface Ce ion as well as bond between H atom and surface oxygen. The O-Ce^{II} bond is mostly covalent which is visible from the overlap of oxygen p states with Ce d states. The H-O^{I} bond has also ionic components due to the sharp localized peak of H s states and a charge accumulation around the oxygen atom in the water molecule and between the water molecule and ceria surface as shown in the curve displaying the bonding charge integrated in the planes perpendicular to the z direction in Fig. 5.9. By comparing the Löwdin charges of the atoms in the first and second ceria monolayer before and after H_2O adsorption (displayed in Tab. 5.8) we can observe slight increase of charge in the case of surface monolayer mostly in O^{VI} p, Ce^{V} d and little less at O^{IV} p states. The charge of the subsurface monolayer doesn't change. The oxygen atom in water molecule exhibits decrease in the total charge compared to isolated H_2O molecule as shown in Tab. 5.7.

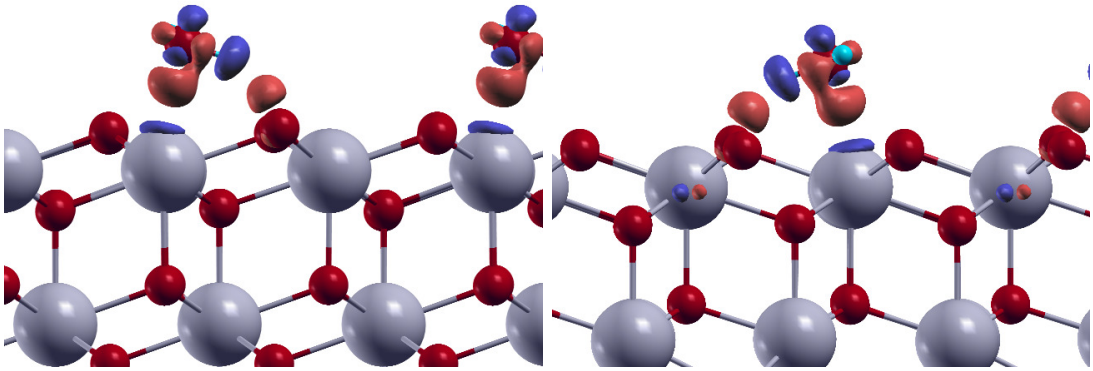

Figure 5.5: Bonding charge calculated for adsorption of water molecule in MS1 configuration on 3 ML CeO_2 (left) and 2 ML CeO_2/Cu(111) (right). The red areas correspond to charge accumulation, blue represents charge depletion.

The H_2O dissociation is studied by exploring the adsorption configurations HP1 and HP2 with water molecule dissociated to OH group and H atom with H close to the OH group (HP1) and further from the OH group (HP2). The adsorption energies as well as the bondlengths for both configurations on clean ceria slab correspond well with the values reported in literature (see table 5.4).

In the more stable HP1 configuration, the OH group is bound with the oxygen end to the Ce^V ion with bondlength 2.24 Å and H is adsorbed at surface oxygen directly neighbouring the Ce atom with bondlength 1.01 Å. The Ce-O bond is significantly shorter than the bond in the case of molecularly adsorbed water. The distance between the oxygen in the OH group and the remaining hydrogen atom is 1.64 Å. From the bonding analysis in Fig. 5.6 we see the O^{VI}-H bond from the overlap of the hydrogen s states with the sharp peaks of one of the surface oxygen p states. The p states of the oxygen atom in the OH group is shifted to higher energies compared to the oxygen p states in molecularly adsorbed water due to the interaction with the Ce ion. On the other hand there is also overlap between the oxygen p states with both hydrogen atoms showing partial bond also between O in the OH group and H adsorbed in the neighbourhood.

The adsorption in the HP2 configuration exhibits significant differences with respect to the adsorption in HP1 configuration. Both the H-O^{VI} and O-Ce^V bonds are shorter. In particular, he H-O^{VI} bond is 0.98 Å long, similar to the length of the bond in water molecule or in OH group. The O-Ce bond decreases to 2.16 Å. From the pDOS analysis it is evident, that the oxygen p states from the OH group shifted to even higher energies and now exhibit overlap only with the hydrogen in the OH group. There is no more bond with the separately adsorbed hydrogen, which instead overlaps with sharper peak of oxygen in the surface ceria atomic layer.

In conclusion results of our simulation of H_2O adsorption on clean stoichiometric CeO_2 (111) slab are in line with the results reported in literature and

Table 5.3: H_2O adsorption energies $E^{ads}_{H_2O}$ [eV] of water molecule adsorbed on ceria surfaces; lengths of bonds between water molecule and ceria surface (H-O; O-Ce) and O-H in the water molecule for each system. Data reported also for adsorption on symmetrically inequivalent sites on 1 ML $CeO_{1.75}$/Cu(111) substrate as described in previous chapter. Corresponding values from the literature also shown for comparison.

ads site	substrate	E_{ads} [eV]	H-O_{surf} [Å]	O-Ce [Å]	H-O [Å]
MS1	[22]	-0.54	1.69	2.62	0.97 - 1.01
	3 ML CeO_2	-0.52	1.77	2.63	0.98 - 1.01
	2 ML CeO_2	-0.99	1.71	2.61	0.98 - 1.01
	1 ML CeO_2(S)	-0.71	1.67	2.68	0.97 - 1.02
	1 ML CeO_2(R)	-0.56	1.66	2.69	0.97 - 1.02
Ce_B-O_B	1 ML CeO_{2-x}	-0.52	1.70	2.70	0.97 - 1.01
Ce_B-O_T	1 ML CeO_{2-x}	-0.51	1.72	2.71	0.97 - 1.01
Ce_T-O_B	1 ML CeO_{2-x}	-0.48	1.68	2.69	0.97 - 1.01
MS2	[22]	-0.51	–	–	–
	3 ML CeO_2	-0.51	2.04; 2.07	2.62	0.99 - 0.99
	2 ML CeO_2	-0.95	2.01; 2.02	2.62	0.99 - 0.99
	1 ML CeO_2(S)	-0.70	2.03; 2.06	2.68	0.99 - 0.99
	1 ML CeO_2(R)	-0.40	2.23; 2.28	2.68	0.98 - 0.98
Ce_T-O_B	1 ML CeO_{2-x}	-0.45	2.04; 2.05	2.66	0.99 - 0.99
MS3	[22]	-0.32	–	–	–
	3 ML CeO_2	-0.32	2.94; 2.95	2.71	0.98 - 0.98
	2 ML CeO_2	-0.77	2.93; 2.93	2.70	0.98 - 0.98
	1 ML CeO_2(S)	–	–	–	–
	1 ML CeO_2(R)	-0.32	3.07; 3.07	2.74	0.98 - 0.98
Ce_T-O_B	1 ML CeO_{2-x}	-0.29	3.01; 3.02	2.74	0.99 - 0.99

can therefore be considered a sound reference point for establishing the effect of the different charge state and thickness of ceria films on H_2O adsorption and dissociation.

5.3.2 2 ML CeO_2/Cu(111)

The 2 ML CeO_2/Cu(111) is a structure which expose an outermost CeO_2(111) monolayer with stoichiometry and electronic structure very similar to clean ceria (111) slab. Important differences arise only when the subsurface ceria monolayer is taken into consideration, since it is formed by Ce^{3+} ions and thus has a different charge state than the corresponding monolayer under the surface in the ideal ceria slab. Note that these Ce^{3+} ions are 4 Å below the surface and 5.5 Å from the water molecule. Still they do have an important effect on the surface properties. The bonding of water molecule on this surface was expected to be very similar to the bonding on clean ceria slab, instead we found, that H_2O adsorption on 2 ML CeO_2/Cu(111) is more stable. The adsorption energy of water molecule in MS1 configuration is -0.99 eV, which is 0.47 eV higher than for the clean ceria surface.

Table 5.4: H_2O adsorption energies $E^{ads}_{H_2O}$ [eV] of water molecule adsorbed on ceria surfaces in dissociated state; lengths of bonds between the OH and H groups and ceria surface (H-O; O-Ce) and O-H in the OH group as well as between OH group and H atom. Corresponding values from the literature also shown for comparison.

ads site	substrate	E_{ads} [eV]	H-O_{surf} [Å]	O-Ce [Å]	H-O [Å]
HP1	[22]	-0.52	1.01	2.23	0.97 - 1.64
	3 ML CeO_2	-0.50	1.01 (2.66)	2.24	0.97 - 1.64
	2 ML CeO_2	-0.97	1.01 (2.65)	2.24	0.97 - 1.64
	1 ML CeO_2(S)	-0.21	1.04 (3.23)	2.33	0.97 - 1.52
	1 ML CeO_2(R)	–	–	–	–
Ce_B	1 ML CeO_{2-x}	-0.31	1.05 (3.27)	2.34	0.97 - 1.52
HP2	[22]	-0.24	–	–	–
	3 ML CeO_2	-0.24	0.98 (2.25)	2.16	0.98 - 4.36
	2 ML CeO_2	-0.50	0.97 (2.40)	2.16	0.98 - 4.39
	1 ML CeO_2(S)	-0.60	0.98 (4.24)	2.17	0.97 - 4.67
	1 ML CeO_2(R)	-0.23	0.98 (4.31)	2.18	0.97 - 4.59
Ce_B	1 ML CeO_{2-x}	-0.30	0.98 (4.40)	2.17	0.97 - 4.50

The same holds also for other studied adsorption configurations, namely MS2 and MS3 have adsorption energies -0.95 and -0.77 eV (0.45 eV more stable than MS2 and MS3 on clean ceria). The higher stability on 2 ML ceria film on Cu(111) than on thick ceria slab is thus consistent regardless of the adsorption configuration. The reason for this behaviour is expected to arise from the electrostatics effects due to the different charge state of subsurface ceria monolayer.

The adsorption properties of water molecule on 2 ML ceria film are calculated and from the results it is clear, that the structure of all the configurations remains basically the same as the structures on clean ceria surface. Overall trend is the decrease of O-Ce^{II} bond by 0.01-0.02 Å and H-O^{I} bond by 0.06, 0.05 and 0.02 Å in the MS1, MS2 and MS3 structures respectively. On the other hand the shape of the bonding charge in Fig. 5.5 or the peaks in the pDOS figure in Fig. 5.4 show that the mode of adsorption remains the same as for water molecule on clean ceria. Also the charge of the atoms in water molecule remains almost unchanged (see table 5.7). The atoms in the surface ceria monolayer exhibit also increase in charge of O p and Ce d states as in the case of adsorption on clean ceria, the increase in the case of Ce d states is slightly higher (see table 5.5).

Different behaviour between the adsorption on clean ceria slab and 2 ML film can be observed when we take into account the subsurface ceria monolayer. The charges of the atoms in subsurface monolayer are different already before the adsorption due to the presence of the metal-oxide interface underneath the 2 ML film. The main difference is in the Ce atomic layer which contains Ce^{3+} ions in the case of 2 ML film, and Ce^{4+} ions in the clean ceria slab. Another difference is also exhibited by oxygen atoms in the interfacial atomic layer, which are more charged by 0.3 on average. The oxygen atoms in the third atomic layer from the interface are also more charged but with much smaller difference. After the adsorption of water molecule, the charge at the subsurface monolayer of clean

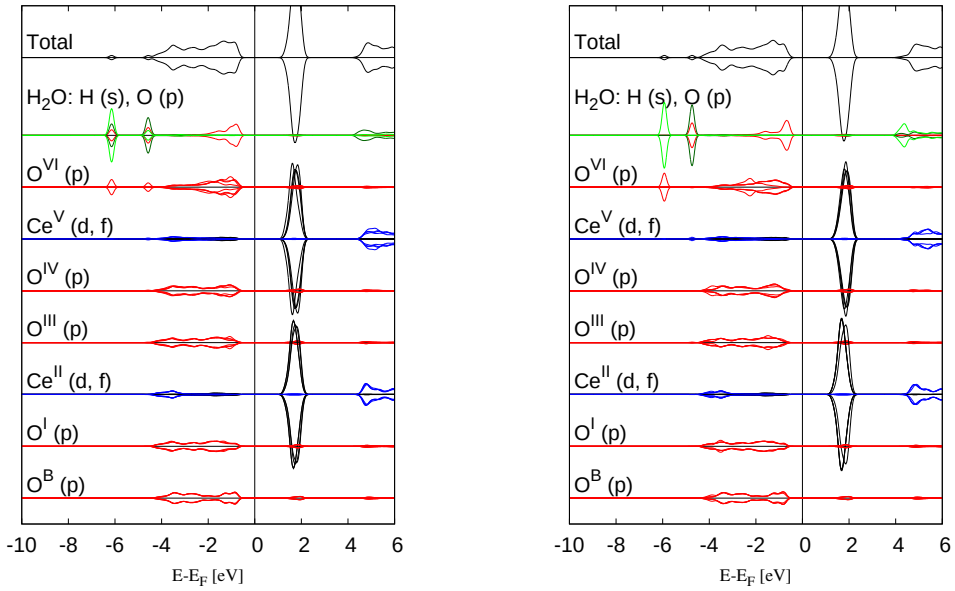

Figure 5.6: Projected density of state of individual atoms in the water molecule adsorbed in dissociated state in the HP1 (left) and HP2 (right) configuration on 3 ML CeO_2. The green lines correspond to H s orbitals, red lines are O p orbitals, blue and black represent Ce d and f states respectively.

ceria slab doesn't change significantly. On the other hand important changes can be observed in the case of the subsurface monolayer in 2 ML ceria film. In particular the Ce states charge lowers upon water adsorption, while the charge of the interfacial oxygen atoms increase as shown in table 5.6. Also the Löwdin charge of the copper atoms in the first layer of substrate changes, in average it increases by 0.01 upon H_2O adsorption. These results evidence the interface charge transfer induced by the adsorbate and support the finding that metallic support can have a role in adsorption of molecules on the supported oxide films by providing extra charge to better accommodate the molecule.

In summary we show the preferential adsorption of water molecule on 2 ML CeO_2/Cu(111) compared to adsorption on clean stoichiometric ceria slab as a result of the presence of charge reservoir at the metallic interface 6.7 Å underneath the surface of the 2 ML ceria film.

5.3.3 1 ML ceria/Cu(111)

Adsorption of water molecule in the same configuration (MS1) as in previous systems of clean ceria slab and 2 ML ceria film to the distance 3.2 Å above the surface of 1 ML CeO_2/Cu(111) leads to a very unexpected result. During the relaxation the water molecule is attracted towards the surface as expected, but also simultaneously the whole ceria monolayer reorganizes so that its structure deviates from the structure of symmetrical stoichiometric 1 ML ceria film. In order to find out whether the reorganization of the monolayer is induced by the

Table 5.5: **Löwdin charges of atoms in surface O-Ce-O monolayer of ceria in the 3 ML CeO_2 and 2 ML CeO_2/Cu(111) cases before and after adsorption of water molecule in MS1 configuration.** Only orbitals with significant changes are shown.

	O^{VI}		Ce^{V}		O^{IV}	
	t	p	t	d	t	p
BEFORE ADSORPTION						
3 ML CeO_2	6.58	4.83	10.82	1.86	6.51	4.80
	6.58	4.83	10.82	1.86	6.51	4.80
	6.58	4.83	10.82	1.86	6.51	4.80
	6.58	4.83	10.82	1.86	6.51	4.80
2 ML CeO_2/	6.59	4.83	10.81	1.84	6.52	4.81
Cu(111)	6.58	4.83	10.81	1.85	6.52	4.81
	6.58	4.83	10.81	1.85	6.52	4.81
	6.58	4.83	10.81	1.85	6.52	4.81
AFTER ADSORPTION						
3 ML CeO_2	6.62	4.86	10.83	1.87	6.52	4.81
	6.56	4.81	10.83	1.88	6.51	4.80
	6.59	4.84	10.82	1.87	6.51	4.80
	6.59	4.84	10.83	1.87	6.52	4.81
2 ML CeO_2/	6.60	4.84	10.83	1.87	6.53	4.82
Cu(111)	6.56	4.81	10.83	1.86	6.51	4.81
	6.59	4.84	10.83	1.88	6.52	4.81
	6.62	4.86	10.83	1.87	6.53	4.82

water molecule or is a stable state of the monolayer, we proceed in the analysis by removing the water molecule and allowing further relaxation of the reorganized film. The relaxation revealed that it is indeed a stable solution and will be referred to as "1 ML CeO_2/Cu(111)(R)" to differentiate it from the original symmetrical 1 ML ceria film reported in previous section ("1 ML CeO_2/Cu(111)(S)").

The top view of the structure of the reconstructed (R) ceria film is shown in Fig. 5.7 (a), where it is possible to compare the displacement of individual atoms with the original symmetrical 1 ML case (S) in the subfigure (b). Due to the distortion of atomic positions two of the interface O^I atoms move to a hollow-like positions with two Cu^I-O^I bondlengths 2.12 Å and one 2.04 Å, while the other two O^I atoms are in a distorted bridge-top positions between two Cu^I atoms with one short Cu^I-O^I bond 1.95 (1.96) Å and one long 2.20 (2.33) Å for the two O^I atoms respectively. Also other atomic layers of ceria monolayer become distorted resulting in four nonequivalent atoms in each atomic layer. Overall the rigid translation together with local distortions of the ceria slab decreases the total energy of the system by 0.3 eV. This energy difference is related to the

Table 5.6: **Löwdin charges of atoms in subsurface O-Ce-O monolayer of ceria in the 3 ML CeO_2 and 2 ML CeO_2/Cu(111) cases before and after adsorption of water molecule in MS1 configuration.** Only orbitals with significant changes are shown.

	O^{III}	Ce^{II}				O^{I}
	t	t	d	f+	f-	t
BEFORE ADSORPTION						
3 ML CeO_2	6.53	10.89	1.94	0.36	0.36	6.53
	6.53	10.89	1.94	0.36	0.36	6.53
	6.53	10.89	1.94	0.36	0.36	6.53
	6.53	10.89	1.94	0.36	0.36	6.53
2 ML CeO_2/	6.59	11.10	1.80	0.94	0.09	6.76
Cu(111)	6.58	11.08	1.70	0.07	1.05	6.85
	6.58	11.10	1.80	0.10	0.94	6.85
	6.58	11.10	1.80	0.94	0.09	6.85
AFTER ADSORPTION						
3 ML CeO_2	6.53	10.89	1.94	0.35	0.35	6.53
	6.53	10.89	1.94	0.35	0.35	6.53
	6.53	10.89	1.94	0.36	0.36	6.53
	6.53	10.89	1.94	0.35	0.35	6.53
2 ML CeO_2/	6.59	11.06	1.70	0.07	1.03	6.78
Cu(111)	6.58	11.05	1.67	1.06	0.07	6.88
	6.58	11.07	1.70	0.07	1.03	6.88
	6.58	11.07	1.70	1.03	0.07	6.88

(2×2) CeO_2(111)/(3×3) Cu(111) supercell interface, corresponding to an area of over 53 Å^2 involving contributions from four molecules of ceria and at least nine interfacial atoms of Cu and eight Cu-O^I bonds (resulting in contribution of 0.03 eV per bond). Compared to the binding energy of copper atom on ceria surfaces which is in order of eV (see chapter 3), we consider the energy difference per Cu-O bond 0.03 eV in this interface as insignificant. Although the change of the structure can have some influence on the properties of the monolayer, the change doesn't significantly affect the structure of the topmost oxygen layer exposed to the adsorbates as well as the peculiar electronic structure of the monolayer in terms of the charge state of cerium ions which remain Ce^{3+}, therefore we don't expect significant differences in the adsorption mechanism and energetics.

In order to further explore the properties of the structural distortion of the film, we study its effect on the adsorption of water molecule. Therefore we consider in the analysis both configurations of the ultrathin 1 ML ceria film on copper, namely the original denoted as (S) and the reconstructed denoted as (R). Also in this case we explored the adsorption of water molecule in MS1, MS2 and MS3 configurations.

The adsorption energies of water molecule adsorbed on both forms of 1 ML

Table 5.7: **Lowdin charges of H-O-H on different substrates**

	H	H	O		
	t	t	t	s	p
H_2O (g)	0.63	0.63	6.65	1.66	4.99
3 ML CeO_2	0.64	0.63	6.58	1.64	4.94
2 ML CeO_2/Cu(111)	0.64	0.63	6.58	1.65	4.94
1 ML CeO_2/Cu(111)	0.65	0.63	6.61	1.65	4.96
1 ML $CeO_{1.75}$/Cu(111)	0.65	0.63	6.61	1.65	4.97

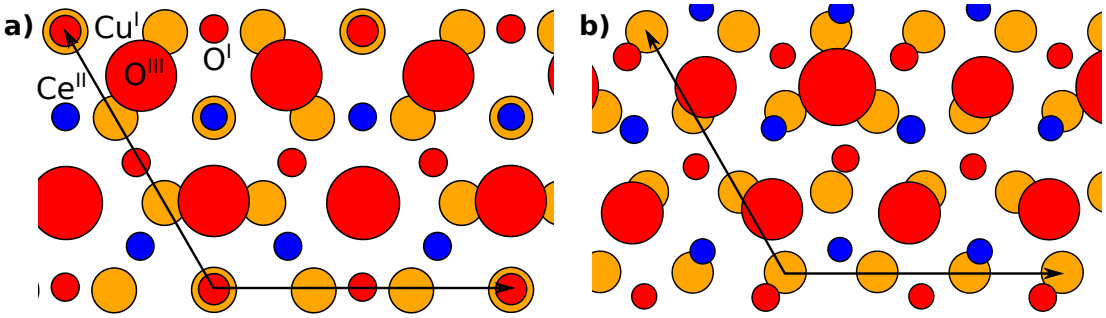

Figure 5.7: A top view of 1 ML CeO_2/Cu(111) system in different metastable atomistic configurations. An original symmetrical structure 1 ML CeO_2/Cu(111)(S) (a) is shown for comparison with the reconstructed structure with reorganized atoms in ceria monolayer 1 ML CeO_2/Cu(111)(R) (b).

ceria film (S) and (R) in all adsorption configurations are reported in table 5.3. The order of stability of the different H_2O adsorption configurations followed the same tendency as in the case of clean ceria surface, the MS1 configuration is most stable closely followed by MS2, while MS3 with hydrogen atoms not bound to the surface is the least stable configuration. Further comparison show, that H_2O adsorption on the 1 ML CeO_2/Cu(111) films is less stable than on 2 ML films and more stable or comparable to adsorption on clean ceria slab. Namely adsorption on the original monolayer (S) is more stable with adsorption energy -0.71 eV for the MS1 configuration and -0.70 eV for MS2 configuration, while the adsorption on the reconstructed monolayer (R) is less stable with adsorption energy -0.56, -0.40 and -0.32 eV for MS1, MS2 and MS3 configurations respectively. Moreover in the case of the reconstructed (R) film the adsorption energy on different structurally inequivalent Ce ions varies between -0.48 – -0.56 eV for the MS1 configuration due to the different local structures at the interface felt by the Ce ions as a result of the structural atomic distortions of atoms at the interface. Thus we can conclude that the local structure at the interface has an effect on the adsorption energies of water molecules adsorbed on ultrathin ceria films.

For further analysis of structure and electronic properties of H_2O adsorption we chose the more stable case of MS1 on 1 ML Ce_2/Cu(111)(S). The H_2O adsorption on this surface results in decrease of the H-O^{III} bond compared to corresponding H-O^{VI} bond in the case of adsorption on 2 ML ceria film by 0.04 Å and increase of the O-Ce^{II} bond by 0.07 Å. This is an effect of electrostatics,

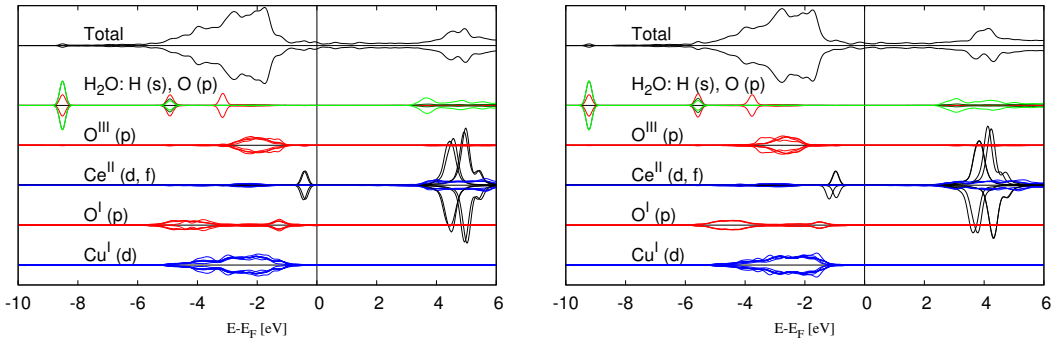

Figure 5.8: Projected density of state of individual atoms upon H_2O adsorption in the MS1 configuration on 1 ML CeO_2/Cu(111)(S) (left) and 1 ML $CeO_{1.75}$/Cu(111) (right). The green lines correspond to H s orbitals, red lines are O p orbitals, blue and black represent Ce d and f states respectively.

since negatively charged oxygen ion is less attracted by Ce^{3+} ion than by Ce^{4+}. Instead the oxygen atom in water molecule exhibits increase in Löwdin charge compared to water molecule on 2 ML film. The charge on surface oxygen atoms larger for 1 ML ceria due to the effect of the copper/ceria interface cause the decrease of the H-O bond. The pDOS analysis in Fig. 5.8 show increased ionic bonding between water molecule and cerium atom since there is almost no overlap of oxygen and cerium states and the O p states in water molecule exhibit sharper narrower peak compared to the pDOS for adsorption on 2 ML film. Increase of the Löwdin charge value upon H_2O adsorption was observed for the Ce^{II} ions and even more for subsurface oxygen layer. Slight change was shown also for first layer of copper atoms, whose charge increased in average for 0.01 per atom.

The last case of 1 ML ceria film is the one observed experimentally containing subsurface vacancies. For this system we also explored different inequivalent Ce^{II} and O^{III} atoms (as described in chapter 4) as adsorption sites for the water molecule. In general we observe adsorption energies lower than in the case of 1 or 2 ML ceria films and comparable to the adsorption on clean ceria slab. In particular, the adsorption was 0.44, 0.5 and 0.48 less stable than on 2 ML film for the MS1, MS2 and MS3 configuration respectively. The order of stability of individual configurations is kept also in the case of the film with subsurface vacancy.

An interesting result is observed H_2O adsorption on different inequivalent Ce sites. The adsorption is more stable when oxygen atom in water molecule is bound to the Ce_B^{II} atom compared to adsorption above Ce_T^{II}. The explanation might be in the different coordination of these two atoms where the Ce_T^{II} atom is 6-fold coordinated, while the Ce_B^{II} only 5-fold which makes it more disposed to make a bond with water molecule.

The electronic properties of water molecule bound on 1 ML $CeO_{1.75}$/Cu(111) in MS1 configuration are analyzed. From pDOS figure 5.8 and bonding charge figure 5.10 it is clear that the bonding mechanism of water molecule on this film is the same as in the case of 1 ML CeO_2/Cu(111)(S). The pDOS doesn't exhibit any difference in terms of sharpness or location of the particular peaks except for

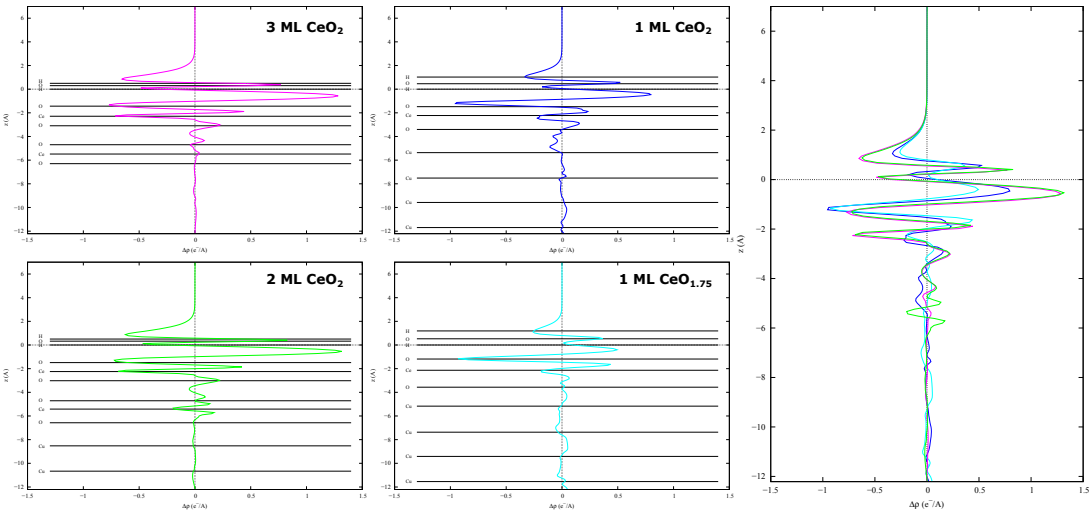

Figure 5.9: Bonding charge integrated across the planes perpendicular to the z direction (right) for all studied systems with H_2O adsorbed in MS1 configuration individually in corresponding panels and for comparison plotted together in the right panel.

the shift of the peaks with respect to the Fermi energy observed already for 1 ML $CeO_{1.75}$/Cu(111) without adsorbates described in previous chapter.

The Löwdin charge of the atoms in the whole defective monolayer, although different from the charge of the stoichiometric monolayer (specifically the surface oxygen and cerium atoms more charged, the interface oxygen less charged), does not significantly change upon H_2O adsorption. The bondlengths show similar trend as for bonding on 1 ML film without vacancy.

In summary we can say that the bonding of water molecule on 1 ML ceria films is less stable than on 2 ML film but more stable than on clean ceria slab. The mechanism of the bonding doesn't change significantly, except for the electrostatics effect which cause increase of Ce-O bond and decrease of O-H bond. The subsurface vacancy does not have an important effect on the H_2O adsorption, so we can conclude, that the electrostatic effect of Ce^{3+} ions is more important for the adsorption of water molecule on ceria surfaces than the presence of subsurface oxygen vacancy.

5.3.4 H_2O dissociation

In order to study H_2O dissociaton on ultrathin ceria films, we explore the structure of dissociated water molecule in HP1 and HP2 configurations on thin ceria films on Cu(111). The bonding of dissociated water molecule on 2 ML CeO_2/Cu(111) substrate exhibits exactly the same trends as molecular adsorption. Namely also in this case the dissociated water molecule binds preferentially on 2 ML film with adsorption energy of -0.97 eV, which is only 0.02 eV less stable than MS1 configuration and more stable than MS2 configuration. Consistently it is 0.47 eV more stable than adsorption on clean ceria slab. The same holds for the HP2 configuration which exhibited adsorption energy -0.50 eV, 0.26 eV more stable than on clean ceria. Both configuration exhibit agreement in bondlenghts

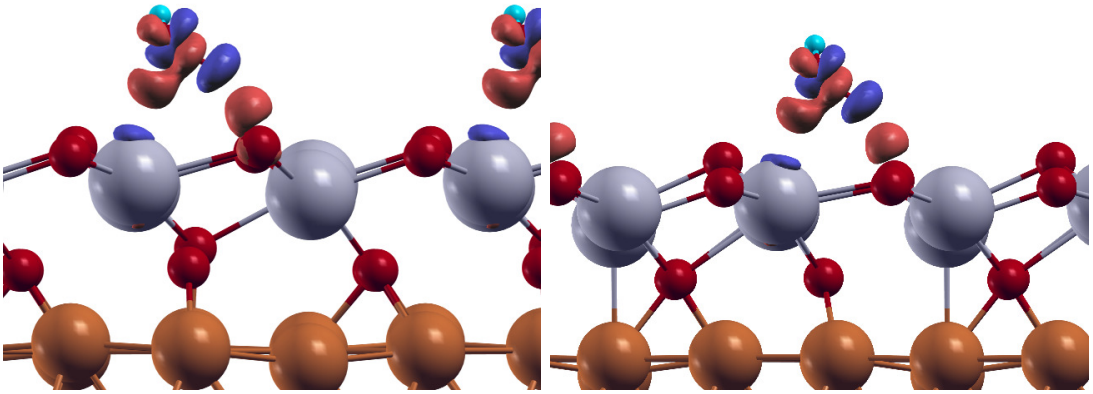

Figure 5.10: Bonding charge calculated for H_2O adsorption in MS1 configuration on 1 ML CeO_2/Cu(111)(S) (left) and 1 ML $CeO_{1.75}$/Cu(111) (right). The red areas correspond to charge accumulation, blue represents charge depletion.

with the dissociated water molecule on clean ceria as well as the same electronic properties shown in Fig. 5.11. In particular as in the case of clean ceria we observe shift of O p states to higher energy, overlap of O p states with both hydrogen atoms in case of HP1 configuration and with only one in case of HP2 configuration and formation of sharp oxygen p peak of one of the surface oxygens which overlaps with the hydrogen s state.

On the other hand adsorption of dissociated water molecule on 1 ML ceria films exhibits completely different characteristics from the adsorption on clean ceria slab or 2 ML film. As in the previous case, we put the OH and H adsorbates in the HP1 and HP2 configurations on the 1 ML films in different distances and relax the system. The relaxation of all HP1 starting configurations on 1 ML CeO_2/Cu(111)(R) results in recombination of OH and H into H_2O adsorbed in MS1 configuration. We were able to stabilize a HP1-like solution on 1 ML CeO_2/Cu(111)(S) substrate, but this solution compared to HP1 configuration on clean ceria slab or 2 ML film exhibits larger O-Ce^{II} bond (2.33 Å) and much shorter bond between the oxygen in the OH group and isolated H (1.52 Å, 0.12 Å shorter) showing the tendency to recombine together with much lower adsorption energy -0.21 eV compared to the MS1 adsorption energy -0.71 eV. Exactly the same behavior is observed also for the 1 ML $CeO_{1.75}$/Cu(111) substrate whose resulting structure also exhibits reduced H-O bond, increased O-Ce bond and the adsorption energy -0.31 eV compared to MS1 adsorption energy -0.52 eV.

When starting from the HP2 configuration, the adsorption characteristics exhibit even more different behaviour. While the H atom remains adsorbed on the surface O atom with bondlengths consistently 0.98 Å for all 1 ML substrates, the OH group causes significant elevation of the Ce atom beneath for more than 1 Å (1.3 Å in case of the (S) substrate). Resulting O-Ce^{II} bond remains only slightly (by 0.01 Å) larger than in HP2 configuration on 2 ML film. The adsorption energies exhibit large dispersion probably because of the different exact local

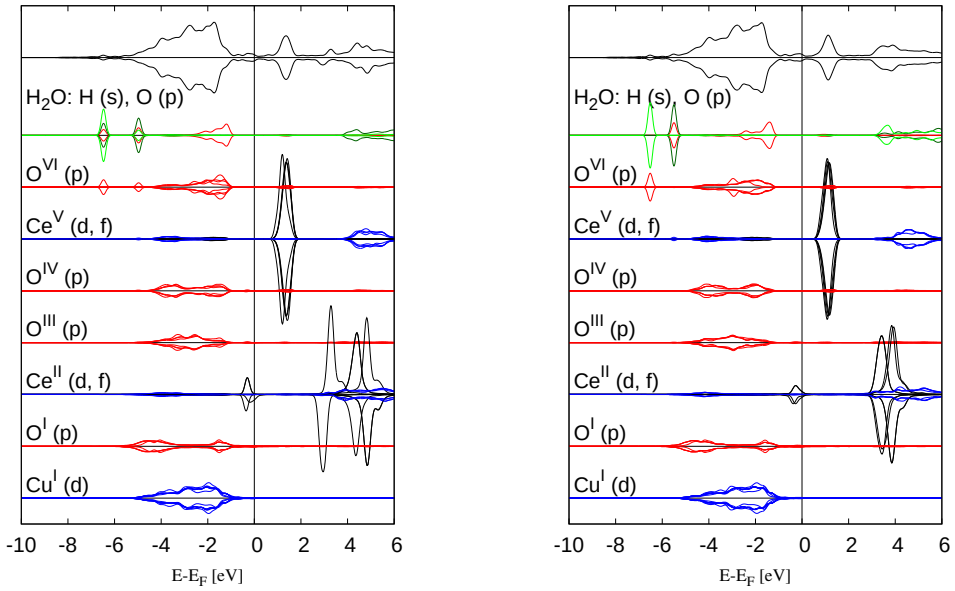

Figure 5.11: Projected density of state of individual atoms in the water molecule adsorbed in dissociated state in the HP1 (left) and HP2 (right) configuration on 2 ML CeO_2/Cu(111). The green lines correspond to H s orbitals, red lines are O p orbitals, blue and black represent Ce d and f states respectively.

structure of the resulting reorganized monolayer.

Thus in conclusion we can state that the thickness of the layer has a significant influence on the properties of water molecule adsorbed on thin ceria films in the dissociated state. In the case of completely dissociated molecule, the OH group tends to be repelled by the charged ceria film and cause significant distortion to the film. Moreover the charge state of the first ceria monolayer due to the presence of the metallic interface underneath induce strong preference for molecular adsorption on 1 ML ceria films compared to adsorption of predissociated water molecule.

5.4 Conclusions

In this chapter we studied the water adsorption in the molecular and dissociated form on ceria films of different thickness. We observed strong preferential adsorption on 2 ML CeO_2/Cu(111) system compared to adsorption on clean ceria slab. This strong preference was shown both for adsorption of water as a molecule as well as in dissociated state. The adsorption as a molecule or as OH-H pair in direct neighbourhood was almost degenerate. The mechanism of adsorption was identical to the adsorption on clean ceria slab

The water adsorption on ultrathin 1 ML ceria films exhibited completely different characteristics. The molecular adsorption on 1 ML films was less stable than on thicker 2 ML film but more stable than on clean ceria slab. Moreover the

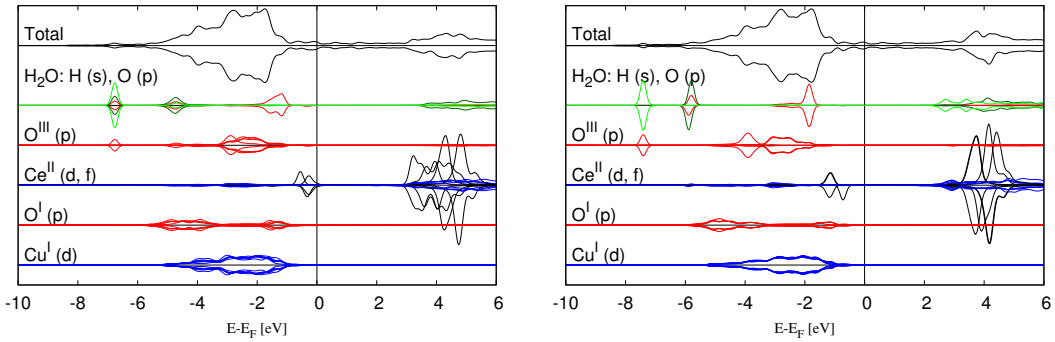

Figure 5.12: Projected density of state of individual atoms in the water molecule adsorbed in dissociated state in the HP1 (left) and HP2 (right) configuration on 1 ML CeO_2/Cu(111)(S). The green lines correspond to H s orbitals, red lines are O p orbitals, blue and black represent Ce d and f states respectively.

molecular adsorption was strongly preferred to adsorption of dissociated molecule in the HP1 configuration in contrast with the trends shown for 2 ML film and clean ceria slab. The charge state as well as the thickness of the film thus has an important role in the adsorption properties and characteristics of water bound on ceria surfaces.

Table 5.8: **Lowdin charges of atoms in the surface ceria monolayer of different supercells before and after adsorption of water molecule in MS1 configuration.**

	O^{III}/O^{VI}		Ce^{II}/Ce^{V}				O^{I}/O^{IV}	
	t	p	t	d	f+	f-	t	p
BEFORE ADSORPTION								
2 ML CeO_2/	6.59	4.83	10.81	1.84	0.38	0.36	6.52	4.81
Cu(111)	6.58	4.83	10.81	1.85	0.37	0.37	6.52	4.81
	6.58	4.83	10.81	1.85	0.37	0.37	6.52	4.81
	6.58	4.83	10.81	1.85	0.37	0.36	6.52	4.81
1 ML CeO_2/	6.66	4.91	10.94	1.59	0.06	1.04	6.79	4.99
Cu(111)	6.64	4.90	10.99	1.61	1.08	0.06	6.88	5.04
	6.64	4.90	10.95	1.59	0.06	1.06	6.87	5.04
	6.64	4.90	10.95	1.59	1.06	0.06	6.88	5.04
1 ML $CeO_{1.75}$/	6.61	4.87	11.04	1.69	1.02	0.07	6.85	5.03
Cu(111)	6.66	4.91	11.00	1.61	0.06	1.06	6.85	5.03
	6.66	4.91	11.03	1.67	1.05	0.06	6.84	5.03
	6.65	4.91	11.03	1.68	0.07	1.02		
AFTER ADSORPTION								
2 ML CeO_2/	6.60	4.84	10.83	1.87	0.36	0.36	6.53	4.82
Cu(111)	6.56	4.81	10.83	1.86	0.37	0.37	6.51	4.81
	6.59	4.84	10.83	1.88	0.36	0.37	6.52	4.81
	6.62	4.86	10.83	1.87	0.37	0.36	6.53	4.82
1 ML CeO_2/	6.65	4.91	10.96	1.58	0.06	1.08	6.81	5.01
Cu(111)	6.67	4.93	11.02	1.65	1.07	0.06	6.90	5.07
	6.64	4.91	10.96	1.58	0.06	1.08	6.90	5.06
	6.62	4.89	10.95	1.57	1.08	0.06	6.89	5.06
1 ML $CeO_{1.75}$/	6.60	4.87	11.04	1.67	0.06	1.06	6.84	5.03
Cu(111)	6.68	4.94	11.03	1.64	1.06	0.06	6.85	5.03
	6.66	4.91	11.05	1.68	0.06	1.06	6.85	5.04
	6.64	4.90	11.02	1.65	1.05	0.06		

Chapter 6

Conclusions

The present work focused on the study of ultrathin ceria films on Cu(111) substrate representing the inverse model catalyst system with applications in hydrogen production in fuel cells. In particular we studied the structural and electronic properties of 1 and 2 ML thick ceria films on the copper substrate followed by the reactivity study of the water adsorption on these ultrathin films.

In the chapter 3 we summarized the results of previous works on copper-ceria interfaces in order to show the general trend at the interface. Every copper-ceria interface studied exhibited a charge transfer accompanied with a change of oxidation state of cerium ions. In particular the interface between copper adatom and stoichiometric CeO_2 included charge transfer from copper to ceria causing the reduction of Ce^{4+} ion to Ce^{3+}, while the interface between copper adatom and defective ceria with oxygen vacancy (which itself cause reduction of two Ce ions) instead exhibited charge transfer in opposite direction. In that case the metal was able to accommodate part of the excess charge left upon the vacancy creation and reoxidized one of the Ce^{3+} ions. This chapter also showed the results of the calculations of the local structure of larger CeO_2(111)/Cu(111) interface in terms of the mutual shift of the copper and ceria slab as well as the spatial separation of the two slabs.

In the chapter 4 we reported results of the calculations of structural and electronic properties of ultrathin ceria films on Cu(111). These results combined with the STM experimental observations allowed to identify and explain the special properties of the first monolayer of supported ceria compared to 2 ML or thicker films, which were ascribed to the finite size effect of the limited thickness of the film.

In particular the thin films of ceria were shown to exhibit compressive strain which was reduced either by increasing the thickness of the film or by including the Ce^{3+} ions or/and oxygen vacancies into the film. In this context it was shown that the 1 ML film contains an ordered array of vacancies which tend to segregate at the copper-ceria interface. The vacancies further allow for relieving the compression of the film and reduce the mismatch of the lattice parameter of the compressed 1 ML film and the lattice parameter of the copper substrate. The presence of oxygen vacancies was confirmed by comparison of simulated STM

image of the ceria film with subsurface vacancies with the atomically resolved STM experimental image of the first monolayer of ceria. Instead the experimental atomically resolved STM image of 2 ML film corresponded best to the simulated image of the stoichiometric 2 ML film. In contrast with the 1 ML film the 2 ML film showed preference of oxygen vacancies at the surface oxygen layer, where in reality they are easily refilled by the oxygen in atmosphere, thus we conclude, that the 2 ML film is stoichiometric.

The reason for the difference in the preferred site for the vacancy formation in the films with different thickness is in the different charge state of the films. As reported in the case of all copper-ceria interfaces, the charge transfer from copper to ceria causes ceria reduction. The reduction involves the whole ceria monolayer in contact with copper, which in the case of the 1 ML film includes all the Ce ions, while in the case of 2 ML the interface monolayer is reduced and the topmost monolayer contains Ce^{4+} ions. The electrons left behind upon vacancy creation in the case of 2 ML film can easily localize on the Ce^{4f} states of the topmost ceria layer, however in the case of 1 ML film containing exclusively Ce^{3+} ions they are accepted by the first layer of Cu.

The differences in the strain, structure (the presence and absence of vacancies) and electronic structure (Ce^{3+} and Ce^{4+} ions) are identified as a finite size effect, a result of the limited thickness of the film with possible implications on the reactivity of the films towards catalytic reactions.

In the chapter 5 we explored the water adsorption on the supported ultrathin ceria films to analyze the impact of the finite size effects on the reactivity of the surface. As a descriptor of the reactivity we used the binding energy of water.

First we analyzed water adsorption and dissociation on clean ceria slab to set a base line for further calculations and verify the validity of our calculations by comparison with results reported in the literature. Next we calculated properties of water molecule adsorbed molecularly and dissociatively on supported 2 ML ceria film, which exhibits local electronic and atomistic structure of the topmost monolayer similar to the termination of clean ceria slab. We show that the adsorption energies of water molecule in all studied configurations was stronger than on ceria slab. The effect of the copper-ceria interface in the case of water adsorption on 2 ML film compared to the clean ceria exhibited as an electrostatics effect reaching from the subsurface monolayer which is formed by Ce ions in 3+ and 4+ state for the 2 ML film and clean ceria slab respectively. The adsorption on the more charged 2 ML film resulted in difference in the bondlengths as well as the adsorbate induced charge transfer at the interface.

The adsorption of water molecule in the molecular and dissociative state on 1 ML film exhibited completely different trends. In contrast with almost similar adsorption energies for water molecule in MS1 and predissociated HP1 configurations on clean ceria and 2 ML film, the 1 ML film strongly prefers molecular adsorption. Moreover when predisociated, the OH group and H atom show tendencies to recombine or exhibit much shorter HO-H bond than in the case of HP1 structure on clean ceria slab or 2 ML film. The HP2 configuration was even less stable resulting in complete reorganization of the monolayer by displacing the Ce atom away from the monolayer by the adsorbed OH group.

In conclusion we showed that the properties of ultrathin ceria films induced by limited thickness of the film and the presence of the metallic interface underneath the film has significant impact on the reactivity of the films. Specifically for water adsorption and dissociation on thin ceria films it was shown that 1 ML ceria film shows strong preference for molecular adsorption, while molecular and dissociative adsorption are degenerate for 2 ML and thicker films.

Appendix A

Metastable electronic solutions - the case of copper-ceria interfaces

Here I will describe the difficulties with calculations of metal-ceria systems. I will show the existence of metastable electronic solutions for systems containing cerium oxides. In particular I will report the extreme case of the metal-oxide interface which exhibit metastable states even for occupation of particular Ce f orbitals.

The detailed review of the theoretical methods of calculating ceria based materials is given in the chapter 3. In the same chapter we also show the strengths and weaknesses of the different levels of the theory. The DFT+U is a method used in most theoretical analyses of ceria materials nowadays, since it is able to correctly describe the cerium oxides both in stoichiometric and reduced forms. However even DFT+U has its limits. Recent studies have shown existence of metastable solutions even for ceria with oxygen vacancies [69, 70, 71, 72]. The metastable solutions for defective ceria include the solutions with different positions of the Ce^{3+} ions created upon formation of the vacancy.

Other source of metastable solutions are adsorbates on ceria surfaces. In Ref. [73] the adsorption of vanadium oxide on ceria surface caused metastable states for different spin configurations of the system upon creating an oxygen vacancy. Even more complicated situation arise when the adsorbate is a metal. Metal adsorption on ceria induce charge transfer and is connected with ceria reduction [23]. Also this case, when electrons have to be localized on Ce ions, allow for existence of metastable solutions with different position of Ce^{3+} ions with respect to the adsorbate. Such complication arise even for the smallest case of metal-oxide interface in form of single adsorbate on ceria surface. Here I will show that the problem of metastable solutions lies not only in the configuration of Ce^{3+} ions but also in the exact electronic structure of the system. In particular I will show the case of extended copper-ceria interface which allow the appearance of metastable states even for the occupation of different cerium f orbitals.

Our calculations revealed a large number of metastable electronic solutions for a supercell with the same atomic coordinates, depending on the starting electronic conditions of Ce f states. Namely when starting from different starting magnetization of Ce atoms or Ce f orbital occupations we can get a result differing in total energy by more than 1 eV. The difference between the results lie in the

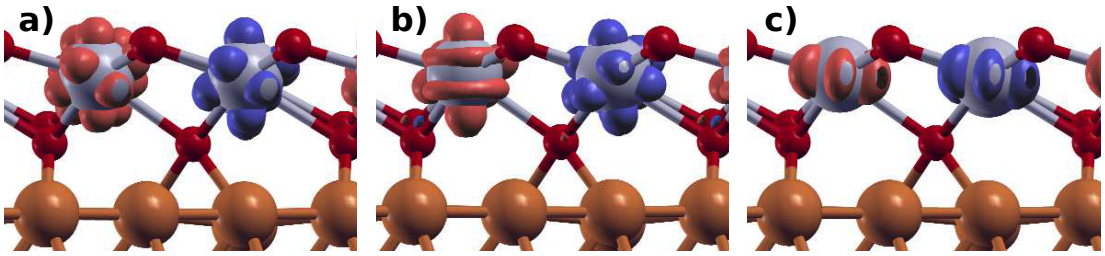

Figure A.1: Spin density of 1 ML CeO_2/Cu(111) with different Ce f occupations. The most stable electronic result (a), an example of less stable result with different shape of f orbital (b), the least stable solution with f orbitals oriented in plane parallel to the interface (c)

occupation of particular Ce^I f state of each of the four Ce^I atoms in the reduced interfacial cerium atomic layer. Examples of such different resulting electronic structures are reported in the Fig. A.1.

The figures show three different spin densities of supercell with identical atomic coordinates corresponding to the structure of 1 ML CeO_2/Cu(111)(S) described in previous chapter. The spin density in subfigure (a) corresponds to the electronic structure with lowest obtained energy and subfigure (b) electronic structure with different shape of spin density on one of the four cerium ions and energy higher by 0.14 eV. Both of these calculations were started by specifying starting magnetization of two Ce ions as positive and two as negative. The difference of the starting structure was in setting different starting eigenvalues for the Ce f states to suggest different orbital occupations of the resulting electronic structure. Such manipulation is usually necessary in cases when the default choice of the program doesn't lead to correct localization of an electron in the Ce f state.

By further exploring the space of metastable solutions we obtained even more different solution with spin densities on all four Ce ions oriented in the plane parallel to the interface (Fig. A.1 (c)) and energy higher by 1.4 than the result in the subfigure (a), the highest from all the obtained solutions. The procedure is based on starting the calculation with higher value of the U parameter (in this case we chose 8.5 eV) to force occupation of different Ce f orbitals. The resulting electron density was then used in subsequent calculation with a usual value of U=4.5 eV.

The energy of the most stable solution of 1 ML CeO_2/Cu(111)(S) system gained by thorough exploration of the possible starting electronic configurations during this further study is 0.3 eV lower than energy of the electronic structure obtained during the calculations reported in chapter 4. However we don't expect the conclusions of the chapter 4 to be considerably influenced by these new results as the conclusions were based mostly on the overall electronic and structural properties of the thin films which are consistent for the different Ce f occupations.

The stability of these metastable solutions was verified by further tests employing increased k-point mesh to 6×6×1 and different smearing values 0.005 Ry and 0.04 Ry compared to usual 0.02 Ry. Starting from the electronic density of the metastable state, the selfconsistent calculation with these changed parameters provided solution of electronic density and thus occupations of the Ce f states

corresponding to the starting density.

Thorough analysis of starting electronic configurations were performed also on other studied systems. Namely 1 ML $CeO_{1.75}$/Cu(111) exhibited structures with total energies within 0.8 eV. The electronic structure described in chapter 4 provided actually the lowest total energy of the system. The reconstructed 1 ML CeO_2/Cu(111)(R) described in the above paragraph allowed for electronic structures with total energies within 0.7 eV. Considering the large range of the total energies of individual substrates, the difference between the two different structures of 1 ML CeO_2/Cu(111) (S) and (R) cells 0.3 eV can be as well ascribed to the different occupied Ce f orbitals in both cases.

The last studied system with 2 ML CeO_2/Cu(111) showed much more stability in the electronic structure of the solutions, the occupied f orbitals were the same in most cases and the interval of total energies was less than 0.3 eV. The electronic solution reported in chapter 4 was less stable by 0.12 eV than the most stable structure obtained by further exploring the space of initial electronic structures. This result shows, that these metastable states come from the presence of the metal substrate and is stabilized at the thicker oxide film.

This thorough analysis provides an evidence of the difficulty to obtain the real ground state electronic structure for systems with large metal-oxide interface. We show that for a system with the same atomic coordinates we were able to stabilize large number of metastable solutions with different electronic structures due to the metalicity and the charge state at the interface. These calculations allowed us to get an upper bound for the total energy as well as the estimate of which f orbital is the most stable for the case of copper/ceria interface. We showed, that a large number of carefully performed calculations are necessary in order to map the potential energy space and achieve the ground state of the system.

Appendix B

List of Tables

- Table 12 (5.6): Löwdin charges of atoms in subsurface O-Ce-O monolayer of ceria in the 3 ML CeO_2 and 2 ML CeO_2/Cu(111) cases before and after adsorption of water molecule in MS1 configuration.
- Table 13 (5.7): Lowdin charges of H-O-H on different substrates
- Table 14 (5.8): Lowdin charges of atoms in the surface ceria monolayer of different supercells before and after adsorption of water molecule in MS1 configuration.

Appendix C

List of Abbreviations

- **DFT:** Density Functional Theory
- **DOS:** Density of States
- **fcc:** face centered cubic
- **GGA:** Generalized Gradient Approximation
- **HRTEM:** High Resolution Transmission Electron Microscopy
- **LDA:** Local Density Approximation
- **LEED:** Low energy electron diffraction
- **LSDA:** Local Spin Density Approximation
- **ML:** monolayer
- **NC-AFM:** Non-contact Atomic Force Microscopy
- **OSC:** Oxygen Storage Capacity
- **PBE:** Perdew-Burke-Ernzerhof
- **pDOS:** Projected Density of States
- **PEMFC:** Proton Exchange Membrane Fuel Cell
- **STM:** Scanning Tunneling Microscopy
- **TDS:** Thermal Desorption Spectroscopy
- **TPD:** Thermally Programmed Desorption
- **WGS:** Water Gas Shift
- **XPS:** X-ray Photoelectron Spectroscopy

Appendix D

CD-ROM

The CD-ROM contains the Doctoral thesis in the pdf formate.

Bibliography

[1] Liu, Y., Fu, Q., and Flytzani-Stephanopoulos, M. (2004) Preferential oxidation of CO in H_2 over CuO-CeO_2 catalysts. *Catal. Today*, **93-95**, 241–246, ISSN 0920-5861.

[2] Fu, Q., Saltsburg, H., and Flytzani-Stephanopoulos, M. (2003) Active nonmetallic Au and Pt species on ceria-based water-gas shift catalysts. *Science*, **301**, 935, ISSN 0036-8075.

[3] Václavů, M., Matolínová, I., Mysliveček, J., Fiala, R., and Matolín, V. (2009) Anode material for hydrogen polymer membrane fuel cell: Pt-CeO_2 RF-sputtered thin films. *J. Electrochem. Soc.*, **156**, B938–B942, ISSN 0013-4651.

[4] Matolín, V., Fiala, R., Khalakhan, I., Lavková, J., Václavů, M., and Vorokhta, M. (2012) Nanoporous Pt^{n+}-CeO_x catalyst films grown on carbon substrates. *Int. J. Nanotechnol.*, **9**, 680, ISSN 1475-7435.

[5] Matolín, V., et al. (2010) Platinum-doped CeO_2 thin film catalysts prepared by magnetron sputtering. *Langmuir*, **26**, 12824–12831, ISSN 0743-7463.

[6] Matolín, V., et al. (2010) Pt and Sn doped sputtered CeO_2 electrodes for fuel cell applications. *Fuel Cells*, **10**, 139–144, ISSN 1615-6854.

[7] Yen, H., Seo, Y., Kaliaguine, S., and Kleitz, F. (2012) Tailored mesostructured copper/ceria catalysts with enhanced preformance for preferential oxidation of CO at low temperature. *Angew. Chem. Int. Ed.*, **51**, 12032–12035, ISSN 1521-3773.

[8] Mullins, D. R., Overbury, S. H., and Huntley, D. R. (1998) Electron spectroscopy of single crystal and polycrystalline cerium oxide surfaces. *Surf. Sci.*, **409**, 307, ISSN 0039-6028.

[9] Liu, W. and Flytzani-Stephanopoulos, M. (1995) Total oxidation of carbon monoxide and methane over transition metal fluorite oxide composite catalysts: I. Catalyst composition and activity. *J. Catal.*, **153**, 304–316, ISSN 0021-9517.

[10] Liu, W. and Flytzani-Stephanopoulos, M. (1995) Total oxidation of carbonmonoxide and methane over transition metal fluorite oxide composite catalysts: II. Catalyst characterization and reaction-kinetics. *J. Catal.*, **153**, 317–332, ISSN 0021-9517.

[11] Liu, W. and Flytzani-Stephanopoulos, M. (1996) Transition metal-promoted oxidation catalysis by fluorite oxides: A study of CO oxidation over Cu-CeO_2. *Chem. Eng. J. and Biochem. Eng. J.*, **64**, 283–294, ISSN 1385-8947.

[12] Li, Y., Fu, Q., and Flytzani-Stephanopoulos, M. (2000) Low-temperature water-gas shift reaction over Cu- and Ni-loaded cerium oxide catalysts. *Appl. Catal., B: Environmental*, **27**, 179–191, ISSN 0926-3373.

[13] Liu, Y., Hayakawa, T., Suzuki, K., and Hamakawa, S. (2001) Production of hydrogen by steam reforming of methanol over Cu/CeO_2 catalysts derived from $Ce_{1-x}Cu_xO_{2-x}$ precursors. *Catal. Comm.*, **2**, 195–200, ISSN 1566-7367.

[14] Trovarelli, A. (2002) *Catalysis by Ceria and Related Materials*. Imperial College Press, ISBN 978-1-86094-299-0.

[15] Flytzani-Stephanopoulos, M., Sakbodin, M., and Wang, Z. (2006) Regenerative adsorption and removal of H_2S from hot fuel gas streams by rare earth oxides. *Science*, **312**, 1508, ISSN 0036-8075.

[16] Skarman, B., Grandjean, D., Benfield, R. E., Hinz, A., Andersson, A., and Wallenberg, L. R. (2002) Carbon monoxide oxidation on nanostructured $CuOx/CeO_2$ composite particles characterized by HREM, XPS, XAS, and high-energy diffraction. *J. Catal.*, **211**, 119, ISSN 0021-9517.

[17] Jung, C. R., Han, J., Nam, S. W., Lim, T.-H., Hong, S.-A., and Lee, H.-I. (2004) Selective oxidation of CO over CuO-CeO_2 catalyst: Effect of calcination temperature. *Catal. Today*, **93-95**, 183–190, ISSN 0920-5861.

[18] Bera, P., Aruna, S. T., Patil, K. C., and Hegde, M. S. (1999) Studies on Cu/CeO_2: A new NO reduction catalyst. *J. Catal.*, **186**, 36–44, ISSN 0021-9517.

[19] Avgouropoulos, G., Ioannides, T., Matralis, H. K., Batista, J., and Hocevar, S. (2001) CuO-CeO_2 mixed oxide catalysts for the selective oxidation of carbon monoxide in excess hydrogen. *Catal. Lett.*, **73**, 33, ISSN 1011-372X.

[20] Hungría, A. B., Iglesias-Juez, A., Martínez-Arias, A., Fernández-García, M., Anderson, J. A., Conesa, J. C., and Soria, J. (2002) Effects of copper on the catalytic properties of bimetallic Pd-Cu/(Ce,Zr)O_x/Al_2O_3 and Pd-Cu/(Ce,Zr)O_x catalysts for CO and NO elimination. *J. Catal.*, **206**, 281, ISSN 0021-9517.

[21] Arroyo-De Dompablo, M. E., Morales-Garca, A., and Taravillo, M. (2011) DFT+U calculations of crystal lattice, electronic structure, and phase stability under pressure of TiO_2 polymorphs. *J. Chem. Phys.*, **139**, 054503, ISSN 0021-9606.

[22] Fernández-Torre, D., Kósmider, K., Carrasco, J., Ganduglia-Pirovano, V. M., and Pérez, R. (2012) Insight into the adsorption of water on the clean CeO_2(111) surface with van der Waals and hybrid density functionals. *J. Phys. Chem. C*, **116**, 13584–13593, ISSN 1932-7447.

[23] Paier, J., Penschke, C., and Sauer, J. (2013) Oxygen defects and surface chemistry of ceria: Quantum chemical studies compared to experiment. *Chem. Rev.*, **113**, 3949–3985, ISSN 0009-2665.

[24] Berner, U., Schierbaum, K., Jones, G., Wincott, P., Haq, S., and Thornton, G. (2000) Ultrathin ordered CeO_2 overlayers on Pt(111): Interaction with NO_2, NO, H_2O and CO. *Surf. Sci.*, **467**, 201–213, ISSN 0039-6028.

[25] Senanayake, S. D., Stacchiola, D., Evans, J., Estrella, M., Barrio, L., Perez, M., Hrbek, J., and Rodriguez, J. A. (2010) Probing the reaction intermediates for the water-gas shift over inverse CeO_x/Au(111) catalysts. *J. Catal.*, **271**, 392–400, ISSN 0021-9517.

[26] Otsuka, K., Hatano, M., and Morikawa, A. (1983) Hydrogen from water by reduced cerium oxide. *J. Catal.*, **79**, 493–496, ISSN 0021-9517.

[27] Padeste, C., Cant, N. W., and Trimm, D. L. (1993) The influence of water on the reduction and reoxidation of ceria. *Catal. Lett*, **18**, 305–316, ISSN 1011-372X.

[28] Kundakovic, L., Mullins, D. R., and Overbury, S. H. (2000) Adsorption and reaction of H_2O and CO on oxidized and reduced Rh/CeO_x(111) surfaces. *Surf. Sci.*, **457**, 51–62, ISSN 0039-6028.

[29] Martin, R. M. (2004) *Electronic Structure*. Cambridge University Press, ISBN 0521534402.

[30] Giannozzi, P. Corso di Laurea in Fisica Computazionale.

[31] Hohenberg, P. and Kohn, W. (1964) Inhomogeneous electron gas. *Phys. Rev.*, **136**, B864, ISSN 1943-2879.

[32] Kohn, W. and Sham, L. J. (1965) Self-consistent equations including exchange and correlation effects. *Phys. Rev.*, **140**, A1133, ISSN 1943-2879.

[33] Cococcioni, M. (2002) A LDA+U study of selected iron compounds. *Diploma thesis*.

[34] Perdew, J. P., Burke, K., and Ernzherof, M. (1996) Generalized gradient approximation made simple. *Phys. Rev. Lett.*, **77**, 3865–3868, ISSN 0031-9007.

[35] Monkhorst, H. J. and Pack, J. D. (1976) Special points for Brillouin-zone integrations. *Phys. Rev. B*, **13**, 5188, ISSN 1098-0121.

[36] de Gironcoli, S. (1995) Lattice dynamics of metals from density-functional perturbation theory. *Phys. Rev. B*, **51**, 6773, ISSN 1098-0121.

[37] Fu, C. L. and Ho, K. M. (1983) First-principles calculation of the equilibrium ground-state properties of transition metals: Applications to Nb and Mo. *Phys. Rev. B*, **28**, 5480, ISSN 1098-0121.

[38] Marzari, N., Vanderbilt, D., Vita, A. D., and Payne, M. C. (1999) Thermal contraction and disordering of the Al(110) surface. *Phys. Rev. Lett.*, **82**, 3296, ISSN 0031-9007.

[39] Methfessel, M. and Paxton, A. T. (1989) High-precision sampling for brillouin-zone integration in metals. *Phys. Rev. B*, **40**, 3616, ISSN 1098-0121.

[40] Vanderbilt, D. (1990) Soft self-consistent pseudopotentials in a generalized eigenvalue formalism. *Phys. Rev. B*, **41**, 7892, ISSN 1098-0121.

[41] Anisimov, V. I., Zaanen, J., and Andersen, O. K. (1991) Band theory and Mott insulators: Hubbard U instead of Stoner I. *Phys. Rev. B*, **44**, 943, ISSN 1098-0121.

[42] Anisimov, V. I., Solovyev, I. V., Korotin, M. A., Czyzyk, M. T., and Sawatzky, G. A. (1993) Density-functional theory and NiO photoemission spectra. *Phys. Rev. B*, **48**, 16929, ISSN 1098-0121.

[43] Solovyev, I. V., Dederichs, P. H., and Anisimov, V. I. (1994) Corrected atomic limit in the local-density approximation and the electronic structure of d impurities in Rb. *Phys. Rev. B*, **50**, 16861, ISSN 1098-0121.

[44] Lichtenstein, A. I. and Katsnelson, M. I. (1998) Ab initio calculations of quasiparticle band structure in correlated systems: LDA++ approach. *Phys. Rev. B*, **57**, 6884, ISSN 1098-0121.

[45] Cococcioni, M. and de Gironcoli, S. (2005) Linear response approach to the calculation of the effective interaction parameters in the LDA+U method. *Phys. Rev. B*, **71**, 035105, ISSN 1098-0121.

[46] Fabris, S., de Gironcoli, S., Baroni, S., Vicario, G., and Balducci, G. (2005) Taming multiple valency with density functionals: A case study of defective ceria. *Phys. Rev. B*, **71**, 041102, ISSN 1098-0121.

[47] Boys, S. F. (1960) Construction of some molecular orbitals to be approximately invariant for changes from one molecule to another. *Rev. Mod. Phys.*, **32**, 296, ISSN 0034-6861.

[48] Marzari, N. and Vanderbilt, D. (1997) Maximally localized generalized Wannier functions for composite energy bands. *Phys. Rev. B*, **56**, 12847, ISSN 1098-0121.

[49] Fabris, S., Vicario, G., Balducci, G., de Gironcoli, S., and Baroni, S. (2005) Electronic and atomistic structures of clean and reduced ceria surfaces. *J. Phys. Chem. B*, **109**, 22860–22867, ISSN 1520-6106.

[50] Fabris, S., de Gironcoli, S., Baroni, S., Vicario, G., and Balducci, G. (2005) Reply to "Comment on 'Taming multiple valency with density functionals: A case study of defective ceria"'. *Phys. Rev. B*, **72**, 237102, ISSN 1098-0121.

[51] Huang, M. and Fabris, S. (2007) Role of surface peroxo and superoxo species in the low-temperature oxygen buffering of ceria: Density functional theory calculations. *Phys. Rev. B*, **75**, 081404, ISSN 1098-0121.

[52] Huang, M. and Fabris, S. (2008) CO adsorption and oxidation on ceria surfaces from DFT+U calculations. *J. Phys. Chem. C*, **112**, 8643–8648, ISSN 1932-7447.

[53] Colussi, S., Gayen, A., Farnesi Camellone, M., Boaro, M., Llorca, J., Fabris, S., and Trovarelli, A. (2009) Nanofaceted PdO sites in PdCe surface superstructures: Enhanced activity in catalytic combustion of methane. *Angewandte Chemie*, **48**, 8481–8484, ISSN 1521-3757.

[54] Farnesi, M. and Fabris, S. (2009) Reaction mechanisms for the CO oxidation on Au/CeO_2 catalysts: Activity of substitutional Au^{3+} cations and deactivation of supported Au^{+} adatoms. *J. Am. Chem. Soc.*, **131**, 10473, ISSN 0002-7863.

[55] Szabová, L., Farnesi Camellone, M., Huang, M., Matolín, V., and Fabris, S. (2010) Thermodynamic, electronic and structural properties of Cu/CeO_2 surfaces and interfaces from first-principles DFT+U calculations. *J. Chem. Phys.*, **133**, 234705, ISSN 0021-9606.

[56] Szabová, L., Stetsovych, O., Dvořák, F., Farnesi Camellone, M., Fabris, S., Mysliveček, J., and Matolín, V. (2012) Distinct physicochemical properties of the first ceria monolayer on Cu(111). *J. Phys. Chem. C*, **116**, 6677–6684, ISSN 1932-7447.

[57] Szabová, L. (2009) Master's thesis, Faculty of Mathematics and Physics, Charles University, Prague.

[58] Szabová, L., Skála, T., Matolínová, I., Fabris, S., Farnesi Camellone, M., and Matolín, V. (2013) Copper-ceria interaction: A combined photoemission and DFT study. *Appl. Surf. Sci.*, **267**, 12–16, ISSN 0169-4332.

[59] Wyckoff, R. W. G. (1961) *Crystal Structures*. Wiley-Interscience, ISBN 0470968621.

[60] Koelling, D. D., Boring, A. M., and Wood, J. H. (1983) The electronic-structure of ceO_2 and prO_2. *Solid State Commun.*, **47**, 227, ISSN 0038-1098.

[61] Hill, S. and Catlow, C. (1993) A Hartree-Fock periodic study of bulk ceria. *J. Phys. Chem. Solids*, **54**, 411, ISSN 0022-3697.

[62] Skorodumova, N. V., Ahuja, R., Simak, S. I., Abrikosov, I. A., Johansson, B., and Lundquist, B. I. (2001) Electronic, bonding and optical properties of CeO_2 and Ce_2O_3 from first principles. *Phys. Rev. B*, **64**, 115108, ISSN 1098-0121.

[63] Skorodumova, N. V., Simak, S. I., Lundqvist, B. I., Abrikosov, I. A., and Johansson, B. (2002) Quantum origin of the oxygen storage capability of ceria. *Phys. Rev. Let.*, **89**, 166601, ISSN 0031-9007.

[64] Gennard, S., Corá, F., and Catlow, C. R. A. (1999) Comparison of the bulk and surface properties of ceria and zirconia by ab initio investigations. *J. Phys. Chem. B*, **103**, 10158, ISSN 1520-6106.

[65] Skorodumova, N. V., Baudin, M., and Hermansson, K. (2004) Surface properties of CeO_2 from first principles. *Phys. Rev. B*, **69**, 075401, ISSN 1098-0121.

[66] Andersson, D. A., Simak, S. I., Johansson, B., Abrikosov, I. A., and Skorodumova, N. V. (2007) Modeling of CeO_2, Ce_2O_3 and CeO_{2-x} in the LDA+U formalism. *Phys. Rev. B*, **75**, 035109, ISSN 1098-0121.

[67] Da Silva, J. L. F., Ganduglia-Pirovano, M. V., Sauer, J., Bayer, V., and Kresse, G. (2007) Hybrid functionals applied to rare-earth oxides: The example of ceria. *Phys. Rev. B*, **75**, 045121, ISSN 1098-0121.

[68] Nolan, M., Grigoleit, S., Sayle, D. C., Parker, S. C., and Watson, G. W. (2005) Density functional theory studies of the structure and electronic structure of pure and defective low index surfaces of ceria. *Surf. Sci.*, **576**, 217–229, ISSN 0039-6028.

[69] Ganduglia-Pirovano, M. V., Da Silva, J. L. F., and Sauer, J. (2009) Density-functional calculations of the structure of near-surface oxygen vacancies and electron localization on $CeO_2(111)$. *Phys. Rev. Lett.*, **102**, 026101, ISSN 0031-9007.

[70] Li, H.-Y., Wang, H.-F., Gong, X.-Q., Guo, Y.-L., Guo, Y., Lu, G., and Hu, P. (2009) Multiple configurations of the two excess 4f electrons on defective CeO_2 (111): Origin and implications. *Phys. Rev. B*, **79**, 193401, ISSN 1098-0121.

[71] Jerratsch, J. F., Shao, X., Nilius, N., Freund, H.-J., Popa, C., Ganduglia-Pirovano, M. V., Burow, A. M., and Sauer, J. (2011) Electron localization in defective ceria films: A study with scanning-tunneling microscopy and density-functional theory. *Phys. Rev. Lett.*, **106**, 246801, ISSN 0031-9007.

[72] Conesa, J. C. (2009) Surface anion vacancies on ceria: Quantum modelling of mutual interactions and oxygen adsorption. *Catal. Today*, **143**, 315–325, ISSN 0920-5861.

[73] Penschke, C., Paier, J., and Sauer, J. (2013) Oligomeric vanadium oxide species supported on the $CeO_2(111)$ surface: Structure and reactivity studied by density functional theory. *J. Phys. Chem. C.*, **117**, 5274–5285, ISSN 1932-7447.

[74] Mayernick, A. D. and Janik, M. J. (2009) Ab initio thermodynamic evaluation of Pd atom interaction with CeO_2 surfaces. *J. Chem. Phys.*, **131**, 084701, ISSN 0021-9606.

[75] Wilson, E. L., Grau-Crespo, R., Pang, C. L., Cabailh, G., Chen, Q., Purton, J. A., Catlow, C. R. A., Brown, W. A., de Leeuw, N. H., and Thornton, G. (2008) Redox behavior of the model catalyst $Pd/CeO_{2-x}/Pt(111)$. *J. Phys. Chem. C*, **112**, 10918, ISSN 1932-7447.

[76] Alfredsson, M. and Catlow, C. R. A. (2002) A comparison between metal supported C-ZrO_2 and CeO_2. *Phys. Chem. Chem. Phys.*, **4**, 6100–6108, ISSN 1463-9076.

[77] Lu, Z. S. and Yang, Z. X. (2010) Interfacial properties of $NM/CeO_2(111)$ (NM = noble metal atoms or clusters of Pd, Pt and Rh): A first principles study. *J. Phys.: Condens. Matter*, **22**, 475003, ISSN 0953-8984.

[78] G. N. Vayssilov and Y. Lykhach and A. Migani and T. Staudt and G. P. Petrova and N. Tsud and T. Skála and A. Bruix and F. Illas and K. C. Prince and V. Matolín and K. M. Neyman and J. Libuda (2011) Support nanostructure boosts oxygen transfer to catalytically active platinum nanoparticles. *Nature Materials*, **10**, 310, ISSN 1476-1122.

[79] Yang, Z., Lu, Z., and Luo, G. (2007) First-principles study of the $Pt/CeO_2(111)$ interface. *Phys. Rev. B*, **76**, 075421, ISSN 1098-0121.

[80] Loffreda, D. and Delbecq, F. (2012) Growth of a Pt film on non-reduced ceria: A density functional theory study. *J. Chem. Phys.*, **136**, 044705, ISSN 0021-9606.

[81] Branda, M. M., Castellani, N. J., Grau-Crespo, R., Leeuw, N. H. D., Hernandez, N. C., Sanz, J. F., Neyman, K. M., and Illas, F. (2009) On the difficulties of present theoretical models to predict the oxidation state of atomic Au adsorbed on regular sites of CeO_2 (111). *J. Chem. Phys.*, **131**, 094702, ISSN 0021-9606.

[82] Branda, M. M., Henandez, N. C., Sanz, J. F., and Illas, F. (2010) Density functional theory study of the interaction of Cu, Ag, and Au atoms with the regular CeO_2 (111) surface. *J. Phys. Chem. C*, **114**, 1934, ISSN 1932-7447.

[83] Zhang, C., Michaelides, A., King, D., and Jenkins, S. J. (2008) Structure of gold atoms on stoichiometric and defective ceria surfaces. *J. Chem. Phys.*, **129**, 194708, ISSN 0021-9606.

[84] Zhang, C., Michaelides, A., King, D., and Jenkis, S. J. (2009) Anchoring sites for initial Au nucleation on $CeO_2(111)$: O vacancy versus Ce vacancy. *J. Phys. Chem. C*, **113**, 6411–6417, ISSN 1932-7447.

[85] Hernandez, N. C., Grau-Crespo, R., de Leeuw, N. H., and Sanz, J. F. (2009) Electronic charge transfer between ceria surfaces and gold adatoms:

A GGA+U investigation. *Phys. Chem. Chem. Phys.*, **11**, 5246–5252, ISSN 1463-9076.

[86] Zhang, C. J., Michaelides, A., and Jenkins, S. J. (2011) Theory of gold on ceria. *Phys. Chem. Chem. Phys.*, **13**, 22–33, ISSN 1463-9076.

[87] Luches, P., Pagliuca, F., Valeri, S., Illas, F., Preda, G., and Pacchioni, G. (2012) Nature of Ag islands and nanoparticles on the CeO_2(111) surface. *J. Phys. Chem. C.*, **116**, 1122–1132, ISSN 1932-7447.

[88] Yang, Z. X., Xie, L. G., Ma, D. W., and Wang, G. T. (2011) Origin of the high activity of the ceria-supported copper catalyst for H_2O dissociation. *J. Phys. Chem. C*, **115**, 6730–6740, ISSN 1932-7447.

[89] Yang, Z., He, B., Lu, Z., and Hermansson, K. (2010) Physisorbed, chemisorbed, and oxidized CO on highly active Cu-CeO_2(111). *J. Phys. Chem. C*, **114**, 4486–4494, ISSN 1932-7447.

[90] Hay, P. J., Martin, R. L., Uddin, J., and Scuseria, G. E. (2006) Theoretical study of CeO_2 and Ce_2O_3 using a screened hybrid density functional. *J. Chem. Phys.*, **125**, 034712, ISSN 0021-9606.

[91] Da Silva, J. L. F., Ganduglia-Pirovano, M. V., Sauer, J., Bayer, V., and Kresse, G. (2007) Hybrid functionals applied to rare-earth oxides: The example of ceria. *Phys. Rev. B*, **75**, 045121, ISSN 1098-0121.

[92] Perdew, J. P., Ernzerhof, M., and Burke, K. (1996) Rationale for mixing exact exchange with density functional approximations. *J. Chem. Phys.*, **105**, 9982–9985, ISSN 0021-9606.

[93] Becke, A. D. (1993) Density-functional thermochemistry. III. The role of exact exchange. *J. Chem. Phys.*, **98**, 5648–5652, ISSN 0021-9606.

[94] Giannozzi, P., et al. (2009) Quantum ESPRESSO: A modular and open-source software project for quantum simulations of materials. *J. Phys.: Condens. Matter*, **21**, 395502, ISSN 0953-8984.

[95] Loschen, C., Carrasco, J., Neyman, K. M., and Illas, F. (2007) First-principles LDA+U and GGA+U study of cerium oxides: Dependence on the effective U parameter. *Phys. Rev. B*, **75**, 035115, ISSN 1098-0121.

[96] Nolan, M. and Watson, G. (2006) The surface dependence of CO adsorption on ceria. *J. Phys. Chem. B*, **110**, 16600–16606, ISSN 1520-6106.

[97] Kokalj, A. (1999) XCrySDen-a new program for displaying crystalline structures and electron densities. *J. Mol. Graphics Modelling*, **17**, 176–179, ISSN 1093-3263.

[98] Kittel, C. (1996) *Introduction to solid state physics*. Wiley, ISBN 047141526X.

[99] Perdew, J. P., Chevary, J. A., Vosko, S. H., Jackson, K. A., Pederson, M. R., Singh, D. J., and Fiolhais, C. (1992) Atoms, molecules, solids, and surfaces: Applications of the generalized gradient approximation for exchange and correlation. *Phys. Rev. B*, **46**, 6671, ISSN 1098-0121.

[100] Gerward, L., Olsen, J. S., Petit, L., Vaitheeswaran, G., Kanchana, V., and Svanee, A. (2005) Bulk modulus of CeO_2 and PrO_2-an experimental and theoretical study. *Journal of Alloys and Compounds*, **400**, 56–61, ISSN 0925-8388.

[101] Duclos, S., Vohra, Y., Ruoff, A., Jayaraman, A., and Espinosa, G. (1988) High-pressure x-ray diffraction study of CeO_2 to 70 GPa and pressure-induced phase transformation from the fluorite structure. *Phys. Rev. B*, **38**, 7755, ISSN 1098-0121.

[102] Gerward, L. and Olsen, J. (1993) Powder diffraction analysis of cerium dioxide at high pressure. *Powder Diffr.*, **8**, 127, ISSN 0885-7156.

[103] Yang, Z., an Gaixia Luo, Z. L., and Hermansson, K. (2007) Oxygen vacancy formation energy at the $Pd/CeO_2(111)$ interface. *Phys. Lett. A*, **369**, 132–139, ISSN 0375-9601.

[104] Rodríguez, J. A., Evans, J., Graciani, J., Park, J.-B., Liu, P., Hrbek, J., and Sanz, J. F. (2009) High water-gas shift activity in $TiO_2(110)$ supported Cu and Au nanoparticles: Role of the oxide and metal particle size. *J. Phys. Chem. C*, **113**, 7364–7370, ISSN 1932-7447.

[105] Matolín, V., Sedláček, L., Matolínová, I., Šutara, F., Skála, T., Šmíd, B., Libra, J., Nehasil, V., and Prince, K. C. (2008) Photoemission spectroscopy study of Cu/CeO_2 systems: Cu/CeO_2 nanosized catalyst and $CeO_2(111)/Cu(111)$ inverse model catalyst. *J. Phys. Chem. C*, **112**, 3751–3758, ISSN 1932-7447.

[106] Šutara, F., Cabala, M., Sedláček, L., Skála, T., Škoda, M., Matolín, V., Prince, K. C., and Cháb, V. (2008) Epitaxial growth of continuous $CeO_2(111)$ ultra-thin films on Cu(111). *Thin Solid Films*, **516**, 6120–6124, ISSN 0040-6090.

[107] Matolín, V., Libra, J., Matolínová, I., Nehasil, V., Sedláček, L., and Šutara, F. (2007) Growth of ultra-thin cerium oxide layers on Cu(111). *App. Surf. Sci.*, **254**, 153–155, ISSN 0169-4332.

[108] Freund, H.-J. (2002) Clusters and islands on oxides: From catalysis via electronics and magnetism to optics. *Surf. Sci.*, **500**, 271–299, ISSN 0039-6028.

[109] Freund, H.-J. (2007) Metal-supported ultrathin oxide film systems as designable catalysts and catalyst supports. *Surf. Sci*, **601**, 1438–1442, ISSN 0039-6028.

[110] Netzer, F. P., Allegretti, F., and Surnev, S. (2010) Low-dimensional oxide nanostructures on metals: Hybrid systems with novel properties. *J. Vac. Sci. Technol. B*, **28**, 1–16, ISSN 1071-1023.

[111] Weiss, W. and Ritter, M. (1999) Metal oxide heteroepitaxy: Stranski-Krastanov growth for iron oxides on Pt(111). *Phys. Rev. B*, **59**, 5201–5213, ISSN 1098-0121.

[112] König, T., Simon, G. H., Rust, H.-P., and Heyde, M. (2009) Work function measurements of thin oxide films on metals - MgO on Ag(001). *J. Phys. Chem. C*, **113**, 11301–11305, ISSN 1932-7447.

[113] Kresse, G., Schmid, M., Napetschnig, E., Shishkin, M., Köhler, L., and Varga, P. (2005) Materials science: Structure of the ultrathin aluminum oxide film on NiAl(110). *Science*, **308**, 1440–1442, ISSN 0036-8075.

[114] Netzer, F. P. (2010) "Small and beautiful" - The novel structures and phases of nano-oxides. *Surf. Sci.*, **604**, 485–489, ISSN 0039-6028.

[115] Sterrer, M., Risse, T., Pozzoni, U. M., Giordano, L., Heyde, M., Rust, H.-P., Pacchioni, G., and Freund, H.-J. (2007) Crossover from three-dimensional to two-dimensional geometries of Au nanostructures on thin MgO(001) films: A confirmation of theoretical predictions. *Phys. Rev. Lett.*, **98**, 096107, ISSN 0031-9007.

[116] Sock, M., Surnev, S., Ramsey, M. G., and Netzer, F. P. (2001) Adsorption and reaction of CO on vanadium oxide-Pd(111) "inverse" model catalysts: An HREELS study. *Top. Catal.*, **14**, 15–23, ISSN 1022-5528.

[117] Rodríguez, J. A. and Hrbek, J. (2010) Inverse oxide/metal catalysts: A versatile approach for activity tests and mechanistic studies. *Surf. Sci*, **604**, 241–244, ISSN 0039-6028.

[118] Mullins, D. R., Radulovic, P. V., and Overbury, S. H. (1999) Ordered cerium oxide thin films grown on Ru(0001) and Ni(111). *Surf. Sci.*, **429**, 186–198, ISSN 0039-6028.

[119] Lu, D.-L., Gao, H.-J., Shaikhutdinov, S., and Freund, H.-J. (2006) Morphology and defect structure of the CeO_2(111) films grown on Ru(0001) as studied by scanning tunneling microscopy. *Surf. Sci.*, **600**, 5004–5010, ISSN 0039-6028.

[120] Dvořák, F., Stetsovych, O., Steger, M., Cherradi, E., Matolínová, I., Tsud, N., Škoda, M., Skála, T., Mysliveček, J., and Matolín, V. (2011) Adjusting morphology and surface reduction of CeO_2(111) thin films on Cu(111). *J. Phys. Chem. C*, **115**, 7496–7503, ISSN 1932-7447.

[121] Mullins, D. R., Robbins, M. D., and Zhou, J. (2006) Adsorption and reaction of methanol on thin-film cerium oxide. *Surf. Sci.*, **600**, 1547–1558, ISSN 0039-6028.

[122] Staudt, T., Lykhach, Y., Tsud, N., Skála, T., Prince, K. C., Matolín, V., and Libuda, J. (2010) Ceria reoxidation by CO_2: A model study. *J. Catal.*, **275**, 181–185, ISSN 0021-9517.

[123] Zhou, J. and Mullins, D. R. (2006) Rh-promoted methanol decomposition on cerium oxide thin films. *J. Phys. Chem. B*, **110**, 15994–16002, ISSN 1520-6106.

[124] Baron, M., Bondarchuk, O., Stacchiola, D., Shaikhutdinov, S., and Freund, H.-J. (2009) Interaction of gold with cerium oxide supports: $CeO_2(111)$ thin films vs CeO_x nanoparticles. *J. Phys. Chem. C*, **113**, 6042–6049, ISSN 1932-7447.

[125] Lykhach, Y., Staudt, T., Lorenz, M. P. A., Streber, R., Bayer, A., Steinrück, H.-P., and Libuda, J. (2010) Microscopic insights into methane activation and related processes on Pt/ceria model catalysts. *Chem. Phys. Chem.*, **11**, 1496–1504, ISSN 1439-7641.

[126] Rodríguez, J. A., Ma, S., Liu, P., Hrbek, J., Evans, J., and Pérez, M. (2007) Activity of CeO_x and TiO_x nanoparticles grown on Au(111) in the water-gas shift reaction. *Science*, **318**, 1757–1760, ISSN 0036-8075.

[127] Rodríguez, J. A., et al. (2009) Water-gas shift reaction on a highly active inverse CeO_x/Cu(111) catalyst: Unique role of ceria nanoparticles. *Angew. Chem. Int. Ed.*, **48**, 8047–8050, ISSN 1521-3773.

[128] Eck, S., Castellarin-Cudia, C., Surnev, S., Prince, K. C., Ramsey, M. G., and Netzer, F. P. (2003) Adsorption and reaction of CO on a ceria-Rh(111) "inverse model catalyst" surface. *Surf. Sci.*, **536**, 166–176, ISSN 0039-6028.

[129] Wrobel, R., Suchorski, Y., Becker, S., and Weiss, H. (2008) Cerium oxide layers on the Cu(111) surface: Substrate-mediated redox properties. *Surf. Sci.*, **602**, 436–442, ISSN 0039-6028.

[130] Yang, F., Graciani, J., Evans, J., Liu, P., Hrbek, J., Sanz, F. J., and Rodríguez, J. A. (2011) CO oxidation on inverse CeO_x/Cu(111) catalysts: High catalytic activity and ceria-promoted dissociation of O_2. *J. Am. Chem. Soc*, **133**, 3444–3451, ISSN 0002-7863.

[131] Hornés, A., et al. (2010) Inverse CeO_2/CuO catalyst as an alternative to classical direct configurations for preferential oxidation of CO in hydrogen-rich stream. *J. Am. Chem. Soc.*, **132**, 34–35, ISSN 0002-7863.

[132] Castellarin-Cudia, C., Surnev, S., Schneider, G., Podlucky, R., Ramsey, M. G., and Netzer, F. P. (2004) Strain-induced formation of arrays of catalytically active sites at the metal-oxide interface. *Surf. Sci.*, **554**, L120–L126, ISSN 0039-6028.

[133] Eck, S., Castellarin-Cudia, C., Surnev, S., Ramsey, M. G., and Netzer, F. P. (2002) Growth and thermal properties of ultrathin cerium oxide layers on Rh(111). *Surf. Sci.*, **520**, 173–185, ISSN 0039-6028.

[134] Grinter, D. C., Ithnin, R., Pang, C. L., and Thornton, G. (2010) Defect structure of ultrathin ceria films on Pt(111): Atomic views from scanning tunnelling microscopy. *J. Phys. Chem. C*, **114**, 17036–17041, ISSN 1932-7447.

[135] Galloway, H. C., Sautet, P., and Salmeron, H. (1996) Structure and contrast in scanning tunneling microscopy of oxides: FeO monolayer on Pt(111). *Phys. Rev. B*, **54**, R11145–R11148, ISSN 1098-0121.

[136] Mašek, K., Beran, J., and Matolíin, V. (2012) RHEED study of the growth of cerium oxide on Cu(111). *App. Surf. Sci.*, **259**, 34–34, ISSN 0169-4332.

[137] Sedona, F., Agnoli, S., and Granozzi, G. (2006) Ultrathin Wagon-wheel-like TiO_x phases on Pt(111): A combined low-energy electron diffraction and scanning tunneling microscopy investigation. *J. Phys. Chem. B*, **110**, 15359–15367, ISSN 1520-6106.

[138] Torbrügge, S., Reichling, M., Ishiyama, A., Morita, S., and Custance, O. (2007) Evidence of subsurface oxygen vacancy ordering on reduced CeO_2(111). *Phys. Rev. Lett.*, **99**, 056101, ISSN 0031-9007.

[139] Stetsovych, O., Dvořák, F., Szabová, L., Fabris, S., Mysliveček, J., and Matolín, V. (2012) Nanometer-range strain distribution in layered incommensurate systems. *Phys. Rev. Lett.*, **109**, 266102, ISSN 0031-9007.

[140] Hattab, H., et al. (2012) Interplay of wrinkles, strain, and lattice parameter in graphene on iridium. *Nano Lett.*, **12**, 678–682, ISSN 1530-6984.

[141] Kumar, S. and Schelling, P. K. (2006) Density functional theory study of water adsorption at reduced and stoichiometric ceria (111) surfaces. *J. Chem. Phys.*, **125**, 204704, ISSN 0021-9606.

[142] Azimi, G., Dhiman, R., Kwon, H.-M., Paxson, A. T., and Varanasi, K. K. (2013) Hydrophobicity of rare-earth oxide ceramics. *Nature Materials*, **12**, 315–320, ISSN 1476-1122.

[143] Henderson, M. A., Perkins, C. L., Engelhard, M. H., Thevuthasan, S., and Peden, C. H. F. (2003) Redox properties of water on the oxidized and reduced surfaces of CeO_2(111). *Surf. Sci.*, **526**, 1–18, ISSN 0039-6028.

[144] Matolín, V., et al. (2012) Water interaction with CeO_2(111)/Cu(111) model catalyst surface. *Catal. Today*, **181**, 124–132, ISSN 0920-5861.

[145] Chen, B., Ma, Y., Ding, L., Xu, L., Wu, Z., Yuan, Q., and Huang, W. (2013) Reactivity of hydroxyls and water on a CeO_2(111) thin film surface: The role of oxygen vacancy. *J. Phys. Chem. C*, **117**, 5800–5810, ISSN 1932-7447.

[146] Mullins, D. R., Albrecht, P. M., Chen, T.-L., Calaza, F. C., Biegalski, M. D., Christen, H. M., and Overbury, S. H. (2012) Water dissociation on CeO_2(100) and CeO_2(111) thin films. *J. Phys. Chem. C*, **116**, 19419–19428, ISSN 1932-7447.

[147] Gritschneder, S., Iwasawa, Y., and Reichling, M. (2007) Strong adhesion of water to CeO_2(111). *Nanotechnol.*, **18**, 044025, ISSN 0957-4484.

[148] Gritschneder, S. and Reichling, M. (2007) Structural elements of CeO_2(111) surfaces. *Nanotechnol.*, **18**, 044024, ISSN 0957-4484.

[149] Torbrügge, S., Custance, O., Morita, S., and Reichling, M. (2012) Manipulation of individual water molecules on CeO_2(111). *J. Phys.: Condens. Matter*, **24**, 084010, ISSN 0953-8984, doi: 10.1088/0953-8984/24/8/084010.

[150] Chen, H.-T., Choi, Y. M., Liu, M., and Lin, M. C. (2007) A theoretical study of surface reduction mechanisms of CeO_2(111) and (110) by H_2. *Chem. Phys. Chem.*, **8**, 849–855, ISSN 1439-7641.

[151] Fronzi, M., Piccinin, S., Delley, B., Traversa, E., and Stampfl, C. (2009) Water adsorption on the stoichiometric and reduced CeO_2(111) surface: A first-principles investigation. *Phys. Chem. Chem. Phys.*, **11**, 9188–9199, ISSN 1463-9076.

[152] Watkins, M. B., Foster, A. S., and Shluger, A. L. (2007) Hydrogen cycle on CeO_2 (111) surfaces: Density functional theory calculations. *J. Phys. Chem. C*, **111**, 15337–15341, ISSN 1932-7447.

[153] Yang, Z., Wang, Q., Wei, S., Ma, D., and Sun, Q. (2010) The effect of environment on the reaction of water on the ceria(111) surface: A DFT+U study. *J. Phys. Chem. C*, **114**, 14891–14899, ISSN 1932-7447.

[154] Watkins, M., Trevethan, T., Shluger, A. L., and Kantorovich, L. N. (2007) A comparison of dynamic atomic force microscope set-ups for performing atomic scale manipulation experiments. *Nanotechnol.*, **18**, 345503, ISSN 0957-4484.

[155] Molinari, M., Parker, S. C., Sayle, D. C., and Islam, M. S. (2012) Water adsorption and its effect on the stability of low index stoichiometric and reduced surfaces of ceria. *J. Phys. Chem. C*, **116**, 7073–7082, ISSN 1932-7447.

[156] Marrocchelli, D. and Yildiz, B. (2012) First-principles assessment of H_2S and H_2O reaction mechanisms and the subsequent hydrogen absorption on the CeO_2(111) surface. *J. Phys. Chem. C*, **116**, 2411–2424, ISSN 1932-7447.

[157] Prin, M., Pijolat, M., M., S., and Touret, O. (1991) Characterization of a cerium dioxide powder from its equilibrium with water vapour. *Thermochim. Acta*, **186**, 273–283, ISSN 0040-6031.